Failure of the Human Proximal Femur: Material and Structural Perspectives

by

Catherine Mary Ford

E S.E., Bioengineering
University of Pennsylvania
1990

M.S., Mechanical Engineering
Massachusetts Institute of Technology
1992

Submitted to the Harvard University - Massachusetts Institute of Technology
Division of Health Sciences and Technology
in Partial Fulfillment of the Requirements for the Degree of

Doctor of Philosophy

in Medical Engineering

at the

Massachusetts Institute of Technology

September, 1996

© 1996 Massachusetts Institute of Technology
All rights reserved

Author _____
Harvard-MIT Division of Health Sciences and Technology

Certified by _____
Wilson C. Hayes, Ph.D.
Maurice E. Muller Professor of Biomechanics, Harvard Medical School
Thesis Supervisor

Certified by _____
Lorna J. Gibson, Ph.D.
Prof. of Civil and Environmental Engineering and Mechanical Engineering, MIT
Thesis Supervisor

Accepted by _____
Martha Gray, Ph.D.
Director, Harvard-MIT Division of Health Sciences and Technology

MASSACHUSETTS INSTITUTE
OF TECHNOLOGY

ARCHIVES

AUG 19 1996

LIBRARIES

Failure of the Human Proximal Femur: Material and Structural Perspectives

by

Catherine Mary Ford

Submitted to the Harvard University - Massachusetts Institute of Technology
Division of Health Sciences and Technology
in Partial Fulfillment of the Requirements for the Degree of
Doctor of Philosophy in Medical Engineering

Abstract

An exponential increase in hip fracture risk is an apparently immutable consequence of aging in our society. Approximately 1.66 million hip fractures occurred worldwide in 1990, and this number is expected to increase markedly as the elderly population grows. From an engineering viewpoint, a hip fracture is a structural failure of the proximal femur resulting when loads applied to the bone exceed its structural capacity. The objective of this thesis was to improve current understanding of hip fracture etiology by investigating factors contributing to the structural capacity of the femur. This goal was accomplished using two research strategies: material level studies examining multiaxial failure properties of trabecular bone, and finite element studies at the whole bone level aimed at elucidating the relative contributions of age-related bone loss and fall mechanics to hip fracture risk. Using an analytical approach applicable to cellular materials, failure surfaces for general, three-dimensional states of stress were derived for trabecular bone of any density and degree of transverse isotropy. Comparison with surfaces derived experimentally demonstrated that the microstructural failure mechanisms used in the model do contribute to multiaxial failure behavior at the continuum level. For studies at the structural level, an anatomically accurate finite element model of the proximal femur was generated using geometric and densitometric information from Quantitative Computed Tomography (QCT). The structural capacity of the femur was predicted under load vectors representing *in vivo* falls impacting on the hip, revealing that variations in impact direction can dramatically influence load-bearing capacity. Using a novel algorithm allowing direct comparison of QCT data from femurs with different geometry, three-dimensional patterns of bone loss associated with osteopenia and osteoporosis were determined. The structural consequences of bone loss were assessed by applying these highly non-uniform density reductions to the finite element model. The results suggest that clinically "uniform" bone loss (i.e. that which appears uniform based on two-dimensional clinical bone density exams) causes progressively larger percent reductions in structural capacity, and that inter-region differences in the rate of bone loss can have a dramatic effect on structural capacity.

Thesis Supervisor: Wilson C. Hayes, Ph.D.
Title: Maurice E. Mueller Professor of Biomechanics

Thesis Supervisor: Lorna J. Gibson, Ph.D.
Title: Professor of Civil and Environmental Engineering and Mechanical Engineering

Acknowledgments

I am indebted to a number of individuals whose support and assistance led to the successful completion of this work. I would first like to thank my thesis supervisors, Toby Hayes and Lorna Gibson. I am grateful to Toby for the vision and leadership that led to the founding and successful growth of the Orthopedic Biomechanics Laboratory at Beth Israel Hospital. The outstanding personnel and facilities that Toby has brought together made for an exceptional graduate research experience, and I am grateful to have had the opportunity to be a part of the OBL. Toby's tireless insistence that I define relevant research questions, along with his emphasis on the oral and written communication of results, has left me well-prepared and confident for my future scientific endeavors. I also owe a debt of gratitude to Lorna Gibson, who taught me everything I know about modeling the mechanical behavior of cellular solids. I thank Lorna both for her outstanding technical mentoring and her concern for me as a person as well as a student. In addition to my thesis supervisors, I thank Tom McMahon of the Division of Applied Sciences at Harvard and Susan Greenspan of the Department of Bone and Mineral Metabolism at Beth Israel Hospital for their interest in this work, for their insights during committee meetings, and for their helpful perspectives on the written thesis.

The OBL is full of people who contributed in large and small ways to making my experience successful and enjoyable. One individual who deserves major credit for helping me through this thesis is Tony Keaveny. Although Tony was not officially listed as a thesis advisor, he served as my primary research mentor during my first one and a half years at the OBL. He supervised all of the experimental trabecular bone work, and guided me through the development of the finite element model of the proximal femur. Even after taking a faculty position at Berkeley, Tony continued to give freely of his time and energy and contributed significantly to this thesis. Extra-special thanks also go to Mary Bouxsein, who knew more about the ups and downs of this research (not to mention the ups and

downs of my life over the last four years) than anyone, because she eagerly listened to all of the traumas and triumphs as they happened. Those three-hour long runs during marathon training times were good for more than just getting in shape. This work also benefited from the technical input of many other graduate students and staff of the OBL. I thank all who assisted along the way, with everything from mechanical testing (Ed Wachtel, Aaron Hecker), CT data processing (John Hipp, Dan Michaeli), finite element modeling advice (Maria Oden, Matt Silva), specimen preparation (Tania Pinilla, Steve Bowman, Deb Cheng, Ed Wachtel), statistics (Betsy Myers), and exceptional computer support (Michael Harrington, Sarah Trilling).

My friends and family have been a constant and unwavering source of support for me throughout my stay in Boston. My life has been enriched in ways I could never have imagined, thanks to the group of musicians at the Paulist Center with whom I have had the privilege of playing every Saturday for the last six years. I thank my sister Beverly and my brother-in-law Bill for their friendship, support, and ability to understand what it can be like to negotiate the MIT maze. I also thank MJ for her friendship and for being there through it all. Lastly, I offer my warmest thanks to Mom and Dad for their unceasing love and for being my absolute biggest fans throughout my life. They instilled in me the value of education, and gave selflessly of their love, time and energy so that I could achieve my goals. I dedicate this thesis to them, and I hope that someday I can give to my own children what they have given to me.

Financial support for this work was provided by the National Science Foundation, the Harvard-MIT Division of Health Sciences and Technology, Rhone-Poulenc Rorer, the National Institutes of Health, and the American Association of University Women.

Table of Contents

1. Introduction 10

1.1 Background....10

1.2 Outline of Thesis....14

1.3 References....17

2. The Shear Failure Properties of Trabecular Bone, with Application to Multiaxial Failure 20

2.1 Introduction....20

2.2 Materials and Methods....23

2.2.1 Specimen Preparation....23

2.2.2 Design & Validation of Shear Strain Measurement System....25

2.2.3 Mechanical Testing....27

2.2.4 Data Analysis....28

2.2.5 Formulation of the Tsai-Wu Failure Criterion....29

2.3 Results....33

2.3.1 Shear Failure Properties....33

2.3.2 Application of Shear Properties to Multiaxial Failure....40

2.4 Discussion....42

2.5 References....48

3. Uniaxial Strength Asymmetry in Cellular Materials: An Analytical Model 50

3.1 Introduction....50

3.2 Analysis: Honeycombs....52

3.3 Results: Honeycomb....56

3.4 Analysis: Open-cell Foam....59

3.5 Results: Open-cell Foam....62

3.6 Discussion 62
3.7 References 68

4. Multiaxial Failure Properties of Cellular Materials: An Analytical Model 70

4.1 Introduction 70
4.2 Analysis: Honeycomb 71
4.3 Results: Honeycomb 75
4.4 Analysis: Foam 77
4.5 Results: Foam 82
4.6 Comparison of Analytical and Tsai-Wu Failure Envelopes 83
4.7 Discussion 84
4.8 References 94
Appendix: Derivation of Failure Surface for States of Stress where Principal Stresses are not Aligned with Principal Material Directions 96

5. The Effect of Impact Direction on the Structural Capacity of the Proximal Femur During Falls 101

5.1 Introduction 101
5.2 Materials and Methods 104
5.2.1 Finite Element Model 104
5.2.2 Loads and Boundary Conditions 105
5.2.3 Failure Criterion 107
5.3 Results 110
5.4 Discussion 112
5.5 References 117

6. Three-Dimensional Patterns of Bone Loss in the Proximal Femur 122

6.1 Introduction 122

6.2 Methods 125
6.2.1 Development and Validation of Relationship between BMD Level and Three-Dimensional Density Distribution 125
6.2.2 Determination of Patterns of Age-Related Bone Loss 130
6.3 Results 132
6.3.1 Relationship between DXA Measurements and Three-dimensional Density Distribution 132
6.3.2 Patterns of Age-Related Bone Loss 140
6.4 Discussion 147
6.5 References 151
7. The Structural Consequences of Age-Related Bone Loss in the Proximal Femur 155
7.1 Introduction 155
7.2 Materials and Methods 158
7.2.1 Finite Element Model 158
7.2.2 Application of Age-Related Density Changes to Finite Element Model 159
7.2.3 Parametric Studies of Age-Related Density Changes 160
7.2.3.1 Clinically Uniform Bone Loss 160
7.2.3.2 Clinically Non-Uniform Bone Loss 163
7.3 Results 165
7.4 Discussion 169
7.5 References 176

Chapter 1

Introduction

1.1 Background

Fracture of the proximal femur is an enormous public health problem. Over 280,000 hip fractures occur each year in the United States alone, with an estimated health care cost approaching $10 billion (AAOS, 1993). Approximately 1.66 million hip fractures occurred worldwide in 1990, with Europe and North America accounting for about half (Cooper *et al.*, 1992). With the exponential growth of the elderly population, experts project that the number of hip fractures will exceed 600,000 in the United States (AAOS, 1993) and 6.26 million throughout the world (Cooper *et al.*, 1992) by the middle of next century if incidence is not reduced. Over 90% of hip fractures occur in individuals over the age of 70 (Cummings *et al.*, 1985), a group that experiences significant morbidity and mortality as a result of these fractures. Those who experience a hip fracture have a 12 to 20 percent higher mortality rate than those of similar age and gender who do not experience a fracture, and approximately one third of fracture patients are dependent on other people or mechanical aids for mobility after fracture (Cummings *et al.*, 1985).

The successful design of intervention efforts to reduce hip fracture incidence depends upon a sound understanding of the factors that contribute to hip fracture risk. From an engineering viewpoint, a hip fracture is a structural failure of the proximal femur that results when the loads applied to the bone exceed the structural capacity of the bone. Using this conceptual framework, hip fracture risk is conveniently quantified by defining a factor of risk, which is simply the ratio of the load applied to the femur during a particular activity to the load required to fracture the femur during that activity (Hayes and Myers, 1995). When the load applied to the femur meets or exceeds the structural capacity of the

femur during a particular activity, fracture is predicted to occur. Clinical studies have demonstrated that both factors related to loading of the femur (e.g. fall direction and impact site) and factors related to the structural capacity of the femur (e.g. bone density) are significant and independent contributors to hip fracture risk (Hayes *et al.*, 1993; Greenspan *et al.*, 1994). Although complex interactions between factors related to loading (i.e. fall severity) and factors related to structural capacity (i.e. bone fragility) ultimately determine an individual's risk of hip fracture, examination of these factors independently is extremely valuable in elucidating the fundamental mechanisms through which each factor acts. In this thesis, I hope to improve our understanding of hip fracture etiology by examining factors that contribute to the structural capacity of the femur (the denominator of the factor of risk). This goal will be accomplished using two distinct but complementary research strategies: experimental and analytical studies at the material level examining the multiaxial failure properties of trabecular bone, and finite element studies at the whole bone level aimed at elucidating the contribution of various factors to the structural capacity of the femur.

The strength properties of trabecular bone as a material play a critical role in determining the load-bearing capacity of the femur. During loads associated with normal gait as well as falls on the hip, trabecular bone carries approximately 70% of the load at the subcapital region, 50% at the mid-neck, and 20% at the intertrochanteric region (Lotz *et al.*, 1995). As the trabecular bone of the proximal femur transmits these substantial loads, it experiences highly complex, multiaxial states of stress (Lotz *et al.*, 1991a). Despite its structural importance in the femur, knowledge of the failure properties of trabecular bone under multiaxial states of stress is limited. Trabecular bone failure properties have been measured under relatively simple multiaxial loading conditions (e.g. compressive loading with radial pressure [Borchers and Gibson, 1992] and biaxial plane stress [Stone *et al.*, 1983]). However, attempts to extrapolate these data to define the failure envelope for a general, three-dimensional state of stress have thus far been unsuccessful. Much of the difficulty in determining multiaxial failure properties arises from two sources: the technical

difficulties involved in performing accurate multiaxial experiments, and the potentially large inter-specimen variations in the density and architecture of trabecular bone. Further experimental work is needed to quantify the multiaxial failure properties of trabecular bone, and how they relate to density and architecture.

In addition to experimental work, analytical models of trabecular bone can also significantly enhance our understanding of multiaxial failure behavior. Microstructural models serve to relate deformation and failure mechanisms at the trabecular level to macroscopic material properties, and therefore provide a framework for interpreting and extending experimental results. Such microstructural models can be of particular value in understanding the effects of trabecular architecture on failure properties, since three-dimensional architecture is extremely difficult to control and measure in the experimental setting. The combination of accurate measurements of trabecular bone failure properties under relatively simple, experimentally feasible states of stress, combined with analytical models relating microstructural properties to macroscopically observed behavior, should lead to improvements in our understanding of multiaxial failure in trabecular bone, and in turn help to elucidate the role of trabecular bone in age-related hip fractures.

In addition to its dependence on trabecular bone failure properties, the structural capacity of the proximal femur also varies as a function of the applied loads. Since over 90% of hip fractures occur as a result of a fall (Hedlund and Lindgren, 1987; Cummings *et al.*, 1990), yet fewer than 5% of all falls actually result in a hip fracture (Tinetti, 1987; Nevitt *et al.*, 1989), the mechanics of falling must contribute considerably to hip fracture risk. In fact, both a fall to the side (Greenspan *et al.*, 1994) and impact near the hip (Hayes *et al.*, 1993) have been shown clinically to be significant contributors to hip fracture risk, independent of bone density measurements. However, the mechanisms responsible for the increased risk associated with particular types of falls has not been explained. Using the factor of risk described previously as a framework, it may be that particular types of falls cause increased fracture risk either because they increase the load applied to the femur (the

numerator of the factor of risk), because they decrease the structural capacity of the femur (the denominator of the factor of risk), or both. The ability of *any* structure to bear loads depends on the direction of application of those loads. In the case of the femur, it is well-established that substantially higher forces are needed to cause fracture under gait loading conditions than under a typical fall loading condition (Lotz *et al.*, 1991b; Lotz *et al.*, 1991a). It is likely that the range of fall trajectories experienced by hip fracture patients and other fallers expose the proximal femur to impact force vectors with a range of directions. However, the effect of differences in loading direction on the structural capacity of the femur has not been examined for loads associated with falling. Such knowledge would be beneficial in elucidating the independent contribution of fall mechanics to hip fracture risk, and could lead to improved clinical assessment of fracture risk by identifying impact load vectors that place the femur at highest risk for fracture.

Age-related reductions in bone density are by far the most widely cited and recognized explanation for the exponential increase in fracture risk that occurs with age. Prospective cohort studies have repeatedly demonstrated associations between densitometric indicators of osteopenia and the incidence of hip fracture (Cummings *et al.*, 1990; Cummings *et al.*, 1993; Melton *et al.*, 1993; Nevitt *et al.*, 1994; Cummings *et al.*, 1995). For example, a study of over 9000 women 65 years and older demonstrated that a decrease in femoral bone mineral density (BMD) of one standard deviation is associated with a 2.6-fold increase in the age-adjusted risk of hip fracture (Cummings *et al.*, 1993). Long-term follow-up of over 300 women has also shown that a one standard deviation in femoral BMD is equivalent, in terms of fracture risk, to a 13-year increase in age (Melton *et al.*, 1993). The findings of several case-control studies (Riggs *et al.*, 1982; Mazess *et al.*, 1988; Aloia *et al.*, 1992; Greenspan *et al.*, 1994) are consistent with these longitudinal investigations. Although the existence of a connection between age-related bone loss and increased hip fracture risk is indisputable, several questions related to the mechanisms underlying this connection remain unanswered or only partly answered. For example, what

is the relationship between a change in clinical bone density for an individual and a change in structural capacity of the femur? Does a given reduction in bone density at a relatively old age (i.e. starting at a relatively low BMD level) cause a larger or smaller change in structural capacity than the same bone density change starting at a relatively high BMD level? Are certain patterns of bone loss associated with larger reductions in structural capacity than other patterns? Are the *relative* values of BMD in different regions of the femur important to consider in the assessment of hip fracture risk? The results of several laboratory studies relating *ex vivo* structural capacity to clinical BMD measurements have helped to explore the answers to these questions. However, the considerable difficulties involved in controlling for the confounding influences of inter-bone differences in geometry and inter-region differences in BMD limit the extrapolation of *ex vivo* results to the longitudinal assessment of fracture risk in individuals. Modeling studies are needed to examine the role of bone density changes independent of these confounding factors. When combined with the results of experimental studies, the results of such modeling studies can be used to improve our ability to assess hip fracture risk in the clinical setting, and can be of use in the development of preventive strategies.

1.2 Outline of Thesis

All of the topics addressed in this thesis are related to proximal femur mechanics, either at the material or structural level. Although there are certainly connections between topics (which are addressed where appropriate), each represents a unique contribution and therefore each chapter is self-contained with its own Introduction, Methods or Analysis, Results, Discussion and References. The topics of the thesis lend themselves to division into two areas: studies of trabecular bone at the material level (Chapters 2, 3 and 4), and studies of hip fracture mechanics at the whole bone level (Chapters 5, 6 and 7). A brief summary of each chapter follows.

Chapter 2 describes the measurement of the failure properties of trabecular bone under shear loading, and the application of these measurements to the development of a multiaxial failure criterion for trabecular bone. Although shear is a critical component of the stresses experienced by trabecular bone during traumatic loading, the failure properties of trabecular bone in shear, and their dependence on apparent density and architecture, have not been accurately quantified. This chapter describes the development of a system for accurately measuring shear strains on trabecular bone during torsional loading, and its use in determining shear failure properties for a range of densities and for two different trabecular orientations. These results for shear loading are then combined with results from other uniaxial experiments and a triaxial experiment to formulate a Tsai-Wu failure criterion for trabecular bone.

In Chapters 3 and 4, microstructural models of cellular materials are developed to explain the uniaxial and multiaxial failure behavior of trabecular bone, and their dependence on density and architecture. In Chapter 3, microstructural analysis reveals that the density-dependent, compression-strong strength asymmetry that has been observed in trabecular bone (Keaveny *et al.*, 1994) can arise if two conditions are met: the cell wall material (i.e. trabecular tissue) is stronger in compression than in tension, and the cell walls (i.e. trabeculae) are loaded simultaneously by axial forces and bending moments. In Chapter 4, these mechanisms are incorporated into the derivation of failure surfaces for cellular materials under a general, three-dimensional state of stress. Comparison between the analytically-derived failure envelopes and those formulated experimentally in Chapter 2 suggests that the microstructural deformation and failure mechanisms described in the analytical models do in fact contribute to multiaxial failure behavior observed experimentally at the continuum level.

In Chapter 5, attention turns from failure of trabecular bone at the material level to failure of the proximal femur as a structure. The focus of this chapter is the effect of impact direction during a fall on the structural capacity of the proximal femur. Using geometric and

densitometric information from Quantitative Computed Tomography (QCT), a three-dimensional finite element model of the proximal femur is developed. The structural capacity of the femur is then predicted under load vectors that represent a range of possible *in vivo* fall impact directions. The results of this parametric study reveal that even seemingly subtle variations in impact direction from a fall can have a substantial influence on the femur's load-bearing capacity. In fact, the predicted differences in structural capacity resulting from differences in impact direction are of the same order as differences resulting from up to two decades of age-related bone loss.

Chapter 6 describes the use of QCT data to determine the three-dimensional patterns of bone loss that occur with age in the proximal femur, and their relationship to clinical measures of BMD from dual-energy x-ray absorptiometry (DXA). Since DXA measurements are by nature two-dimensional, they do not give complete information about the distribution of age-related bone loss in three dimensions, which is essential to determining the structural consequences of bone loss. This chapter describes the development of a geometric scaling algorithm that allows direct comparison of QCT density data from bones of different geometry. Using this algorithm and a database of QCT and DXA data from several femurs, a relationship between changes in BMD and changes in three-dimensional density distribution is derived and validated. Analysis of this relationship reveals that patterns of bone loss that appear uniform from clinical DXA measurements can in fact be non-uniform in three dimensions.

In Chapter 7, the relationship between BMD changes and three-dimensional density changes derived in Chapter 6 is used to assess the structural consequences of age-related bone loss. By mapping the three-dimensional density distributions associated with normal, osteopenic and osteoporotic BMD levels (diagnostic levels defined by an expert panel of the World Health Organization [Kanis *et al.*, 1994]), to the finite element model developed in Chapter 5, the structural consequences of clinically "uniform" bone loss are assessed. Since bone loss in individuals can occur at different rates in different regions of the femur,

the effects of clinically "non-uniform" bone loss in the femoral neck, trochanteric, and intertrochanteric regions is also assessed. The results of these parametric studies reveal that the reductions in structural capacity associated with clinically "uniform" bone loss can be nonlinear (i.e., can depend on the baseline BMD level), and that inter-region differences in bone loss can have a dramatic effect on structural capacity.

1.3 References

AAOS (1993) A Position Statement: Prevention of Hip Fractures. *American Academy of Orthopaedic Surgeons.*

Aloia J., McGowan D., Erens E., and Miele G. (1992) Hip fracture patients have generalized osteopenia with a preferential deficit in the femur. *Osteoporosis Int* **2**, 88-93.

Borchers R. E. and Gibson L. J. (1992) Multiaxial failure criteria for trabecular bone. *Trans 38th ORS* 547.

Cooper C., Campion G., and Melton L. (1992) Hip fractures in the elderly: A world-wide projection. *Osteoporosis Int* **2**, 285-289.

Cummings S., Nevitt M., Browner W., Stone K., Fox K., Ensrud K., Cauley J., Black D., and Vogt T. (1995) Risk factors for hip fracture in white women. *N Engl J Med* **332**, 767-773.

Cummings S. R., Black D. M., and Nevitt M. C. (1990) Appendicular bone density and age predict hip fracture in women. *JAMA* **263**, 665-668.

Cummings S. R., Black D. M., Nevitt M. C., Browner W., Cauley J., Ensrud K., Genant H. K., Palermo L., Scott J., and Vogt T. M. (1993) Bone density at various sites for prediction of hip fractures. *Lancet* **341**, 72-75.

Cummings S. R., Kelsey J. L., Nevitt M. C., and O'Dowd K. J. (1985) Epidemiology of osteoporosis and osteoporotic fractures. *Epidemiologic Reviews* **7**, 178-208.

Greenspan S. L., Myers E. R., Maitland L. A., Resnick N. M., and Hayes W. C. (1994) Fall severity and bone mineral density as risk factors for hip fracture in ambulatory elderly. *JAMA* **271**, 128-133.

Hayes W. and Myers E. (1995) Biomechanics of fractures. In *Osteoporosis: Etiology, Diagnosis and Management*, 93-114, Ed. Riggs B., and Melton L., Lippincott-Raven Publishers, Philadelphia.

Hayes W. C., Myers E. R., Morris J. N., Gerhart T. N., Yett H. S., and Lipsitz L. A. (1993) Impact near the hip dominates fracture risk in elderly nursing home residents who fall. *Calcified Tissue International* **52**, 192-198.

Hedlund R. and Lindgren U. (1987) Trauma type, age and gender as determinants of hip fracture. *J Orthop Res* **5**, 242-246.

Kanis J. A., Melton L. J., Christiansen C., Johnston C. C., and Khaltaev N. (1994) The diagnosis of osteoporosis. *J Bone Min Res* **9**, 1137-1141.

Keaveny T. M., Wachtel E. F., Ford C. M., and Hayes W. C. (1994) Differences between the tensile and compressive strengths of bovine tibial trabecular bone depend on modulus. *J Biomech* **27**, 1137-1146.

Lotz J. C., Cheal E. J., and Hayes W. C. (1991a) Fracture prediction for the proximal femur using finite element models: Part 1-Linear analysis. *J Biomech Eng* **113**, 353-360.

Lotz J. C., Cheal E. J., and Hayes W. C. (1991b) Fracture prediction for the proximal femur using finite element models: Part 2-Nonlinear analysis. *J Biomech Eng* **113**, 361-365.

Lotz J. C., Cheal E. J., and Hayes W. C. (1995) Stress distributions within the proximal femur during gait and falls: Implications for osteoporotic fracture. *Osteoporosis Int* **5**, 252-261.

Mazess R., Barden H., Ettinger B., and Schultz E. (1988) Bone density of the radius, spine and proximal femur in osteoporosis. *J Bone Min Res* **3**, 13-18.

Melton L., Atkinson E., O'Fallon W., Wahner H., and Riggs B. (1993) Long-term fracture prediction by bone mineral assessed at different skeletal sites. *J Bone Min Res* **8**, 1227-1233.

Nevitt M., Johnell O., Black D., Ensrud K., Genant H., and Cummings S. (1994) Bone mineral density predicts non-spine fractures in very elderly women. *Osteoporosis Int* **4**, 325-331.

Nevitt M. C., Cummings S. R., Kidd S., and Black D. (1989) Risk factors for recurrent nonsyncopal falls: A prospective study. *JAMA* **261**, 2663-2668.

Riggs B. L., Wahner H. W., Seeman E., Offord K. P., Dunn W. L., Mazess R. B., Johnson K. A., and Melton L. J. (1982) Changes in bone mineral density of the proximal femur and spine with aging. *J Clin Invest* **70**, 716-723.

Stone J. L., Beaupre G. S., and Hayes W. C. (1983) Multiaxial strength characteristics of trabecular bone. *J Biomech* **16**, 743-752.

Tinetti M. E. (1987) Factors associated with serious injury during falls among elderly persons living in the community. *J. Am Geriatr Soc* **35**, 644-648.

Chapter 2

The Shear Failure Properties of Trabecular Bone, with Application to Multiaxial Failure

2.1 Introduction

Prediction of trabecular bone failure during *in vivo* loading, which is essential for prosthesis design and fracture risk assessment, requires accurate knowledge of its shear failure properties. If the high shear stresses which exist near prostheses (Cheal *et al.*, 1992) exceed the shear strength of trabecular bone, prosthesis loosening may occur. Since falls can induce multiaxial stresses in the proximal femur (Lotz *et al.*, 1991), hip fracture risk prediction also requires knowledge of shear failure properties, which directly affect multiaxial strength (Tsai and Wu, 1971). Since trabecular bone in load-bearing skeletal regions is adapted to transmit compressive and tensile loads along its primary orientation during habitual activities, shear failure may play a large role in trabecular bone fracture during traumatic loads which are not aligned with the primary orientation.

There is mounting evidence that failure strains for tensile (Rohl *et al.*, 1991; Keaveny *et al.*, 1994c) and compressive (Hvid *et al.*, 1985; Hansson *et al.*, 1987; Mosekilde *et al.*, 1987; Hvid *et al.*, 1989; Keaveny *et al.*, 1994c) loading of trabecular bone are homogeneous (independent of apparent density and modulus) and isotropic (independent of trabecular orientation, Turner, 1989; Keaveny *et al.*, 1994b), suggesting that trabecular bone failure is fundamentally a function of the strain that the bone experiences, rather than the stress. However, previous investigations of the *shear* failure properties of trabecular bone have focused exclusively on *stresses* at failure (Halawa *et al.*, 1978; Saha and Gorman, 1981; Stone *et al.*, 1983), such that there is currently a lack of

knowledge about shear failure *strains*. In addition, there is a lack of information regarding relationships between shear failure properties (both stresses and strains) and trabecular orientation. Knowledge of these relationships would provide considerable insight into whether trabecular bone failure *in vivo* is due primarily to shear or to normal strains, both for when the bone is subjected to habitual loading or to traumatic, off-axis loading. If trabecular bone failure during off-axis loading occurs primarily in shear, this result may have substantial implications for predicting age-related fracture risk and evaluating the structural consequences of osteoporosis.

The existing knowledge related to failure of trabecular bone under multiaxial loads is even more limited than the available data for shear failure properties. The main obstacles to performing multiaxial strength experiments on trabecular bone have been its wide range in density and architecture within a specimen, as well as the considerable difficulties involved in applying and measuring controlled multiaxial loads to trabecular bone specimens. However, the recent development of new protocols for preparation and testing of trabecular bone specimens allows for greater control of trabecular architecture within a specimen, and for significant reduction of experimental artifacts in the measurement of tensile and compressive strains (Keaveny *et al.*, 1994a). In addition, this chapter describes the development of a new system for accurate measurement of shear strains during pure shear loading. These new experimental protocols can now be used to accurately perform the experiments needed to determine the multiaxial failure properties of trabecular bone.

The strength of trabecular bone under any arbitrary three-dimensional state of stress can be predicted by combining the results of several uniaxial and simple multiaxial experiments into a multiaxial failure criterion. A general multiaxial failure criterion applicable to most engineering materials is the Tsai-Wu criterion (Tsai and Wu, 1971), which requires experimental determination of up to 27 independent coefficients depending upon material anisotropy. For a transversely isotropic material (a reasonable simplification for much of the trabecular bone in the proximal femur, vertebral body, and proximal tibia),

seven coefficients are independent. To determine these coefficients, seven destructive mechanical tests are required: uniaxial tension in the longitudinal and transverse directions (2 experiments), uniaxial compression in the longitudinal and transverse directions (2 experiments), pure shear in the longitudinal and transverse directions (2 experiments), and axial compression with radial pressure (1 experiment). The first part of this chapter describes the methods and results for two of these experiments, pure shear in the longitudinal and transverse directions. The additional 5 experiments were performed by teams of collaborating investigators (Keaveny *et al.*, 1994b; Keaveny *et al.*, 1994c; Keaveny *et al.*, 1996), using identical specimen preparation methods and similar mechanical testing protocols. In the second part of this chapter, results from the pure shear experiments are combined with results from the remaining 5 experiments to formulate the Tsai-Wu failure criterion for trabecular bone.

It was hypothesized that shear failure strains (yield and ultimate) in trabecular bone are homogeneous, and that by contrast to shear failure stresses which are anisotropic, shear failure strains are isotropic. It was also hypothesized that shear is a dominant failure mode when trabecular bone is loaded obliquely relative to its primary trabecular orientation. To test these hypotheses, the specific objectives were to: 1) determine the dependence of shear failure stresses and failure strains on apparent density and shear modulus by testing cylindrical specimens of bovine tibial trabecular bone to failure in torsion; 2) compare magnitudes of shear failure stresses and strains for specimens with longitudinal versus transverse trabecular orientations; 3) use the shear data, combined with compressive, tensile and triaxial data (Keaveny *et al.*, 1994c; Keaveny *et al.*, 1996), to formulate the Tsai-Wu criterion for trabecular bone, and 4) and use the Tsai-Wu criterion to investigate the dominant failure modes when compressive loads are applied obliquely relative to the primary trabecular orientation.

2.2 Materials and Methods

2.2.1 Specimen Preparation

Thirty-nine tibiae from 1-2 year old cows were obtained from a slaughterhouse (Bertolino Beef Company, Boston, MA). Reduced-section cylindrical specimens, used to bias failure toward a region of uniform surface stress, were prepared according to published protocols (Keaveny *et al.*, 1994a). Briefly, sagittal and coronal plane sections of bovine proximal tibiae were radiographed to identify regions of longitudinally and transversely oriented trabecular bone (Fig. 1). Parallelepipeds were cut from well-oriented regions, and 40 mm long, 8.3 mm diameter cylinders were obtained using a diamond-tipped coring tool (#102095, Starlite, Rosemont, PA) at 360 RPM. The specimen ends were cleaned, dried, and press-fit with cyanoacrylate (Prism 401, Loctite, Newington, CT) into aligned brass end-caps. After freezing for three hours at -70° C, the central 18 mm section was turned down at 315 RPM to a diameter of six mm. Microscopic analysis has demonstrated that no obvious damage occurs to surface trabeculae during this machining process (Keaveny *et al.*, 1994a). All but the embedded ends of the specimens were kept wet during preparation and testing. Twenty-eight longitudinal and 26 transverse specimens were produced in this manner. Of the 39 tibiae used, 17 of the bones yielded only longitudinal specimens, 20 of the bones yielded only transverse specimens, and 2 bones yielded both longitudinal and transverse specimens. Due to the arrangement of trabecular bone within the bovine proximal tibia, longitudinal specimens tended to come from the anterior and posterior aspects, and transverse specimens generally came from closer to the central aspect. Despite the potential bias introduced by this slight difference in harvest locations, serial sectioning of a random subset of specimens revealed that trabecular architectures within the two groups were similar, and each were approximately transversely isotropic (Fig. 1).

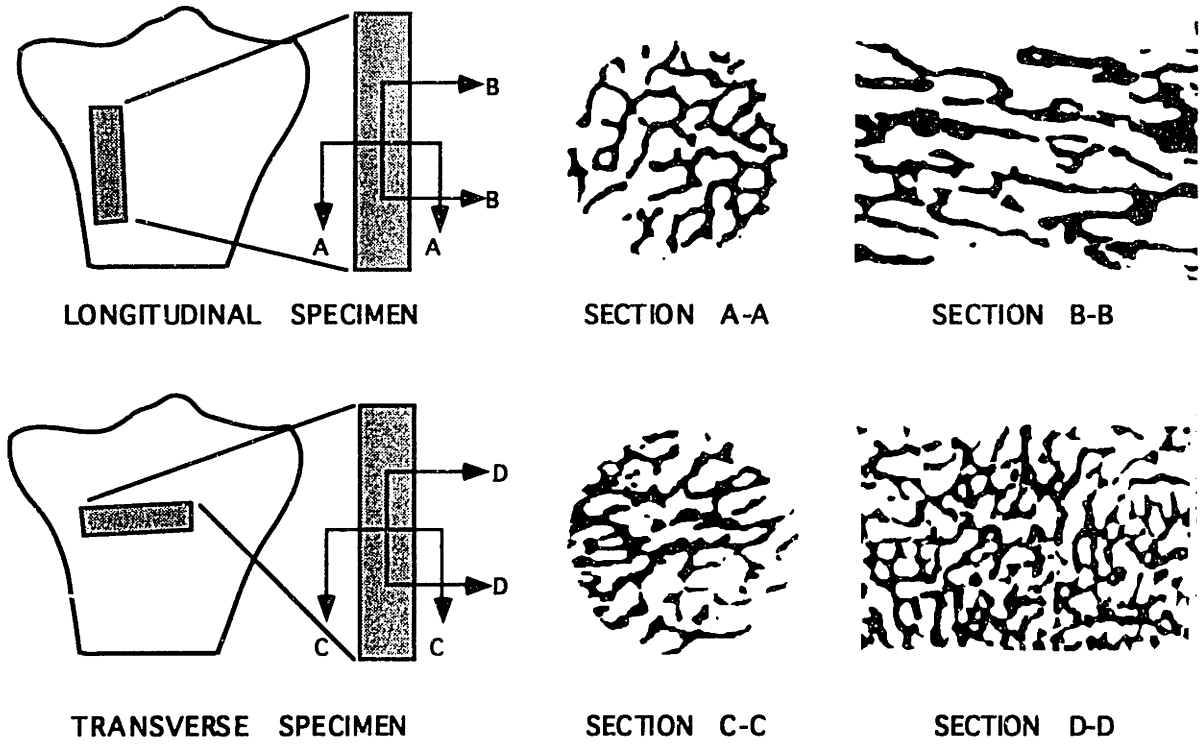

Figure 1: Sections of typical trabecular bone specimens (bone is black) from longitudinal (top) and transverse (bottom) groups. Longitudinal specimens, where the primary trabecular orientation was parallel to the long axis of the specimen (Section B-B), were typically harvested from the anterior and posterior aspects of the tibia and the long axis of the specimen was approximately aligned with the long axis of the tibia. Transverse specimens, where the primary trabecular orientation was perpendicular to the long axis of the specimen (Section D-D), were typically harvested from the central aspect of the tibia, with the long axis of the specimen perpendicular to the long axis of the tibia. The similarity in architecture between Sections A-A and D-D, which appear isotropic, combined with the similarity between Sections B-B and C-C, which appear aligned, demonstrates that the architecture of the bone in both groups was approximately transversely isotropic.

2.2.2 Design & Validation of Shear Strain Measurement System

To measure shear strain on the reduced section of each specimen, a rotational displacement transducer system was designed (Fig. 2). This system included two 1 mm thick, 13 mm diameter split polyethylene rings, attached 6 mm apart to the specimen gage length using orthodontic elastic bands. A 0.3 mm thick aluminum tab perpendicular to each ring was used to couple the rotation at the specimen surface to the deflection of a linear variable differential transformer (LVDT, model LBB-375-TA-100, Lucas Schaevitz, Pennsauken, NJ). Engineering shear strain on the gage length surface γ was calculated based on the deflections of the LVDT's δ_1 and δ_2, the axial distance between the two rings L, the distances between the specimen surface and the point of contact of each LVDT with its aluminum tab t_1, t_2, and the radius of the specimen r using the following equation:

$$\gamma = \left[\arctan\left(\frac{\delta_1}{r+t_1}\right) - \arctan\left(\frac{\delta_2}{r+t_2}\right) \right] \frac{r}{L} \qquad (1)$$

Validation was accomplished by comparing elastic strains measured with this system to those measured using a rosette strain gage glued to a 6 mm diameter reduced-section aluminum specimen. Ten non-destructive torsional tests were performed with repositioning of the rotational transducer system between each test. The mean (± S.D.) percent difference between the strain gage measurement of strain and the rotational transducer system measurement for the 10 tests (1.7% ± 1.0%, range -3.4% - 2.0%) was not statistically different from zero ($p = 0.24$), confirming the system's accuracy with respect to the strain gage. The coefficient of variation of the rotational transducer system measurement on the aluminum specimen was 1.9%, demonstrating its repeatability. The shear modulus of one randomly-chosen bovine tibial trabecular bone specimen was also

measured six times with repositioning of the transducer system each time, yielding a coefficient of variation on trabecular bone of 4.5%. Based on these data, the system was considered to be accurate and precise for bovine trabecular bone.

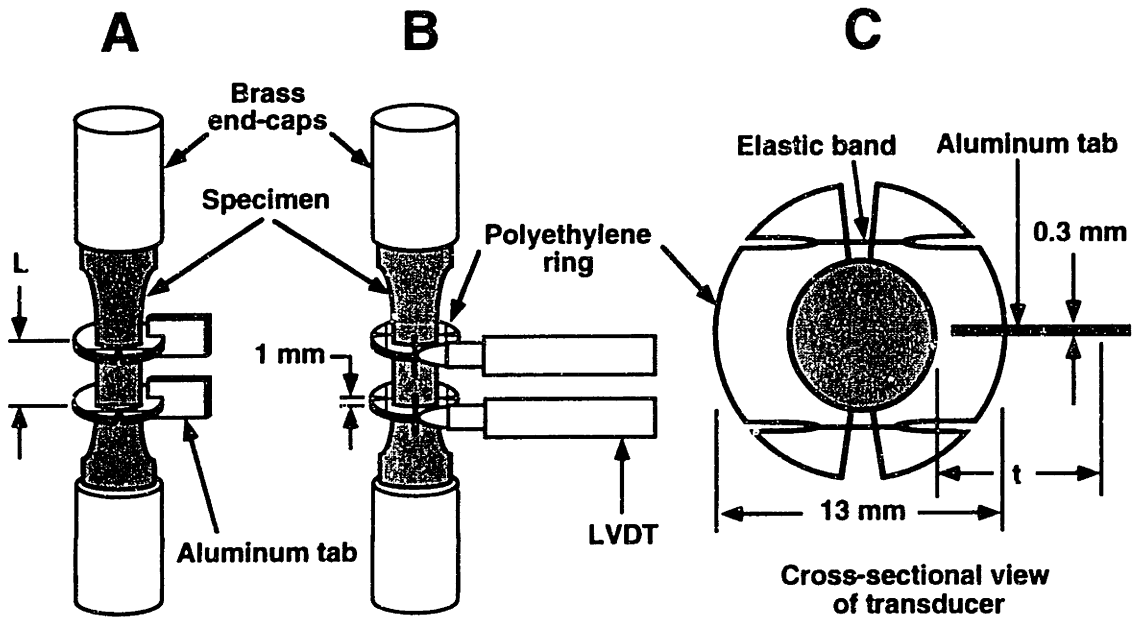

Figure 2: Schematic of rotational transducer system used to measure shear strain on specimen surface (not to scale). Each 40 mm long, 8.3 mm diameter trabecular bone core was glued into brass endcaps approximately 25 mm apart, and the central 18 mm length was turned down to a diameter of 6 mm. Two 1 mm-thick, split polyethylene rings were mounted to the gage length of each specimen (L ≈ 6 mm nominally) using orthodontic elastic bands. A 0.3 mm thick aluminum tab perpendicular to each ring was used to couple the angular displacement of the specimen surface to the deflection of a linearly variable differential transformer (LVDT), positioned perpendicularly at a distance t = 8 mm from the edge of the specimen. (A) View of rotational transducer system showing setup without LVDT's. (B) Perpendicular view, showing LVDT placement. (C) Top view detail of split polyethylene ring, showing attachment to specimen via orthodontic elastic bands.

2.2.3 Mechanical Testing

Young's modulus was measured non-destructively in compression using a uniaxial servo-hydraulic load frame (Model 1331, Instron Corp., Canton, MA). Specimen diameter was measured six times with a digital caliper. Specimens were instrumented with a 5 mm gage length, 16 gram extensometer (Model 632-29C-30, MTS, Minneapolis, MN) and loaded from 0% to 0.4% and back to 0% strain four times with the extensometer repositioned 90° circumferentially each time. Young's modulus was defined as the mean of the slopes of the resulting stress-strain curves between 0.1% and 0.4% strain (Keaveny *et al.*, 1994c).

After overnight storage at 2° C, specimens were tested to failure in torsion at room temperature using a biaxial servo-hydraulic load frame (Series 3300, Interlaken Corp., Minneapolis, MN). The rotational transducer system was mounted onto each specimen, and the axial distance between the two rings was determined using the mean of six measurements with a digital caliper. The end-caps were then gripped in the test frame with zero axial load and torque. Angular displacement was applied at a rate of 2°/sec (rate of approximately 0.6% strain/sec, similar to the rate of 0.5% strain/sec used in previous experiments [Keaveny *et al.*, 1994c]) up to an angular displacement of at least 30° to ensure reaching the ultimate torque. Torque was measured using a multicomponent force transducer (Model MC3A-6-500, Advanced Mechanical Technology, Inc., Newton, MA).

After mechanical testing, a low speed diamond saw (Labcut 1010, Extec, Enfield, CT) was used to section out a cylinder (approximately 5 mm in length) from one or both sides of the fracture site, depending on the amount of intact bone remaining in the gage length. The height and diameter of each cylinder were measured six times using a digital caliper. Marrow was removed from the cylinders using at least five 10-minute cycles in an ultrasonic cleaner with a 1:3 bleach:water solution, with a water jet rinse after each cycle.

The cylinders were centrifuged for 15 minutes at 1000 RPM and weighed to calculate wet apparent density.

2.2.4 Data Analysis

Shear stress τ was determined from the torque versus angle of twist curve using the following equation (Nadai, 1950):

$$\tau = \frac{1}{2\pi r^3}\left[\theta \frac{dT}{d\theta} + 3T\right] \quad (2)$$

where T is the measured torque, r is the radius of the specimen, and θ is the angle of twist per unit length. The term dT/dq was determined by fitting a fifth-degree polynomial to the torque versus angle of twist curve. Although the derivation of equation (2) assumes material isotropy, the errors associated with use of this equation should be minimal since the specimens were approximately transversely isotropic and trabeculae were aligned either parallel or perpendicular to the axis of the specimen. Shear strain at the specimen surface was calculated using equation (1). Shear modulus was defined as the slope of the stress-strain curve between 0.1% and 0.4% strain (Keaveny *et al.*, 1994c). The elastic range was the strain at which a line drawn from the origin with a slope equal to 95% of the shear modulus intersected the stress-strain curve. The yield stress and yield strain of each specimen were defined by the intersection of the stress-strain curve with a line parallel to the line defining shear modulus, but offset by 0.2% strain. The ultimate stress was the maximum stress; the ultimate strain was the lowest strain corresponding to the ultimate stress.

Six specimens were lost during testing, leaving 48 specimens (from 36 different tibiae; n = 25 longitudinal; n = 23 transverse) for statistical analysis. Reasons for lost

specimens were: 1) insufficient gage length for proper rotational transducer placement (2 transverse); 2) specimen mishandling (2 longitudinal, 1 transverse); and 3) operator error (1 longitudinal). Although four longitudinal and nine transverse specimens fractured outside the gage length, the stress-strain curves for these specimens indicated that the fractures occurred after the ultimate stress had been reached within the gage length. Thus, valid yield and ultimate data were obtained for all 48 specimens.

An unpaired Student's *t*-test indicated that the mean apparent density in the transverse group (0.59 ± 0.11 g/cm^3) was 18% higher ($p = 0.008$) than in the longitudinal group (0.50 ± 0.11 g/cm^3). Thus, comparisons between failure stresses were based on mean values adjusted for apparent density, using analyses of covariance with apparent density as covariate (RS1 version 4.3, BBN Software, Cambridge, MA). Unpaired *t*-tests were used to detect any dependence of failure strains on the trabecular orientation, since these properties did not depend on apparent density (see below). Linear regression analysis was used to determine relationships between shear failure properties, shear modulus and apparent density.

2.2.5 Formulation of the Tsai-Wu Failure Criterion

The Tsai-Wu failure criterion is a mathematical formulation that describes an ellipsoidal failure surface in six-dimensional stress space. The criterion can be expressed using indicial notation as

$$F_i\sigma_i + F_{ij}\sigma_i\sigma_j = 1 \qquad i,j = 1-6 \tag{3}$$

where σ_i are the stress components and F_i and F_{ij} are the experimentally derived Tsai-Wu coefficients. For a coordinate system where directions 1, 2 and 3 correspond to directions X, Y and Z, the σ_i indices i = 1-3 correspond to the normal stresses σ_{xx}, σ_{yy},

and σ_{zz}; the indices i = 4-6 correspond to the shear stresses τ_{xy}, τ_{yz}, and τ_{xz}. For a transversely isotropic material with isotropy in the 2-3 (or transverse) plane, the indices 2 and 3 of Equation 3 are interchangeable, as are the indices 4 and 6. In this case, the criterion (Eqn. 3) reduces to

$$F_1\sigma_1 + 2F_2\sigma_2 + F_{11}\sigma_1^2 + 4F_{12}\sigma_1\sigma_2 + 2\left(F_{22} + F_{23}\right)\sigma_2^2 \qquad (4)$$
$$+2\left(F_{22} - F_{23}\right)\sigma_4^2 + 2F_{55}\sigma_5^2 = 1$$

Six of the independent coefficients can be found from uniaxial tests (tension, compression and shear performed on longitudinally and transversely oriented specimens); they are expressed in terms of the uniaxial strengths as follows (Tsai and Wu, 1971)

$$F_1 = \frac{1}{\sigma_1^t} - \frac{1}{\sigma_1^c} \qquad F_2 = \frac{1}{\sigma_2^t} - \frac{1}{\sigma_2^c} \qquad F_3 = F_2$$
$$F_4 = F_5 = F_6 = 0$$
$$F_{11} = \frac{1}{\sigma_1^t\sigma_1^c} \qquad F_{22} = \frac{1}{\sigma_2^t\sigma_2^c} \qquad F_{33} = F_{22} \qquad (5)$$
$$F_{44} = \frac{1}{\sigma_4^2} \qquad F_{55} = \frac{1}{\sigma_5^2} \qquad F_{66} = F_{44}$$

where the superscripts t and c refer to tensile and compressive strengths, respectively. The coefficient F_{12} can be determined from a triaxial test that combines axial loading in the longitudinal (1) direction with radial pressure in the transverse (2 and 3) directions. For this loading condition, the Tsai-Wu criterion reduces to

$$F_1\sigma_1 + 2F_2p + F_{11}\sigma_1^2 + 4F_{12}\sigma_1p + 2\left(F_{22} + F_{23}\right)p^2 = 1 \qquad (6)$$

where p is the applied radial pressure. The coefficient F_{23} is not independent; Cowin (1986) derived the following equation for F_{23} based on symmetries in the microstructure of a transversely isotropic material:

$$F_{23} = F_{22} - 0.5F_{55} \tag{7}$$

Equation 6 can be rearranged to express F_{12} as a function of the known coefficients (F_1, F_2, F_{11}, F_{22}, and F_{23}), and the radial pressure p and axial stress σ_1 at failure in the triaxial test, giving

$$F_{12} = \frac{1}{4\sigma_1 p}\left(1 - F_1\sigma_1 - 2F_2 p - F_{11}\sigma_1^2 - 2\left(F_{22} + F_{23}\right)p^2\right). \tag{8}$$

Each of the coefficients F_{ij} was expressed as a function of density, using power law relationships between strength values and apparent density from the seven experiments. The equations for calculating the coefficients F_1 and F_{11} were determined by Keaveny *et al.* (1994c), who measured the tensile and compressive strengths of longitudinally oriented specimens. Equations for the coefficients F_2 and F_{22} were derived from similar experiments (Keaveny *et al.*, 1994b, unpublished data) on transversely oriented specimens. The equations for calculating the coefficients F_{44} and F_{55} were derived directly from the shear stress results described later in this chapter. Finally, the equation governing the coefficient F_{12} was derived by Keaveny *et al.* based on the results of triaxial tests on longitudinal specimens of trabecular bone (Keaveny *et al.*, 1996). Using these coefficient values, the Tsai-Wu failure envelope was calculated at three levels of apparent density (0.30, 0.45, and 0.60 g cm^{-3}), for two states of stress: biaxial stress with $\sigma_3 = 0$, and triaxial stress with $\sigma_2 = \sigma_3$.

To gain insight into the importance of shear properties in multiaxial failure behavior, yield stresses were predicted for off-axis compressive loads acting from 0° to 90° relative to the primary orientation (equivalent to biaxial stress in the 1-2 plane) using both the maximum stress (Jones, 1975) and the newly developed Tsai-Wu failure criterion. The maximum stress criterion was used in addition to the Tsai-Wu criterion because it does not allow for interactions between different failure modes, and therefore it provides insight into the dominant mode of failure for a given loading condition. Under the maximum stress criterion, yielding was predicted when either: 1) the normal stress in the longitudinal direction exceeded the longitudinal yield stress, 2) the normal stress in the transverse direction exceeded the transverse yield stress, or 3) the shear stress in the 1-2 direction exceeded the transverse shear yield stress. Therefore, the predicted yield stress was the minimum of:

$$\sigma_y = \frac{\sigma_1^c}{\cos^2\theta}$$

$$\sigma_y = -\frac{\sigma_2^c}{\sin^2\theta} \qquad (9)$$

$$\sigma_y = \frac{\sigma_4}{\sin\theta\cos\theta}$$

where σ_y is the off-axis compressive yield stress, θ is the angle between the applied stress and the primary trabecular orientation, σ_1^c is the longitudinal compressive yield stress, σ_2^c is the transverse compressive yield stress, and σ_4 is the transverse shear yield stress determined in this experiment. All yield stress values were calculated from the same density-strength relationships used to formulate the Tsai-Wu constants, evaluated at an overall mean apparent density of 0.62 g cm^{-3}. To allow for interactions between failure modes and therefore provide a more realistic prediction of off-axis behavior, off-axis yield

stresses were also predicted using the more complex Tsai-Wu criterion. For a transversely isotropic material under an off-axis compressive load, the Tsai-Wu failure criterion was reduced to:

$$F_1\sigma_y\cos^2\theta + F_2\sigma_y\sin^2\theta + F_{11}\sigma_y^2\cos^4\theta + F_{22}\sigma_y^2\sin^4\theta + F_{44}\sigma_y^2\sin^2\theta\cos^2\theta + 2F_{12}\sigma_y^2\sin^2\theta\cos^2\theta = 1 \quad (10)$$

where the F_i and F_{ij} terms are defined in Equations 5. To investigate the relative contribution of shear to the biaxial failure properties, off-axis yield stress σ_y were predicted using a value of F_{44} calculated based on the measured transverse shear yield stress values, and also using values of F_{44} calculated assuming that shear yield stress values were 30% higher and 30% lower than measured values, while keeping all other properties constant. All off-axis yield stress predictions were made for an overall mean apparent density of 0.62 g cm^{-3}.

2.3 Results

2.3.1 Shear Failure Properties

All stress-strain curves were linear initially, followed by a gradual yield region until the ultimate point was reached (Fig. 3). Since the theory used to calculate the stress-strain curves is not valid beyond the ultimate point, conclusions could not be drawn regarding stress-strain behavior beyond the ultimate point. However, it was noted that specimens carried one-third to two-thirds of the ultimate torque when the limit of the rotational transducer system was reached (approximately 15% strain). Since all bone throughout the cross-section has yielded when the maximum torque is reached, this behavior suggests that there is a substantial load-carrying capacity after shear failure. Fracture lines were generally

oblique (at approximately 45°) in the longitudinal group, and were either oblique or perpendicular to the specimen axis in the transverse group.

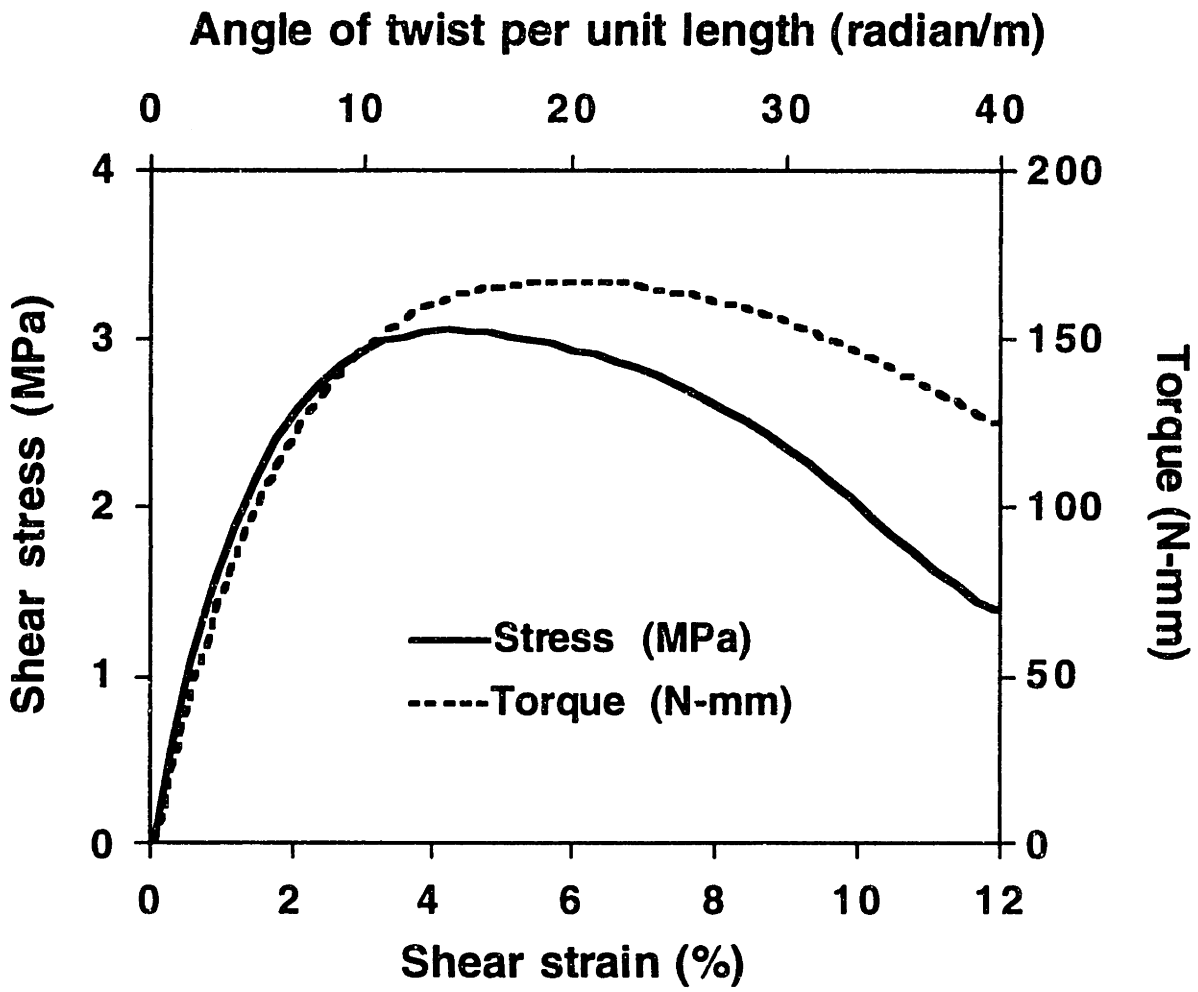

Figure 3: Typical stress-strain and torque versus angle of twist (per unit length) curves for a longitudinal specimen. All specimens exhibited linear behavior initially, and yielded between 1.05% and 1.78% strain. The equation used to calculate stress from torque is not valid beyond the ultimate point. However, specimens typically carried one-third to two-thirds of the ultimate torque when the limit of the rotational transducer system was reached (approximately 15% strain), suggesting that there is a load-carrying capacity after the ultimate stress in shear.

While shear failure stresses were heterogeneous (i.e. dependent on apparent density and shear modulus) as expected, shear failure strains were homogeneous (i.e. independent of apparent density and shear modulus). Shear yield and ultimate stresses were positively and linearly correlated with apparent density (r^2 = 0.61 - 0.80, Fig. 4, Table 1), and the slopes of the relationships were statistically similar (p = 0.20 and 0.36) for longitudinal vs. transverse trabecular orientations. By contrast to the failure stresses, shear failure strains were independent of apparent density (Fig. 5, Table 1). Similar but stronger relationships were observed for failure stresses with shear modulus as the independent variable. There were weak negative correlations (longitudinal, r^2 = 0.25, p = 0.01; transverse, r^2 = 0.20, p = 0.03) between yield strain and shear modulus and between ultimate strain and shear modulus in the longitudinal group (r^2 = 0.35, p = 0.002, Table 1).

While yield and ultimate stresses were highly anisotropic, ultimate strains were isotropic and yield strains were only slightly anisotropic (Table 2). Mean (± S.D.) values of shear yield and ultimate stress for the longitudinal orientation were 4.24 ± 1.42 MPa and 6.35 ± 2.00 MPa respectively; after adjusting for apparent density, these values were 62% and 61% higher respectively (p < 0.0001) than for the transverse orientation. The mean shear yield strain for the longitudinal orientation was 1.46 ± 0.19%, which was 10% higher (p = 0.01) than for the transverse orientation (1.33 ± 0.15%). By contrast to the yield strains, there was no difference (p = 0.24) between the mean ultimate strains for longitudinal (4.60 ± 0.77%) vs. transverse (4.24 ± 1.25%) trabecular orientations.

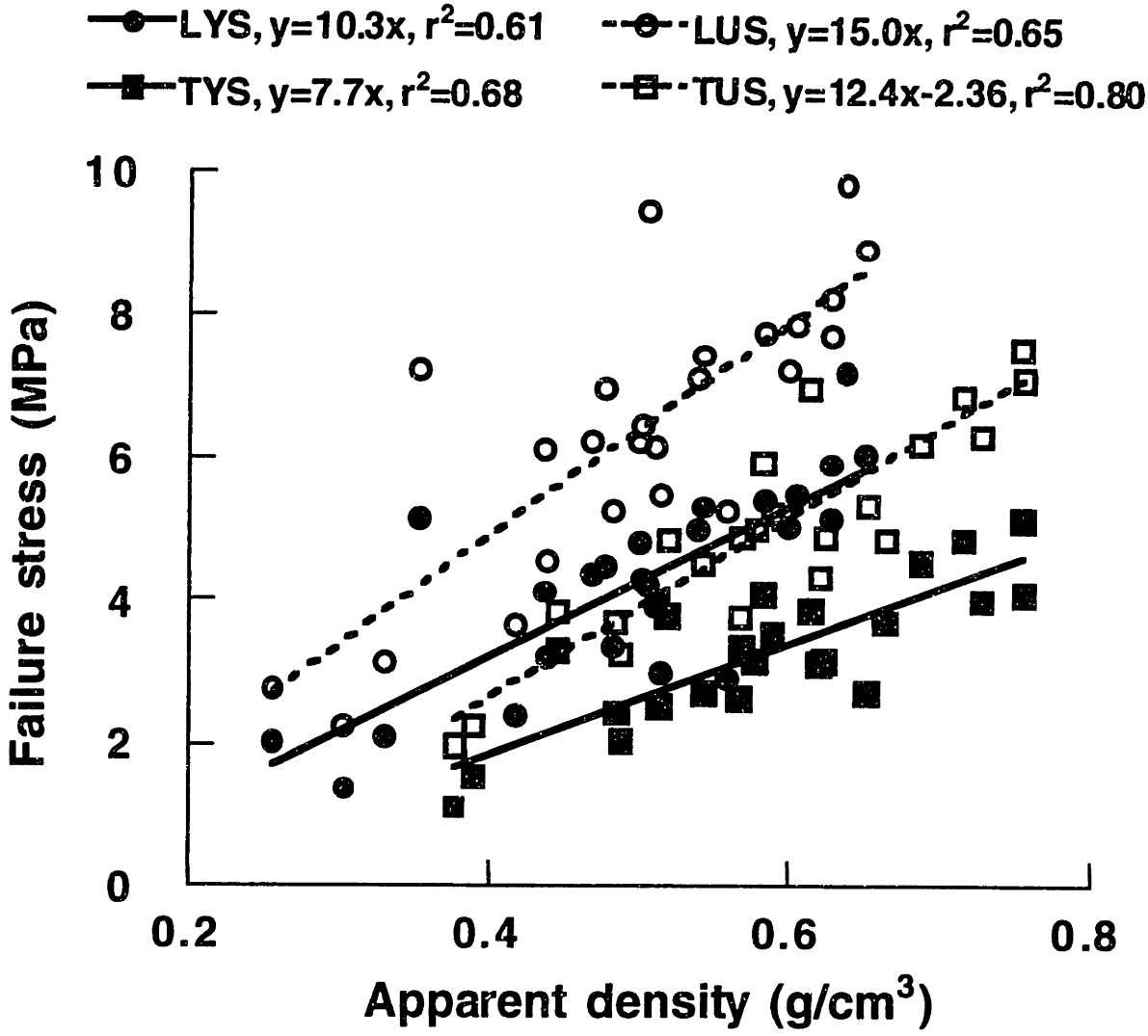

Figure 4: Plots of yield and ultimate stress against apparent density for longitudinal and transverse trabecular orientations. LYS, longitudinal yield stress; TYS, transverse yield stress; LUS, longitudinal ultimate stress; TUS, transverse ultimate stress. For both yield and ultimate stress, the slopes of the relationships were statistically similar for the two trabecular orientations, although the adjusted mean (± S.E.M.) yield and ultimate stresses for the longitudinal group (4.61 ± 0.16 MPa and 6.92 ± 0.21 MPa) were 62% and 61% higher, respectively ($p < 0.0001$, analysis of covariance with apparent density as covariate) than for the transverse group (2.85 ± 0.17 MPa and 4.30 ± 0.22 MPa).

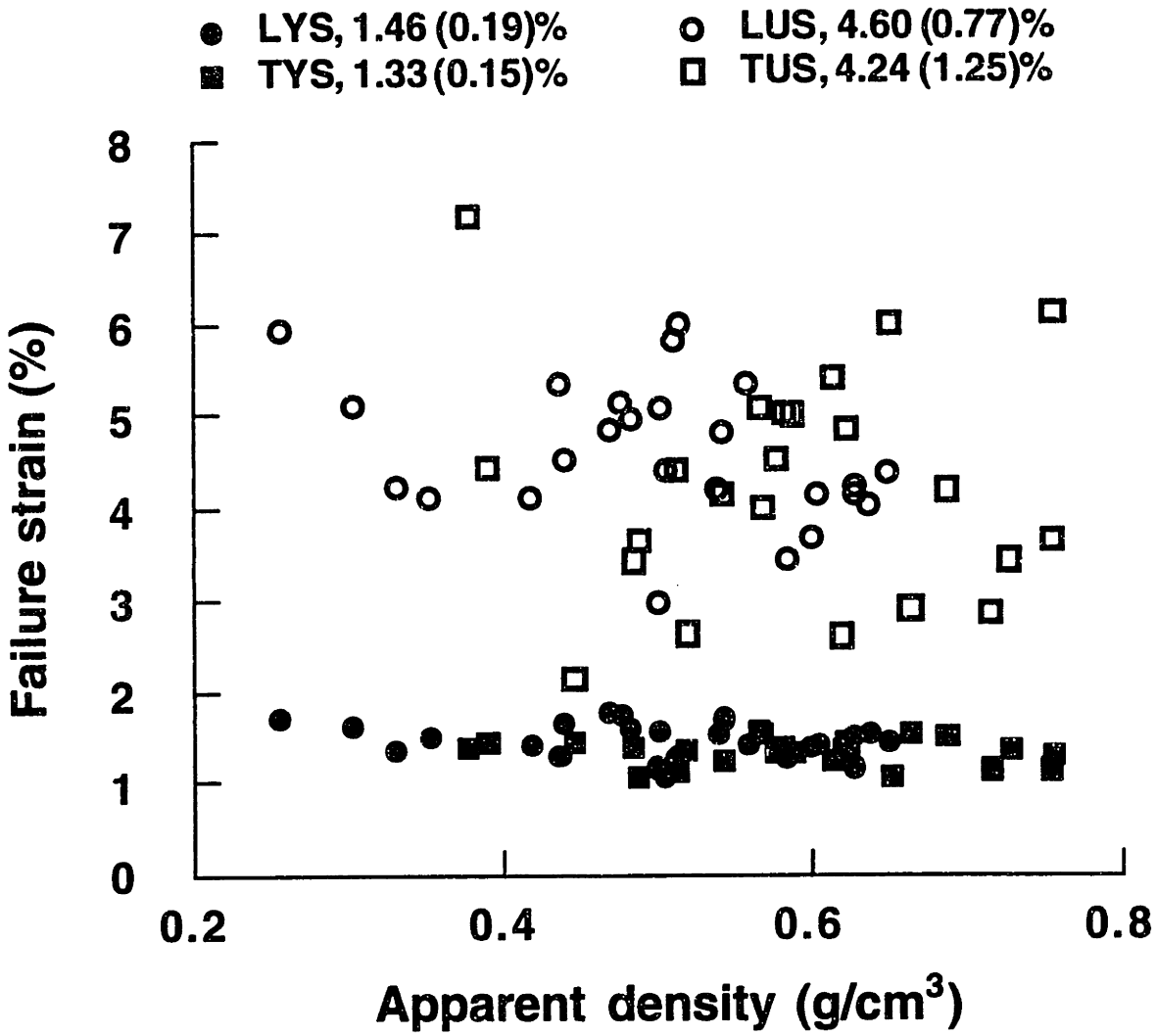

Figure 5: Plots of yield and ultimate strain against apparent density for longitudinal and transverse trabecular orientations. LYS, longitudinal yield strain; TYS, transverse yield strain; LUS, longitudinal ultimate strain; TUS, transverse ultimate strain; numbers are mean (S.D.). Yield and ultimate strains were independent of apparent density in both groups. The mean (± S.D.) yield strain for longitudinal loading (1.46 ± 0.19%) was 10% higher ($p = 0.01$, Student's *t*-test) than for transverse loading (1.33 ± 0.15%), indicating that shear yield strains were slightly anisotropic. However, there was no significant difference ($p = 0.20$) between the ultimate strains for the longitudinal (4.60 ± 0.77%) and transverse (4.24 ± 1.25%) trabecular orientations, indicating that the ultimate strains were isotropic.

		Longitudinal			Transverse		
Y	X	slope	intercept*	r^2	slope	intercept*	r^2
Shear modulus (MPa)	ρ	931	—	0.61	775	-158	0.64
	E	0.143	—	0.78	0.351	—	0.67
Elastic range (%)	G	—	—	—	—	—	—
	ρ	—	—	—	—	—	—
τ_{yield} (MPa)	G	9.88	—	0.80	8.72	0.681	0.83
	ρ	10.3	—	0.61	7.67	—	0.68
γ_{yield} (%)	G	-0.756	1.72	0.25	-0.647	1.52	0.20
	ρ	—	—	—	—	—	—
$\tau_{ultimate}$ (MPa)	G	14.2	1.39	0.83	13.1	1.04	0.84
	ρ	15.0	—	0.65	12.4	-2.36	0.80
$\gamma_{ultimate}$ (%)	G	-3.52	5.82	0.35	—	—	—
	ρ	—	—	—	—	—	—

*Intercepts are only reported when significantly different from zero ($p < 0.05$).
— regression was not significant ($p > 0.05$).

Table 1: Linear regressions ($Y = aX + b$) of shear properties against apparent density (ρ, g cm^{-3}) and either shear modulus (G, GPa) or Young's modulus (E, MPa), compared for longitudinal and transverse trabecular orientations. Relationships for failure stresses (τ, MPa) had statistically similar slopes in the longitudinal and transverse groups (analysis of covariance, $p > 0.05$). Failure strains (γ %) were independent of apparent density and only weakly dependent on shear modulus.

Material property	Longitudinal (n = 25) mean ± S.D. range adj. mean (S.E.M.)*	Transverse (n = 23) mean ± S.D. range adj. mean (S.E.M.)*	Transverse to longitudinal ratio†
Apparent density (g cm^{-3})	0.50 ± 0.11 0.25 – 0.65	0.59 ± 0.11 0.38 – 0.76	1.18 ‡
Shear modulus (MPa)	349 ± 128 99 – 535 384 (15)	296 ± 103 95 – 546 257 (16)	0.67 §
Young's modulus (MPa)	2470 ± 789 704 – 3700	719 ± 241 306 – 1300	0.29 §
Failure stresses (MPa):			
Yield stress	4.24 ± 1.42 1.37 – 7.18 4.61 (0.16)	3.26 ± 0.99 1.11 – 5.10 2.85 (0.17)	0.62 §
Ultimate stress	6.35 ± 2.00 2.22 – 9.83 6.92 (0.21)	4.92 ± 1.48 1.96 – 7.53 4.30 (0.22)	0.62 §
Failure strains (%):			
Elastic range	0.97 ± 0.23 0.46 – 1.35	0.80 ± 0.22 0.45 – 1.21	0.82 ¶
Yield strain	1.46 ± 0.19 1.07 – 1.78	1.33 ± 0.15 1.05 – 1.56	0.91 ¶
Ultimate strain	4.60 ± 0.77 2.96 – 6.00	4.24 ± 1.25 2.16 – 7.17	0.92 (No difference) **

*Adjusted means are only reported for properties where the slopes of the relationships with density were statistically similar for longitudinal and transverse loading (by analysis of covariance with density as covariate).
†Ratios are based on adjusted means for shear modulus and failure stresses; for Young's modulus and failure strains, comparisons were based on unpaired *t*-tests.
‡$p = 0.008$; §$p < 0.0001$; ¶$p = 0.01$; **$p = 0.2$.

Table 2: Comparison of mean values of the material properties for longitudinal and transverse trabecular orientations. All material properties, except apparent density and ultimate strain, were significantly lower for the transverse group.

2.3.2 Application of Shear Properties to Multiaxial Failure

The results described above for shear yield stresses were combined with results from tensile, compressive (Keaveny *et al.*, 1994b; Keaveny *et al.*, 1994c) and triaxial (Keaveny *et al.*, 1996) experiments to formulate the Tsai-Wu failure criterion for bovine tibial trabecular bone. Although linear relationships were reported above between apparent density and shear yield strengths, power law relationships provided similarly good correlations. Power laws were used to formulate the following relationships between the Tsai-Wu constants and apparent density:

$$
\begin{aligned}
F_1 &= \frac{1}{46.9\rho^{1.68}} - \frac{1}{86.4\rho^{1.99}} \\
F_2 = F_3 &= \frac{1}{(10.8\rho^{1.59})} - \frac{1}{(22.4\rho^{2.58})} \\
F_{11} &= \frac{1}{(46.9\rho^{1.68})(86.4\rho^{1.99})} \\
F_{22} = F_{33} &= \frac{1}{(10.8\rho^{1.59})(22.4\rho^{2.58})} \\
F_{44} = F_{66} &= \frac{1}{(7.39\rho^{1.58})^2} \\
F_{55} &= \frac{1}{(10.1\rho^{1.30})^2} \\
F_{12} = F_{13} &= \frac{-0.000734}{\rho^4} + 0.00398
\end{aligned}
\tag{11}
$$

For the case of biaxial stress with $\sigma_3 = 0$, at all densities, the major axis of the Tsai-Wu failure ellipsoid was nearly parallel to the line defining an axial to transverse stress ratio of about six (Fig. 6). However, the ellipsoid was more elongated at lower densities than at higher densities. Since the amount of elongation in the ellipsoid is controlled by the magnitude of the strength interaction term F_{12}, this result indicates that for biaxial stress

Figure 6: Plane through the Tsai-Wu failure surface for a biaxial state of stress, for three apparent densities (0.30 g cm^{-3}, inner envelope; 0.45 g cm^{-3}, middle envelope; 0.60 g cm^{-3}, outer envelope). At all densities, the major axis of the ellipsoid was aligned nearly parallel with the line defining an axial to transverse stress ratio of about six. At lower densities, the ellipsoid is more elongated than at higher densities. Since F_{12}, the strength interaction term, determines the level of elongation of the ellipsoid, this result indicates that there is more of a strength interaction effect at lower densities.

states, there is more of a multiaxial strength interaction effect at lower densities. The orientation and elongation of the failure envelopes for the triaxial, axisymmetric stress state were similar to the biaxial case (Fig. 7). However, the ratio of transverse to longitudinal stress at failure was lower for all densities in the triaxial case than in the biaxial case.

The dominant failure mode for off-axis compressive loading depended on the angle between the applied load and the primary trabecular orientation (Fig. 8). Using the maximum stress criterion and the measured shear yield stress, yielding in shear was predicted for angles between 6° and 62°, while yielding due to normal stresses was predicted for all other angles (Fig. 8B). When the shear yield stress was increased by 30% (therefore increasing the ratio of shear to compressive yield stress), yielding in shear was predicted for a slightly smaller range of angles (8° - 55°); when the shear yield stress was reduced by 30%, yielding in shear was predicted for a larger range of angles (4° - 69°). Although the maximum stress criterion did not allow for interaction between failure modes (as evidenced by slope discontinuities), the predicted yield stresses follow trends similar to those calculated from the Tsai-Wu criterion (Fig. 8C). Thus, if the failure behavior of trabecular bone is well-described by the Tsai-Wu criterion, the dominant failure mode will be shear when compressive loads are applied at approximately 6° - 62° oblique to the primary trabecular orientation.

2.4 Discussion

Based on trends measured for tensile and compressive failure of bovine tibial trabecular bone (Keaveny *et al.*, 1994b; Keaveny *et al.*, 1994c), it was hypothesized in this study that shear failure strains of bovine tibial trabecular bone are homogeneous and isotropic. It was also hypothesized that shear is a dominant failure mode when trabecular bone is loaded obliquely relative to its primary trabecular orientation. The results indicate that while failure stresses in shear were highly inhomogeneous and anisotropic, shear

Figure 7: Plane through the Tsai-Wu failure surface for a triaxial, axisymmetric state of stress for three apparent densities (0.30 g cm^{-3}, inner envelope; 0.45 g cm^{-3}, middle envelope; 0.60 g cm^{-3}, outer envelope). At all densities, the major axis of the ellipsoid was aligned nearly parallel with the line defining an axial to transverse stress ratio of about 11. As in the case of biaxial stress, the ellipsoid is more elongated at lower densities, indicating that there is more of a strength interaction effect at lower densities.

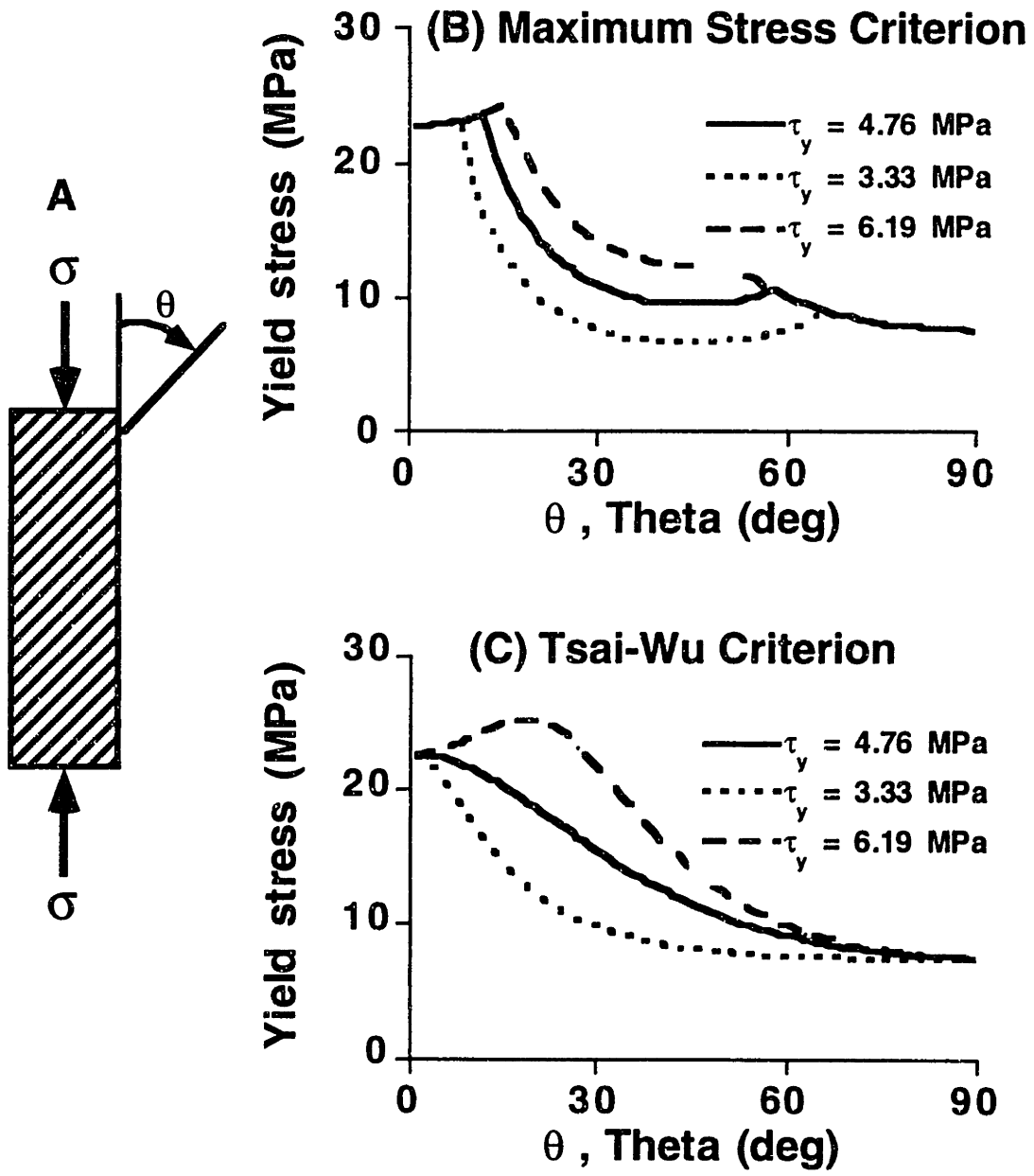

Figure 8: (A) Yield stresses were predicted for uniaxial compressive stresses σ acting from $\theta = 0°$ (longitudinal loading) to $\theta = 90°$ (transverse loading) relative to the primary trabecular orientation, using the measured shear yield strength values, and also using values 30% above and 30% below the measured value. Using the maximum stress criterion (B) and the measured shear yield stress, yielding in shear was predicted for angles between 6° and 62°; when the shear yield stress was increased, yielding in shear was predicted for a smaller range of angles (8° - 55°); when the shear yield stress was reduced, yielding in shear was predicted for a larger range of angles (4° - 69°). The predicted yield stresses from the maximum stress criterion follow trends similar to those based on the more complex and realistic Tsai-Wu criterion (C), which also predicts large changes in off-axis yield stress with changes in the ratio of shear to compressive yield stress.

failure strains were homogeneous and were either isotropic (ultimate) or only slightly anisotropic (yield). These results indicate that failure in shear can be predicted for (bovine tibial) trabecular bone of any density and orientation with knowledge of only its failure strains. The data for shear yield stresses were then used to formulate the Tsai-Wu multiaxial failure criterion for trabecular bone. Assuming that the Tsai-Wu criterion describes the failure behavior of trabecular bone under plane stress conditions, it was demonstrated that shear failure can dominate trabecular bone failure for a substantial range of off-axis compressive loading directions, and that this range depends on the magnitude of the shear yield stress.

The use of a custom rotational displacement transducer system and a reduced-section cylindrical geometry eliminated end-artifacts and biased failure to a region of constant surface stress, resulting in a higher level of accuracy in the measurement of trabecular bone shear properties than has been achieved previously. By harvesting specimens from 36 different bones, the data also provide a good representation of the behavior of bovine proximal tibial bone in general. Since longitudinal and transverse specimens were not selected randomly from identical sites within the tibia, there may be architectural differences between groups which introduced a bias into the comparisons for different orientations. However, the most structurally important differences between groups were in apparent density and the direction of the primary trabecular orientation. Since failure strengths were adjusted for inter-group differences in apparent density, the comparisons for different trabecular orientations should closely reflect the anisotropy of trabecular bone. It should also be noted that the absolute values of the reported properties may be somewhat inaccurate relative to the *in vivo* situation because *in vivo* boundary conditions can never be simulated exactly with excised trabecular bone specimens.

One possible limitation of the results is their applicability to human bone, due to differences in apparent density and architecture between human and bovine bone. The mean ($\pm$ S.D.) wet apparent density of 0.54 ± 0.11 g cm^{-3} of the specimens used here is higher

than those reported for the human lumbar spine, 0.19 ± 0.08 g cm^{-3}* (Hansson *et al.*, 1987) and proximal tibia, 0.26 ± 0.14 g cm^{-3}* (Ashman *et al.*, 1989), although the densities reported here are similar to those reported for the human proximal femur, 0.50 ± 0.16 g cm^{-3}* (Rohlmann *et al.*, 1980). Since failure stresses are highly dependent on apparent density, the failure stress results should be extrapolated carefully (if at all) to densities below the measured values. However, since failure strains were independent of apparent density, the mean failure strain values reported here may apply to low density human bone. Differences in architecture must also be considered when extrapolating the results to human bone, since the failure mechanisms at the trabecular level may differ. The substantial overlap of failure strains for longitudinal and transverse trabecular orientations, however, suggests that shear failure strains may be independent of architecture.

The mean values for ultimate shear stress and shear modulus agree with values reported by previous investigators (Table 3). The mean ultimate strength for longitudinal specimens (6.35 ± 1.89 MPa) agrees best with the value of 6.60 ± 1.66 MPa reported by Stone *et al.* (1983) for bovine humeral bone, most likely due to similarities in density and trabecular orientation between the two studies. The slightly lower values reported by Saha and Gorman (1981) are probably due to their use of lower density human bone. The shear modulus values also compare favorably with those measured by ultrasound for the bovine femur (Ashman *et al.*, 1987). Although values for shear failure strains have not been reported, previous investigators have concluded that compressive failure strains are isotropic (Turner, 1989) or slightly anisotropic (Mosekilde *et al.*, 1987), which is in general consistent with the results for shear failure strains.

The combination of data presented in this chapter for shear yield stresses with data for tensile, compressive and triaxial loading to formulate the Tsai-Wu failure criterion represents a significant advance in the application of multiaxial failure theory to trabecular bone. In particular, the failure criterion described here can be used to predict failure for any

* Dry apparent density values reported in these studies were converted to wet apparent density based on the data of Galante *et al.* (1970).

state of multiaxial stress and for a specimen of any apparent density. However, extrapolation of the failure surface to densities outside the range used to formulate the criterion (approximately 0.4 - 0.8 g cm^{-3}) may result in inaccurate predictions of failure stresses. In addition to its limitation to relatively high density bone, the formulation described here may not be applicable to trabecular bone with different architecture than bovine tibial bone. Therefore, additional experimental work is required to determine the multiaxial failure behavior of human bone for various anatomic sites. Finally, although the Tsai-Wu failure criterion has been formulated for trabecular bone, its predictive accuracy has not been evaluated in prospective tests, which should occur before the criterion can be effectively used in predicting structural failure of whole bones.

The prediction that shear can dominate failure during off-axis loading may have implications for traumatic failure of bones, particularly age-related hip fractures. Although the analysis using the maximum stress criterion did not take into account interactions between failure modes (as evidenced by slope discontinuities in Fig. 8B), the predictions are consistent with those based on the more realistic Tsai-Wu criterion. Therefore, although one mode is not necessarily solely responsible for failure, the results indicate that shear can dominate trabecular bone failure for a relatively large range of off-axis loading directions. If this prediction holds for human bone, then failure of trabecular bone *in vivo* during traumatic, off-axis loading (such as in the proximal femur during falls) may be dominated by shear failure. The results also indicate that if changes in trabecular structure with aging degrade shear properties more than compressive properties — which may occur as the body attempts to maintain maximum structural capacity for habitual activities — then shear will dominate trabecular bone failure for an even larger range of off-axis loading. Therefore, efforts to understand and predict the failure properties of the proximal femur under traumatic loading conditions may be improved by considering the shear as well as compressive properties of the trabecular bone.

2.5 References

Ashman R. B., Corin J. D., and Turner C. H. (1987) Elastic properties of cancellous bone: measurement by an ultrasonic technique. *J Biomech* **20**, 979-986.

Ashman R. B., Rho J. Y., and Turner C. H. (1989) Anatomical variation of orthotropic elastic moduli of the proximal human tibia. *J Biomech* **22**, 895-900.

Cheal E. J., Spector M., and Hayes W. C. (1992) Role of loads and prosthesis material properties on the mechanics of the proximal femur after total hip arthroplasty. *J Orthop Res* **10**, 405-422.

Halawa M., Lee A. J. C., Ling R. S. M., and Vangala S. S. (1978) The shear strength of trabecular bone from the femur, and some factors affecting the shear strength of the cement-bone interface. *Archives of Orthopaedic and Traumatic Surgery* **92**, 19-30.

Hansson T., Keller T., and Panjabi M. (1987) A study of the compressive properties of lumbar vertebral trabeculae: Effects of tissue characteristics. *Spine* **12**, 56-62.

Hvid I., Bentzen S. M., Linde F., Mosekilde L., and Pongsoipetch B. (1989) X-ray quantitative computed tomography: the relations to physical properties of proximal tibial trabecular bone specimens. *J Biomech* **22**, 837-844.

Hvid I., Jensen N., Bunger C., Solund K., and Djurhuus J. (1985) Bone mineral assay: its relation to the mechanical strength of cancellous bone. *Eng Med* **14**, 79-83.

Jones R. (1975) Maximum stress theory. In *Mechanics of Composite Materials*, 72-74, Scripta Book Company, Washington, D.C.

Keaveny T., Wachtel E., and Zadesky S. (1996) Multiaxial failure characteristics of trabecular bone. *Trans 42nd ORS* **21**, 81.

Keaveny T. M., Guo X. E., Wachtel E. F., McMahon T. A., and Hayes W. C. (1994a) Trabecular bone exhibits fully linear elastic behavior and yields at low strains. *J Biomech* **27**, 1127-1136.

Keaveny T. M., Wachtel E. F., Cutler M. J., and Pinilla T. P. (1994b) Yield strains for bovine trabecular bone are isotropic but asymmetric. *Trans 40th ORS* **19**, 428.

Keaveny T. M., Wachtel E. F., Ford C. M., and Hayes W. C. (1994c) Differences between the tensile and compressive strengths of bovine tibial trabecular bone depend on modulus. *J Biomech* **27**, 1137-1146.

Lotz J. C., Cheal E. J., and Hayes W. C. (1991) Fracture prediction for the proximal femur using finite element models: Part 1-Linear analysis. *J Biomech Eng* **113**, 353-360.

Mosekilde L., Mosekilde L., and Danielsen C. (1987) Biomechanical competence of vertebral trabecular bone in relation to ash density and age in normal individuals. *Bone* **8**, 79-85.

Nadai A. (1950) Torsion of a Round Bar. The Stress-Strain Curve in Shear. In *Theory of Flow and Fracture of Solids*, McGraw-Hill Book Company, Inc., New York.

Rohl L., Larsen E., Linde F., Odgaard A., and Jorgensen J. (1991) Tensile and compressive properties of cancellous bone. *J Biomechanics* **24**, 1143-1149.

Rohlmann A., Zilch H., Bergmann G., and Kolbel R. (1980) Material properties of femoral cancellous bone in axial loading. Part I: Time independent properties. *Arch Orthop Trauma Surg* **97**, 95-102.

Saha S. and Gorman P. H. (1981) Strength of human cancellous bone in shear and its reiationship to bone mineral content. *Trans. 27th ORS* **6**, 217.

Stone J. L., Beaupre G. S., and Hayes W. C. (1983) Multiaxial strength characteristics of trabecular bone. *J Biomech* **16**, 743-752.

Tsai S. W. and Wu E. M. (1971) A general theory of strength for anisotropic materials. *J Comp Mater* **5**, 58-80.

Turner C. (1989) Yield behavior of bovine cancellous bone. *J Biomech Eng* **111**, 256-260.

Chapter 3

Uniaxial Strength Asymmetry in Cellular Materials: An Analytical Model

3.1 Introduction

Both natural and engineering cellular solids bear mechanical loads. Successful design of engineering cellular materials requires an understanding of their response to load, in particular how their stiffness and strength relate to those of the solid from which they are made, to their relative density and to their cell geometry. Analytical models based on the microstructural mechanisms responsible for observed macroscopic behavior are useful in designing materials with appropriate properties for specific applications. The development of microstructural models that explain material strength behavior is essential for accurate prediction of failure in both natural and engineered structures.

Some cellular materials have different uniaxial tensile and compressive strengths. This strength asymmetry may arise as a result of the cellular material failing by different mechanisms in tension and compression (Gibson and Ashby, 1988). Flexible polyurethane foams, for instance, typically fail by yielding in tension and by elastic buckling in compression: then the tensile yield strength is greater than the compressive elastic collapse strength and the degree of strength asymmetry decreases as the relative density increases. Brittle ceramic foams often fail by brittle fracture in tension and by brittle crushing in compression; if there is a pre-existing crack in the material, the tensile fracture strength is less than the compressive crushing strength. Strength asymmetry may also arise in cellular solids which fail by the same mechanisms in tension and compression but which are made up of a solid with different tensile and compressive strengths. Examples include trabecular bone (Stone *et al.*, 1983; Kaplan *et al.*, 1985; Keaveny *et al.*, 1994) and rigid polyurethane

foams (Triantafillou *et al.*, 1989). Both are stronger in compression than in tension and both show considerable ductility, suggesting that failure is by yielding or microcracking. The degree of strength asymmetry increases with relative density (Fig. 1). Here, the strength asymmetry in cellular solids arising from a difference in the tensile and compressive yield strength of the cell wall material is described. First, strength asymmetry is modeled in a simple, two-dimensional honeycomb, and then these results are extended to three dimensions using a tetrahedral unit cell to represent open-cell foams.

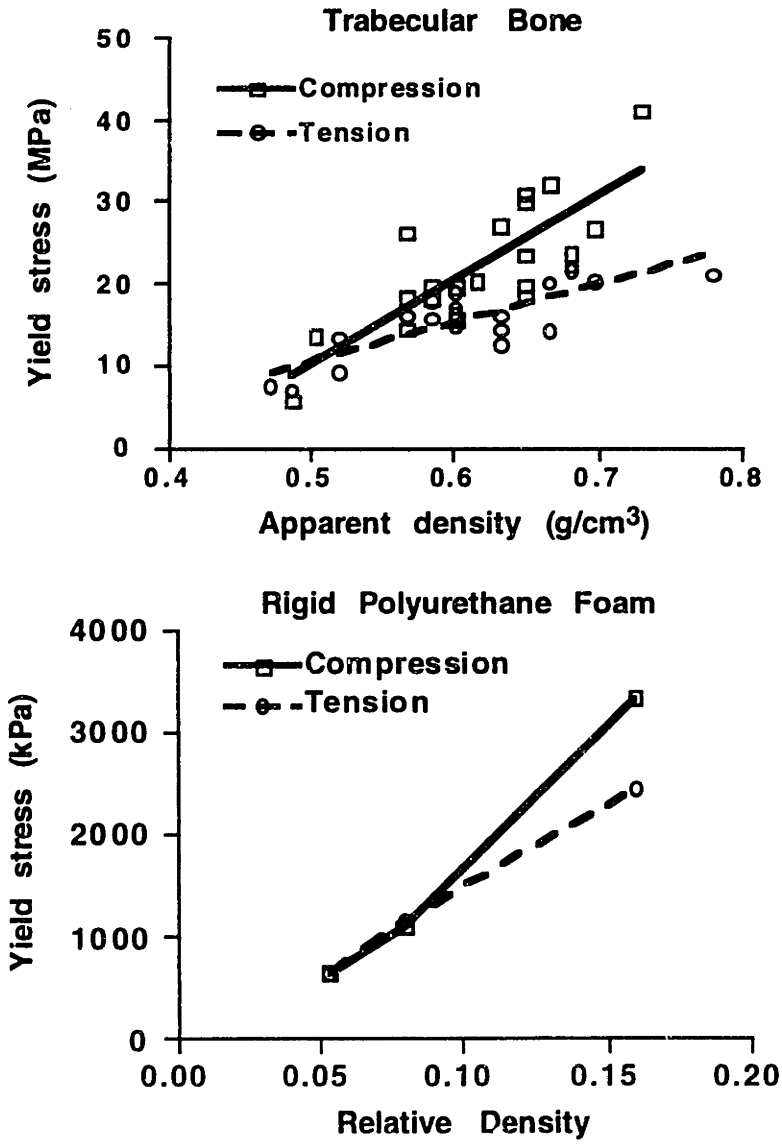

Figure 1: Compressive and tensile yield strength plotted against density for trabecular bone (Keaveny *et al.*, 1994) and rigid polyurethane foam (Triantafillou *et al.*, 1989). Both materials exhibit compression-strong strength asymmetry that increases with density.

3.2 Analysis: Honeycombs

The uniaxial yield strength of hexagonal honeycombs is analyzed first, allowing for differences in the tensile and compressive yield strengths of the cell wall material, using the method of Gibson and Ashby (1988). They neglected the effect of axial stresses within the cell wall, which leads to equal tensile and compressive yield strengths in the honeycomb, even for differing tensile and compressive strengths in the cell wall material. As shown below, strength asymmetry in the honeycomb results from the presence of the axial stress in the oblique struts; it increases with increasing ratio of the axial to the bending stresses.

The unit cell of a regular, isotropic honeycomb is shown in Fig. 2a; anisotropy is introduced by changing either h/l or θ (Fig. 2b). The relative density of the honeycomb is given by

$$\frac{\rho^*}{\rho_s} = \frac{(2+h/l)}{2\cos\theta(h/l+\sin\theta)}\frac{t}{l} \tag{1}$$

The application of a remote uniaxial stress σ_2 in the X_2-direction (Fig. 2) produces both a bending moment M and an axial stress σ_a on the inclined member of the unit cell (Fig. 3), given by

$$M = \frac{Pl\cos\theta}{2} \tag{2}$$

$$\sigma_a = \frac{P\sin\theta}{bt} \tag{3}$$

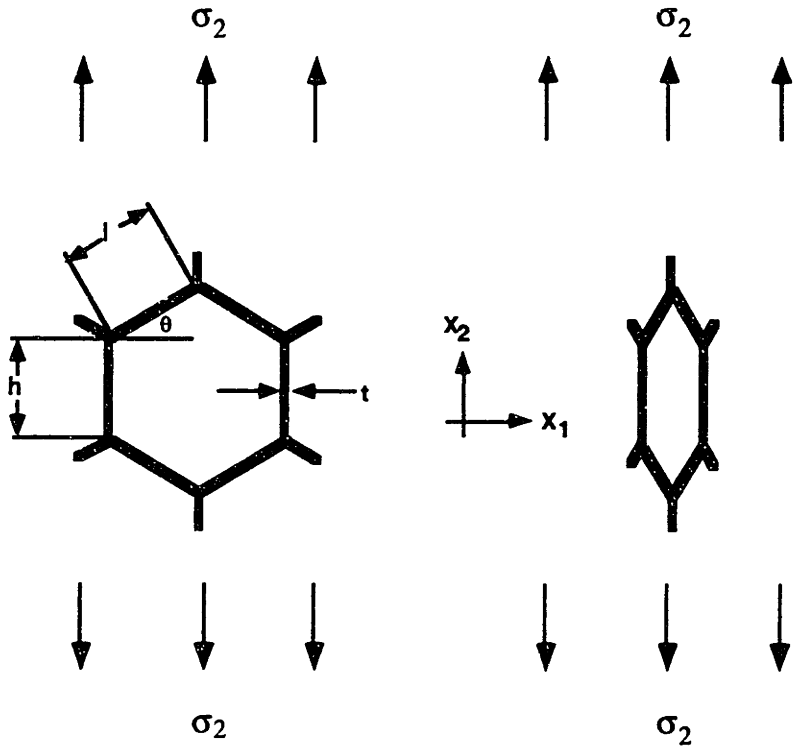

Figure 2: Unit cells of hexagonal honeycombs used for modeling strength asymmetry. The cell shape is described by parameters h/l and θ; the relative density is proportional to the aspect ratio of the cell walls t/l. (A) Regular, isotropic unit cell with $h/l = 1$ and $\theta = 30°$. (B) Anisotropic unit cell. Anisotropy is introduced when either $h/l \neq 1$ or $\theta \neq 30°$.

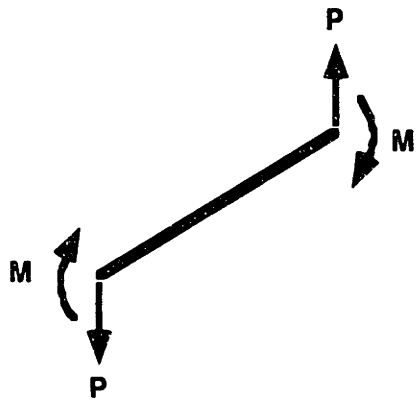

Figure 3: The application of a remote uniaxial stress in the vertical (X_2) direction produces bending moments M and forces P on the inclined members of the honeycomb unit cell.

where P is the vertical force applied to the oblique strut and $\sigma_2 = P/b\ell\cos\theta$. Failure occurs when the cell wall has yielded across its entire section (Fig. 4). The depth of the neutral axis c is given by

$$c = \frac{t\left(\sigma_{ys}^{c} + \sigma_a\right)}{\sigma_{ys}^{c} + \sigma_{ys}^{t}} \tag{4}$$

where σ_{ys}^{c} and σ_{ys}^{t} are the compressive and tensile yield strengths (absolute value) of the cell wall material, respectively. The moment required to cause formation of a plastic hinge is then given by the force, F, times the moment arm, $t/2$:

$$M_p = \left(\sigma_{ys}^{t} - \sigma_a\right)\frac{bct}{2} \tag{5}$$

or

$$M_p = \frac{bt^2}{2}\left(\frac{\sigma_{ys}^{t}\sigma_{ys}^{c} + \left(\sigma_{ys}^{t} - \sigma_{ys}^{c}\right)\sigma_a - \sigma_a^2}{\sigma_{ys}^{t} + \sigma_{ys}^{c}}\right) \tag{6}$$

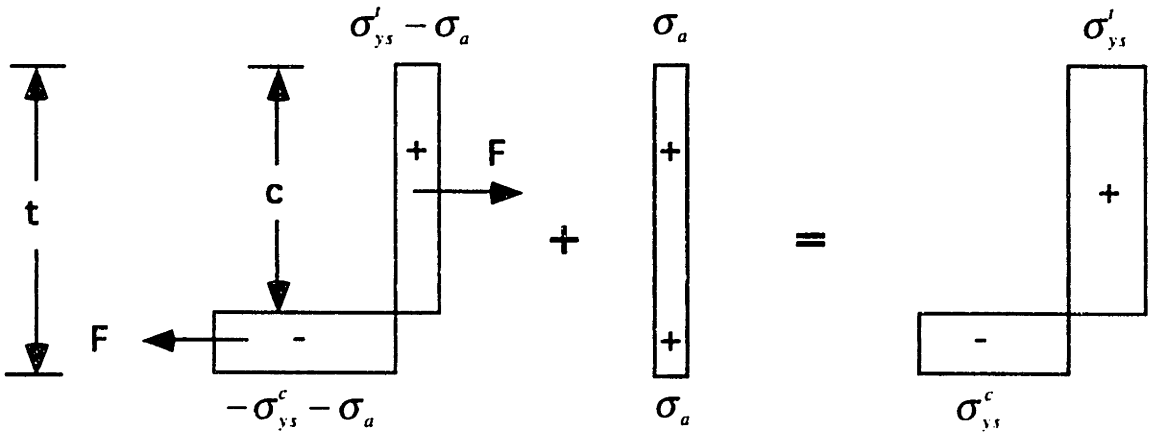

Figure 4: The bending, axial and total stress distributions across the section of an oblique strut that has failed as a result of plastic hinge formation. The depth of the neutral axis c is found by equating forces above and below the neutral axis.

By equating the applied moment M (Eqn. 2, which can be positive or negative) and the plastic moment M_p (Eqn. 6), the equation governing the uniaxial tensile and compressive strengths σ_2^* of the honeycomb is obtained:

$$\pm\left(\frac{\sigma_2^* \cos^2\theta}{(t/l)^2}\right) = \frac{1}{\sigma_{ys}^c + \sigma_{ys}^t}\left[\sigma_{ys}^t\sigma_{ys}^c + (l/t)\sigma_2^*\cos\theta\sin\theta\left(\sigma_{ys}^t - \sigma_{ys}^c\right) - (l/t)^2\left(\sigma_2^*\right)^2\cos^2\theta\sin^2\theta\right] \tag{7}$$

Note that if the axial stress within the cell wall is zero ($\sigma_a = 0$) the second and third terms within the square brackets of Equation (7) vanish and the tensile and compressive strengths of the honeycomb are identical.

The analysis for loading in the X_1 direction (Fig. 2) directly parallels that for the X_2 direction. The equation governing the uniaxial strengths σ_1^* is:

$$\pm\left(\frac{\sigma_1^*(h/l+\sin\theta)\sin\theta}{(t/l)^2}\right) = \frac{1}{\sigma_{ys}^c + \sigma_{ys}^t}\left[\sigma_{ys}^t\sigma_{ys}^c + (l/t)\sigma_1^*(h/l+\sin\theta)\cos\theta\left(\sigma_{ys}^t - \sigma_{ys}^c\right) - (l/t)^2\left(\sigma_1^*\right)^2(h/l+\sin\theta)^2\cos^2\theta\right] \tag{8}$$

To demonstrate the effects of geometry on strength asymmetry, tensile and compressive strengths of the honeycomb σ_2^* (normalized by the compressive strength of the cell wall material σ_{ys}^c) were calculated as a function of t/l for values of h/l from 0.5 to 3 (with θ = 30°), for values of θ from 30° (isotropic case) to 75° (with h/l = 1), and for an extreme case of anisotropy where h/l = 3 and θ = 75°. These analyses were performed assuming that the compressive strength of the cell wall material was 40% higher than the tensile strength (R = $\sigma_{ys}^c/\sigma_{ys}^t$ = 1.4). The effect of cell wall material properties was examined by varying R from 1.1 to 1.7.

3.3 Results: Honeycomb

In all cases, the honeycomb model predicted an increase in the strength differential with an increase in relative density for loading in the X_2 direction (Fig. 5). For a given relative density, anisotropic honeycombs had higher absolute normalized strengths as well as a higher degree of strength asymmetry than the isotropic honeycomb (Fig. 5a). Increases in both geometric parameters (h/l and θ) caused increases in the uniaxial strengths of the honeycomb as well as approximately linear increases in the ratio of compressive to tensile strength of the honeycomb (Figs. 5b, 5c). Increases in h/l had a relatively small effect on the ratio of compressive to tensile strength of the honeycomb, with an increase in strength ratio from 1.04 to 1.08 with an increase in h/l from 0.5 to 3.0 (at a relative density of 0.3, Fig. 5b). An increase in the oblique strut angle θ from 30° to 75° resulted in a larger increase in the strength ratio of the honeycomb, from 1.05 to 1.14 at a relative density of 0.3 (Fig. 5c). The parameter with the largest effect on the predicted honeycomb strength ratio was the ratio of the compressive and tensile strengths of the cell wall material R. An increase in this ratio from 1.1 to 1.7 caused an increase in the strength ratio of the isotropic honeycomb from 1.02 to 1.08 and a much larger increase from 1.04 to 1.24 in the highly anisotropic honeycomb, both at a relative density of 0.3 (Fig. 5d).

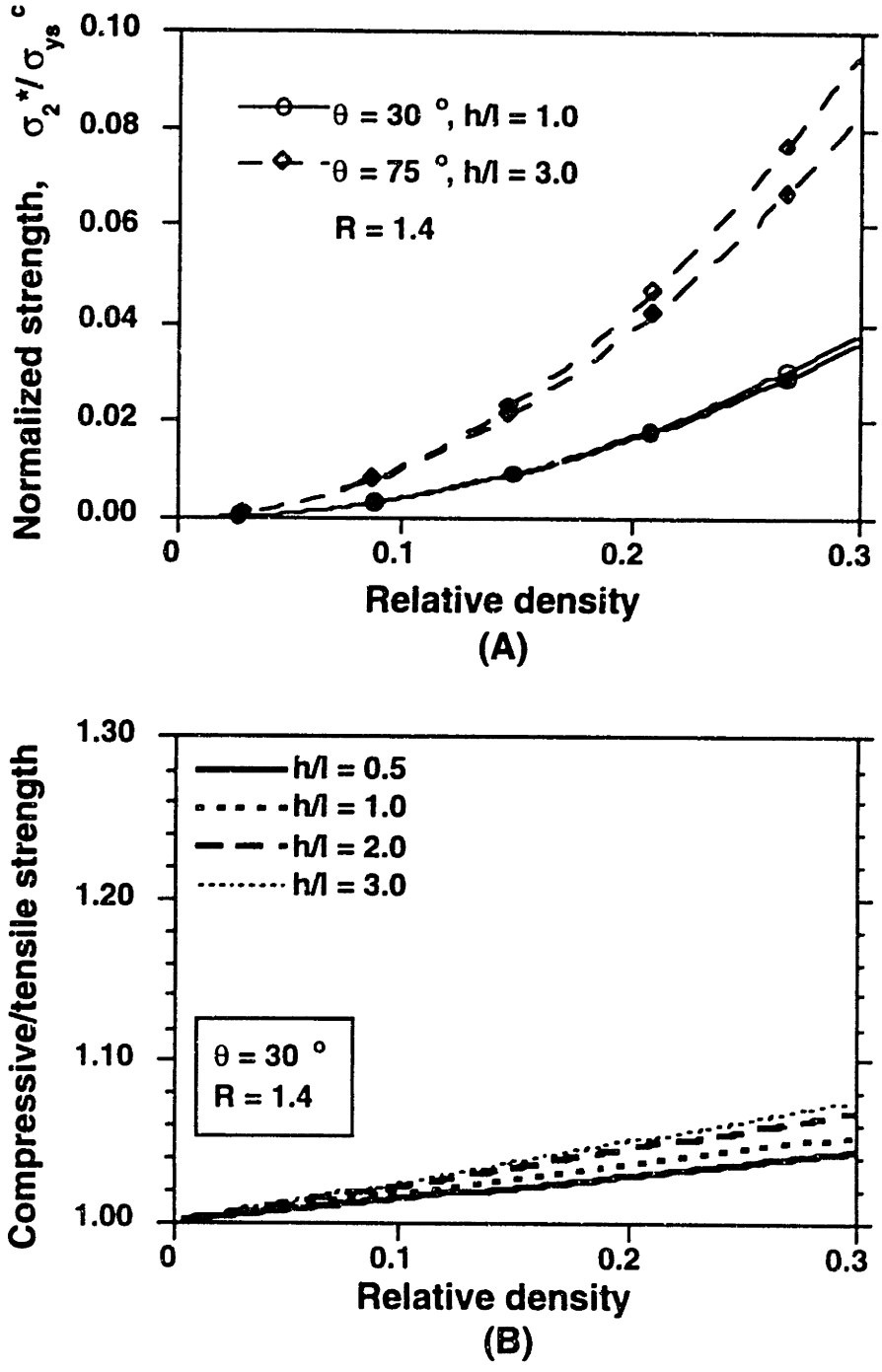

Figure 5: Strength asymmetry results for honeycomb model, for loading in the X_2 direction (A) Compressive (open symbols) and tensile (filled symbols) yield strengths of honeycomb plotted against relative density, for the isotropic case (θ = 30° and h/l = 1) and a highly anisotropic case (θ = 75° and h/l = 3.0), with a ratio of compressive to tensile strength of the cell wall material R of 1.4. Yield strengths were normalized by the compressive strength of the cell wall material, σ_{ys}^c. (B) Ratio of compressive to tensile strength of the honeycomb plotted against relative density for values of h/l from 0.5 to 3.0.

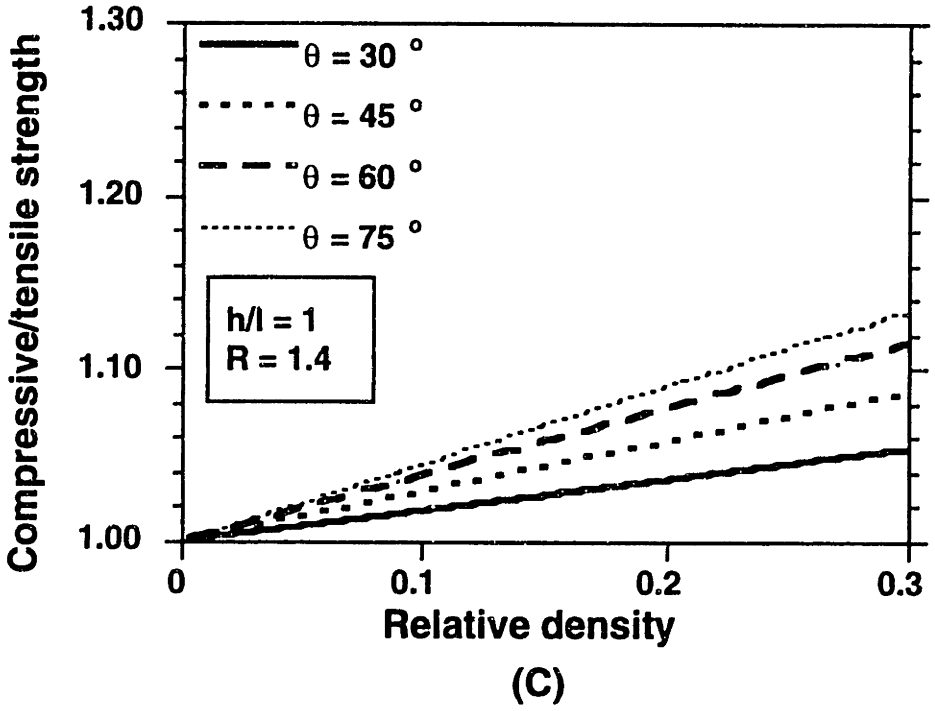

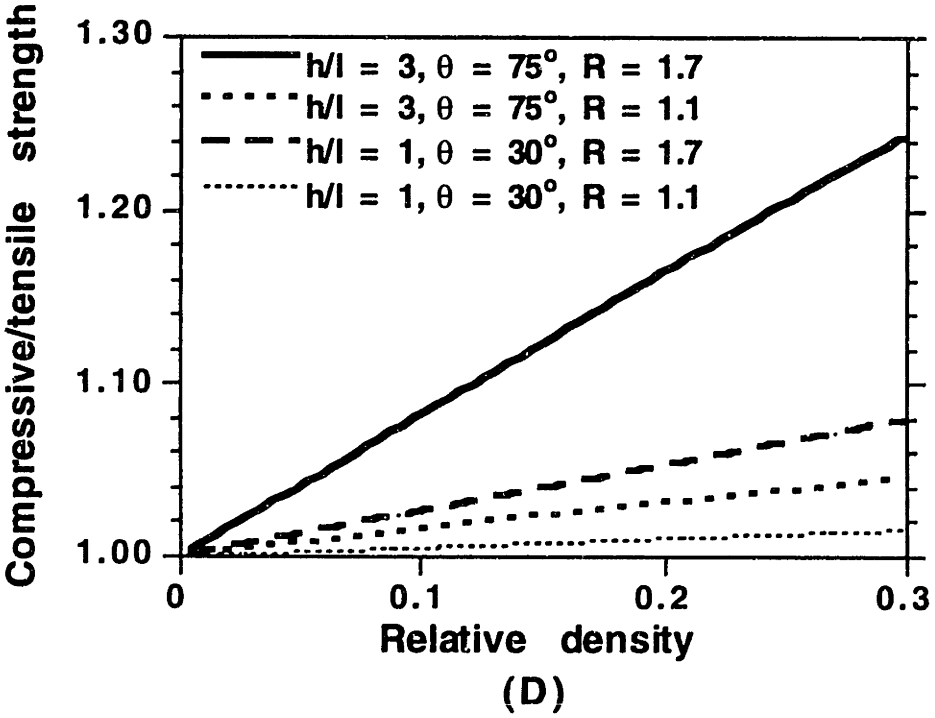

Figure 5: Strength asymmetry results for honeycomb model. (C) Strength ratio of the honeycomb plotted against relative density for values of θ from 30° (isotropic case) to 75°. (D) Strength ratio of the honeycomb plotted against relative density for values of R (ratio of compressive to tensile strength of the cell wall material) equal to 1.1 and 1.7, both for the isotropic case ($h/l = 1$, $\theta = 30°$) and a highly anisotropic case ($h/l = 3$, $\theta = 75°$).

3.4 Analysis: Open-cell foam

The mechanisms of deformation and failure in open-cell foams are similar to those in honeycombs. Since strength asymmetry arises from combined axial forces and bending moments in oblique struts, it is assumed that a microstructural element comprised of a single vertical strut with three oblique struts joining at equal angles captures the essential features of the mechanical behavior of open-cell foams (Fig. 6a). This representative microstructural element is now analyzed using dimensional arguments.

Each strut has a square cross section of width t. A tetrahedral element (Fig. 6a), with four struts of equal length meeting at equal tetrahedral angles, is similar to that analyzed by Warren and Kraynik (1988). Struts of unequal lengths, or at angles other than the tetrahedral angle, model more anisotropic foams (Fig. 6b).

In a manner similar to the honeycomb analysis, a single oblique strut is isolated, and the applied moment (due to the application of a remote uniaxial stress σ_2) is equated with the moment required to form a plastic hinge. The applied moment and axial force in the oblique strut due to the application of a remote uniaxial stress σ_2 (Fig. 7) are given by:

$$M = \frac{P}{6} l \cos\theta \tag{9}$$

$$\sigma_a = \frac{P \sin\theta}{3t^2} \tag{10}$$

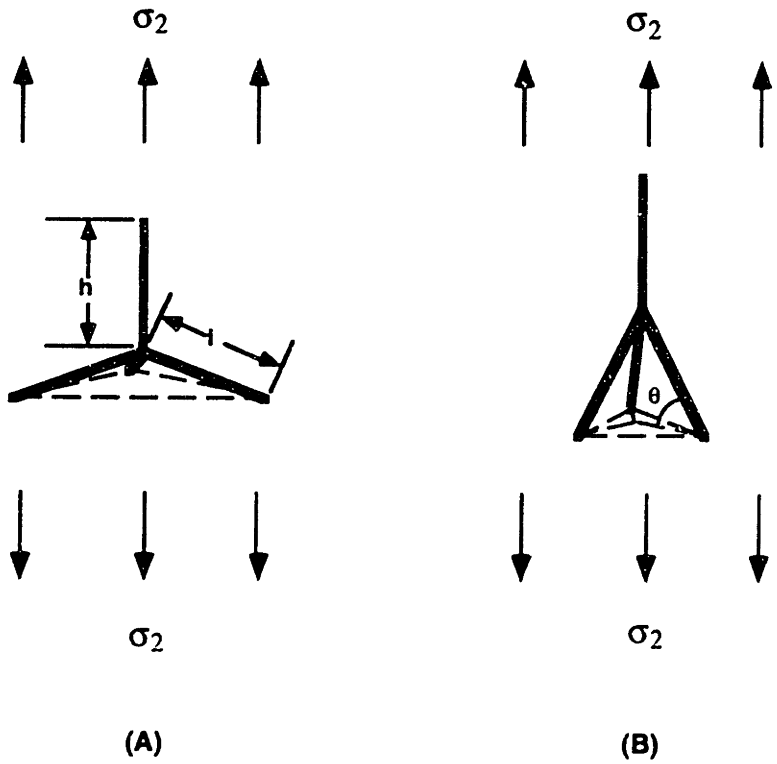

Figure 6: Microstructural element used to study strength asymmetry in open-cell foams. Each strut has a square cross section with width *t*. (A) Four struts of equal length meet at equal tetrahedral angles, similar to the microstructural element analyzed by Warren and Kraynik (1988). (B) Struts of unequal lengths, or at angles other than the tetrahedral angle, model more anisotropic foams.

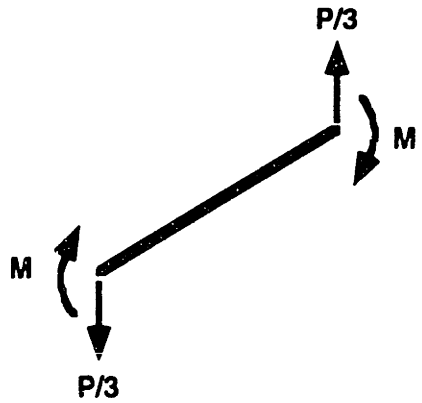

Figure 7: The application of a remote uniaxial stress in the vertical (X_2) direction produces bending moments M and forces P/3 on each inclined member of the microstructural element (total vertical force on the microstructural element = P).

It is assumed that for a single microstructural element, the remote stress acts over an area proportional to $(l\cos\theta)^2$, and therefore $P = k\sigma_2 l^2 \cos^2\theta$, where k is an unknown constant of proportionality. The relative density of the foam is proportional to $(t/l)^2$. The depth of the neutral axis is given by Equation 4 (Fig. 4). The moment required to form a plastic hinge is given by:

$$M_p = \frac{t^3}{2}\left(\frac{\sigma^t_{ys}\sigma^c_{ys} + \left(\sigma^t_{ys} - \sigma^c_{ys}\right)\sigma_a - \sigma_a^2}{\sigma^t_{ys} + \sigma^c_{ys}}\right) \tag{11}$$

which is simply Equation 6 defining the plastic moment for the honeycomb with b replaced by the strut edge length t. By equating the applied moment (Eqn. 9) and the plastic moment (Eqn. 11), the following equation governing the uniaxial strengths σ_2^* of the open-cell foam is obtained:

$$\pm\frac{k}{3}\sigma_2^* l^3\cos^3\theta = \tag{12}$$

$$\frac{t^3}{\left(\sigma^c_{ys} + \sigma^t_{ys}\right)}\left[\sigma^c_{ys}\sigma^t_{ys} + \frac{k}{3}\sigma_2^*(l/t)^2\left(\sigma^t_{ys} - \sigma^c_{ys}\right)\cos^2\theta\sin\theta - \left(\frac{k}{3}\right)^2\left(\sigma_2^*\right)^2(l/t)^4\cos^4\theta\sin^2\theta\right]$$

For the open-cell foam model, normalized strengths were calculated as a function of t/l for values of h/l from 0.5 to 3 (with θ = 19°), values of θ from 19° (tetrahedral angle) to 75° (with h/l = 1), and for an extreme case of anisotropy where h/l = 3 and θ = 75°. As with the honeycomb, these analyses were performed assuming that the compressive strength of the cell wall material was 40% higher than the tensile strength (R = $\sigma^c_{ys}/\sigma^t_{ys}$ = 1.4). The effect of cell wall material properties was examined by varying R from 1.1 to 1.7. Since the parameter k affects only the absolute value of the predicted strengths and not the ratio of the compressive to tensile strength, k was assumed to be unity in all analyses.

3.5 Results: Open-cell Foam

Results for the open-cell foam model were qualitatively similar to those for the honeycomb model. Strength asymmetry increased with t/l in each case, and was more pronounced when the foam was more anisotropic (Fig. 8a). An increase in h/l from 0.5 to 3.0 did not affect the ratio of compressive to tensile strength of the foam (Fig. 8b), a result which was expected because the parameter h/l affects only the relative density of the material and not its uniaxial strengths. An increase in θ from 19° (isotropic case) to 75° caused an increase in the predicted strength ratio (an increase from 1.04 to 1.15 at a relative density of 0.3, Fig. 8c). An increase in R from 1.1 to 1.7 caused an increase in strength ratio from 1.01 to 1.06 in the more isotropic foam, and a much larger increase from 1.08 to 1.48 in the highly anisotropic foam (at t/l = 0.3, Fig. 8d).

3.6 Discussion

The objective of this chapter was to determine the mechanisms responsible for compression-strong strength asymmetry in cellular materials, and to describe the way in which strength asymmetry depends on relative density, cell geometry, and cell wall material properties. By incorporating different tensile and compressive strengths of the cell wall material into honeycomb and open-cell foam models, it was demonstrated that density-dependent differences between tensile and compressive strengths of a cellular material arise when oblique struts are loaded simultaneously by axial forces and bending moments. Increases in the alignment of the oblique struts with the direction of loading (resulting in an increase in the amount of axial relative to bending force) caused a decrease in the ratio of tensile to compressive strength of the material. In the limit where struts are perfectly aligned with the direction of loading, the material would be expected to exhibit strength asymmetry equal to the strength asymmetry of the solid cell wall material. However, increases in the

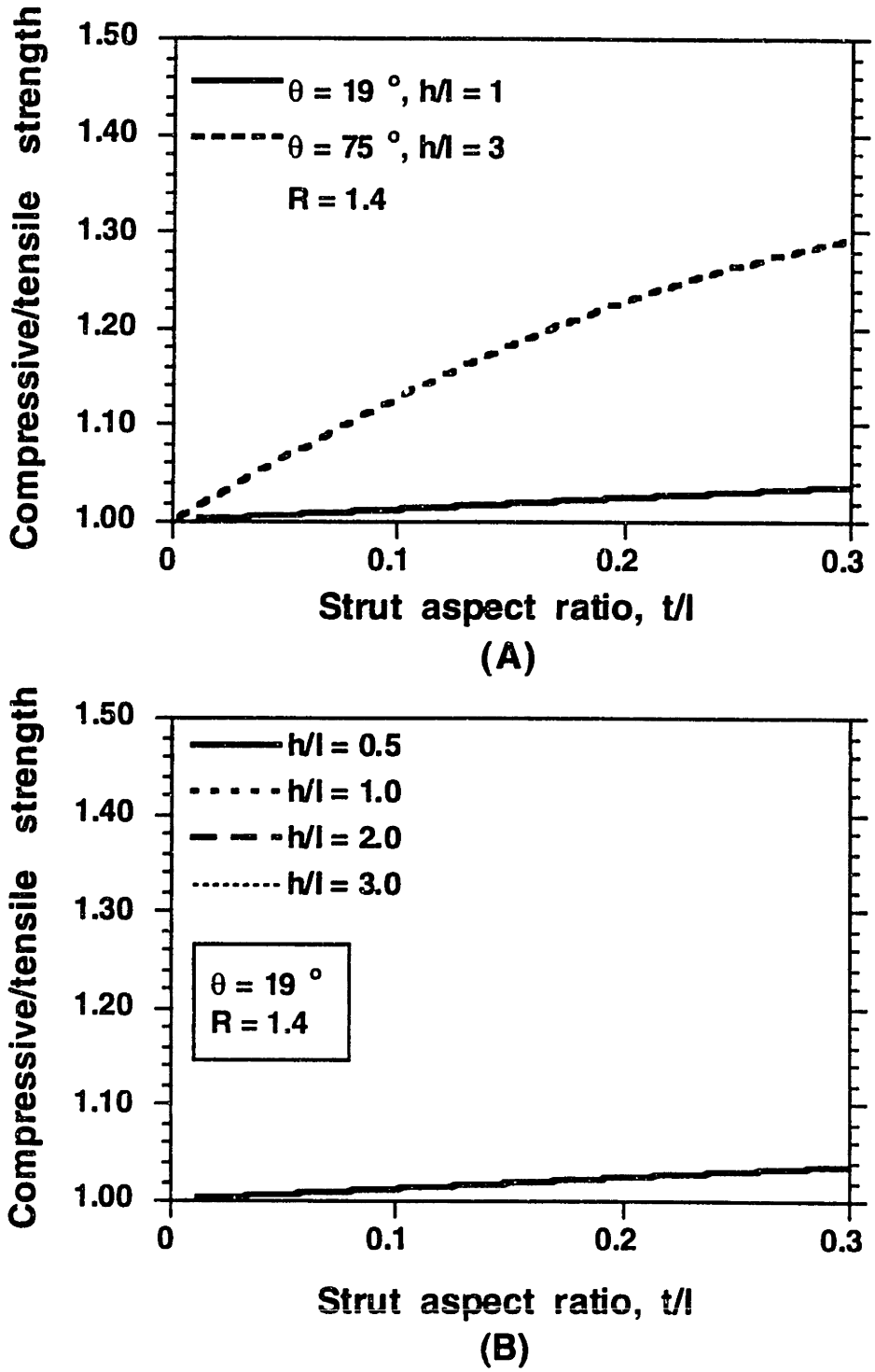

Figure 8: Strength asymmetry results for open-cell foam model, for loading in the X_2 direction. (A) Ratio of compressive and tensile yield strengths of the foam versus relative density, for the tetrahedral case (θ = 19° and h/l = 1) and a highly anisotropic case (θ = 75° and h/l = 3.0), with a ratio of compressive to tensile strength of the cell wall material R of 1.4. (B) Ratio of compressive to tensile strength of the foam plotted against the strut aspect ratio t/l for values of h/l from 0.5 to 3.0.

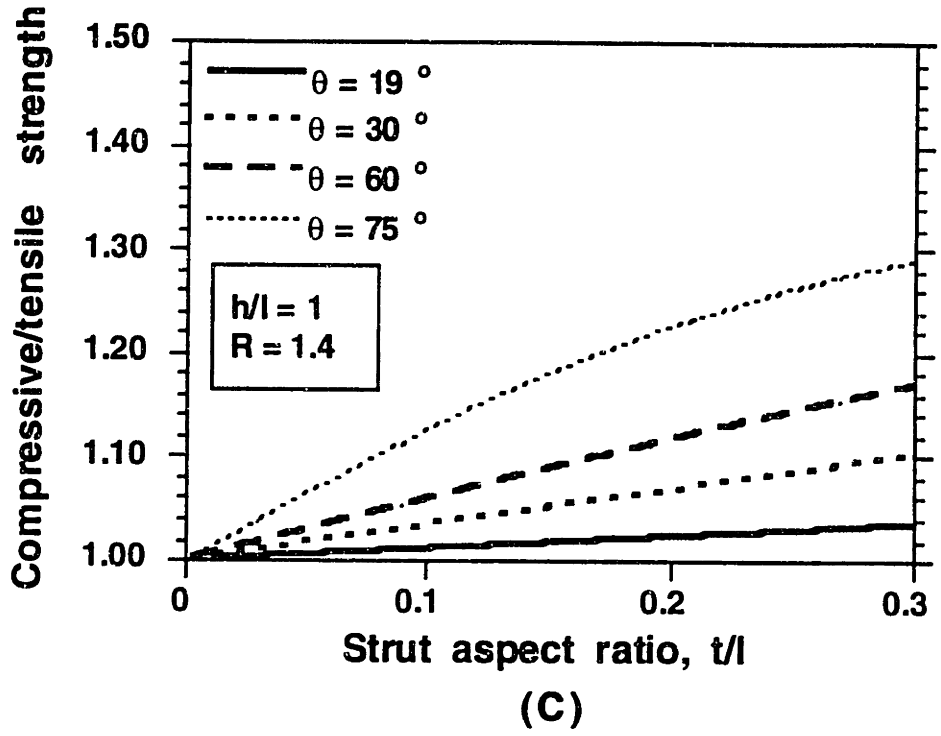

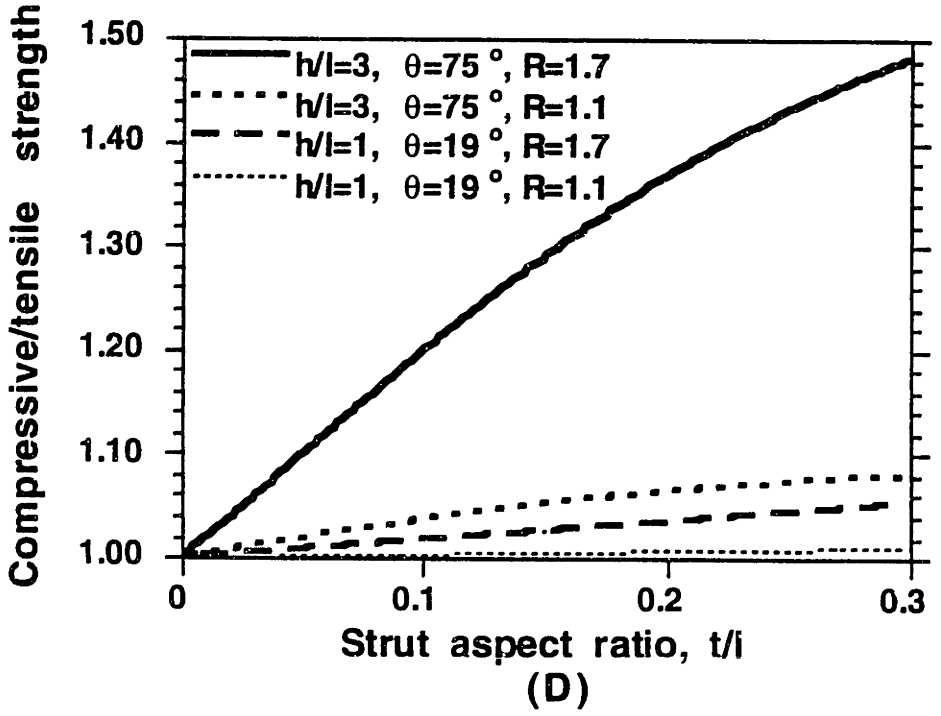

Figure 8: Strength asymmetry results for open-cell foam model. (C) Strength ratio of the foam plotted against t/l for values of θ from 19° (tetrahedral angle) to 75°. (D) Strength ratio of the foam plotted against t/l for values of R (ratio of compressive to tensile strength of the cell wall material) equal to 1.1 and 1.7 for the tetrahedral case (h/l = 1, θ = 19°) and a highly anisotropic case (h/l = 3, θ = 75°).

relative density of such a material (by increasing the strut aspect ratio t/l) would result in no differences in the ratio of tensile to compressive strength. Therefore, *both* bending moments *and* axial forces in the struts, combined with strength asymmetry of the cell wall material, are necessary to explain the density-dependent strength asymmetry that has been observed in real materials (Fig. 1).

The predictive ability of the model can be assessed by comparing strength predictions (using the open-cell foam model) to measurements of tensile and compressive strength available in the literature for trabecular bone. The predictions are compared to the data of Keaveny *et al.* (1994, Fig. 1), who report a ratio of tensile to compressive strength of 0.73 ± 0.47 at an apparent density of 0.6 g/cm^3 (relative density of 0.33, assuming a bone tissue density of 1.8 g/cm^3 [Galante *et al.*, 1970]; the variability in the strength ratio was calculated by adding the coefficients of variation for the tensile and compressive strngth measurements, defined as the standard deviation divided by the mean). Specimens in this experiment were prepared such that the direction of the primary trabecular orientation was closely aligned with the direction of loading. Therefore, $\theta = 60^\circ$ is used in the model to represent, on average, the relatively steep angle at which the oblique trabeculae lie relative to the horizontal (Fig. 9). A value of $h/l = 0.5$ is also used; this combination of h/l and θ results in a strength anisotropy ratio (ratio of longitudinal to transverse strength) of approximately 8 from the model, consistent with anisotropy ratios reported for highly oriented trabecular bone (Williams and Lewis, 1982). It is assumed that the cell walls are made of cortical bone, which has a tensile strength of 140 MPa and a compressive strength of 209 MPa (Burstein *et al.*, 1976). Unfortunately, the exact relationship between the strut aspect ratio t/l and relative density for this trabecular bone is unknown. However, for strut aspect ratios ranging from 0.1 to 0.5, which are reasonable estimates for this trabecular bone, our model predicts levels of strength asymmetry that are consistent with the experimental results. The open-cell foam model predicts a ratio of tensile to compressive strength of 0.83 at a strut aspect ratio of 0.3, which agrees reasonably well

with the reported value of 0.73 ± 0.47, particularly given the large amount of scatter present in the strength-density relationship for this trabecular bone ($r^2 = 0.66$, Fig. 1a) and the assumptions made regarding cell geometry and cell wall material properties. Neither the compressive nor the tensile strength of trabecular tissue have been directly measured; the ratio of compressive to tensile strength may in fact be higher than the value assumed here. The experimental trabecular bone data also show that the tensile and compressive strengths become equal at an apparent density of approximately 0.5 g/cm^3 (relative density of 0.28). The theoretical model predicts that the tensile and compressive strengths do not become equal until the strut aspect ratio becomes vanishingly small. A probable explanation for this discrepancy is that trabeculae begin to fail by buckling in compression at low relative densities, a phenomenon that is not accounted for in the the model. However, the model does predict levels of strength asymmetry that are consistent with experimental dat for apparent densities above about 0.55 g/cm^2, and also correctly predicts that the strength asymmetry increases with relative density.

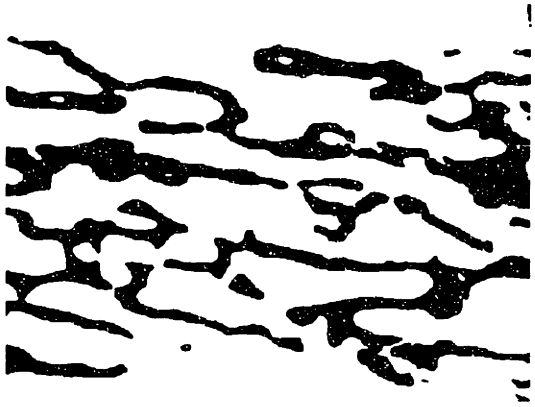

Figure 9: Section through a typical bovine tibial trabecular bone specimen (bone is black; Keaveny *et al.*, 1994). Specimens were harvested such that the primary trabecular orientation was aligned relative to the direction of loading (horizontal).

Experimental data are also available for the uniaxial strengths of rigid polyurethane foams, another material that exhibits density-dependent differences in tensile and

compressive strengths (Fig. 1, Triantafillou *et al.*, 1989). Unfortunately, a lack of experimental data for the tensile strength of the cell wall material prevents us from making a direct quantitative comparison between the model predictions and experiment. Assuming that the tensile strength of the cell wall material is less than the compressive strength and that the cell wall material has ductility in tension, then the model can qualitatively explain the increase in the strength differential with relative density that is observed experimentally in these foams. Although these comparisons for trabecular bone and rigid polyurethane foams would benefit from improved data for cell wall material properties, the comparisons nevertheless support the conclusion that combined axial and bending forces acting on obliquely oriented struts gives rise to strength asymmetry in real materials.

Although simple unit cell models are useful for characterizing the mechanisms responsible for observed cellular material behavior, these models are limited because they do not account for the natural variability present in real materials. In fact, finite element analyses have revealed that honeycombs with non-periodic structure are typically 30-35% weaker than regular honeycombs of the same density, because a small number of cell walls in non-periodic structures experience higher strains than the cell walls in periodic structures (Silva and Gibson, 1996). Although this finding is limited to two-dimensional materials, it suggests that idealized unit cell foam models may overestimate the absolute strength of real materials with inherent variability. The larger strains that occur in materials with microstructural variability are likely to occur to the same extent in tension and compression, however, and therefore the predictions for ratios of tensile to compressive strength should not be significantly limited by the assumption of an idealized unit cell geometry. Even so, predictions of absolute strength values based on unit cell models with idealized geometries should be interpreted with care.

The three-dimensional unit cell geometry used in this study is most representative of an open-cell foam, and therefore may not be the most appropriate model for explaining strength asymmetry behavior in closed-cell foams. However, the open-cell model may still

provide insight into the behavior of closed-cell foams. In closed-cell materials, where plates rather than rods are the primary structures, it is feasible that a combination of axial and bending forces in obliquely oriented plates results in density-dependent strength asymmetry. This idea is supported by the fact that the model was able to explain the uniaxial strength behavior of rigid polyurethane foams, which are closed-cell materials. Since membranes in closed-cell foams tend to carry higher axial loads than cell edges, the strength differential effect may be even more pronounced in closed-cell than in open-cell foams. The analysis presented here is also limited to honeycombs and foams where the direction of loading is aligned with the principal material directions (X_1 and X_2 directions, Fig. 2). In practice, materials can also be subjected to uniaxial loads that are aligned obliquely relative to the unit cell orientation, and also to more complex multiaxial loading conditions. To address this issue, in the following chapter these models are used to analyze the strength behavior of cellular materials under more complex loading conditions. Given that the model explains the mechanisms responsible for uniaxial strength behavior which were previously not well-understood, the insights gained from the uniaxial analyses presented here should allow for the development of improved multiaxial failure criteria for cellular materials.

3.7 References

Burstein A. H., Reilly D. T., and Martens M. (1976) Aging of bone tissue: mechanical properties. *J Bone Joint Surg* **58-A**, 82-86.

Galante J., Rostoker W., and Ray R. D. (1970) Physical properties of trabecular bone. *Calcif Tissue Res* **5**, 236-246.

Gibson L. and Ashby M. (1988) *Cellular Solids: Structure & Properties*, Pergamon Press, Oxford.

Kaplan S., Hayes W., Stone J., and Beaupre G. (1985) Tensile strength of bovine trabecular bone. *J Biomech* **18**, 723-727.

Keaveny T. M., Wachtel E. F., Ford C. M., and Hayes W. C. (1994) Differences between the tensile and compressive strengths of bovine tibial trabecular bone depend on modulus. *J Biomech* **27**, 1137-1146.

Silva M. and Gibson L. (1996) The effects of non-periodic microstructure and defects on the compressive strength of two-dimensional cellular solids. *Int J Mech Sci* , in press.

Stone J. L., Beaupre G. S., and Hayes W. C. (1983) Multiaxial strength characteristics of trabecular bone. *J Biomech* **16**, 743-752.

Triantafillou T. C., Zhang J., Shercliff T. L., Gibson L. J., and Ashby M. F. (1989) Failure surfaces for cellular materials under multiaxial loads--II. Comparison of models with experiment. *Int J Mech Sci* **31**, 665-678.

Warren W. and Kraynik A. (1988) The linear elastic properties of open-cell foams. *Journal of Applied Mechanics* **55**, 341-346.

Williams J. and Lewis J. (1982) Properties and an anisotropic model of cancellous bone from the proximal tibial epiphysis. *J Biomech Eng* **104**, 50-56.

Chapter 4

Multiaxial Failure Properties of Cellular Materials: An Analytical Model

4.1 Introduction

The service loads experienced by natural and engineering cellular solids can cause complex multiaxial states of stress to develop within the material. For example, foams used in protective equipment are subjected to three-dimensional states of stress during impact, and natural cellular materials such as trabecular bone undergo complex multiaxial stresses during normal and traumatic activities. An understanding of how cellular materials fail under multiaxial stresses is directly applicable to the design of materials for packaging and protective devices, and for failure prediction in natural and engineered structures.

Analysis of the microstructural mechanisms of deformation in cellular materials under load can lead to an understanding of how the macroscopically-observed failure properties of a material relate to features such as cell geometry, relative density and cell wall material properties. This unit-cell approach has been used previously to describe the multiaxial failure behavior of two-dimensional honeycombs and three-dimensional porous foams (Gibson *et al.*, 1989). Despite its success in predicting the failure behavior of a number of materials, this model does not always accurately predict the failure behavior of cellular materials that have greater compressive than tensile strength, and whose strength differential increases with increasing relative density. In particular, failure of materials (such as trabecular bone and rigid polyurethane foams) that fail by the same mechanism in tension and compression (yielding or microcracking), and whose strength asymmetry arises from a difference between the tensile and compressive strengths of the cell wall material, is not well-described by previous theory (Triantafillou *et al.*, 1989; Borchers,

1991). In Chapter 3, a tetrahedral unit cell model was used to demonstrate that density-dependent, compression-strong strength asymmetry arises in cellular materials when two conditions are met: the solid cell wall material is stronger in compression than tension, and obliquely oriented members are loaded simultaneously by axial forces and bending moments. In this chapter, these mechanisms are incorporated into an analysis of the behavior of cellular materials under more complex states of stress. First, the failure behavior of a simple, two-dimensional honeycomb is analyzed under a biaxial state of stress, and then the three dimensional tetrahedral unit cell from the previous chapter is used to derive yield surfaces for foams under a general, three-dimensional state of stress. The chapter is then completed by comparing the failure envelopes derived analytically using the microstructural model to the Tsai-Wu failure criterion developed experimentally in Chapter 2.

4.2 Analysis: Honeycomb

First, the failure surface for hexagonal honeycombs under a general biaxial state of stress are derived, incorporating a difference in the tensile and compressive yield strengths of the cell wall material, using the method of Gibson and Ashby (1988). The analysis is confined to cases where the solid cell wall material has ductility in both tension and compression, suggesting that failure is either by yielding or microcracking. This analysis closely parallels that presented in Chapter 3, but allows for stresses in both the X_1 and X_2 directions (Fig. 1).

The unit cell of a regular, isotropic honeycomb is shown in Fig. 1a; anisotropy is introduced by changing either h/l or θ (Fig. 1b). The relative density of the honeycomb is given by

$$\frac{\rho^*}{\rho_s} = \frac{(2+h/l)}{2\cos\theta(h/l+\sin\theta)}\frac{t}{l} \tag{1}$$

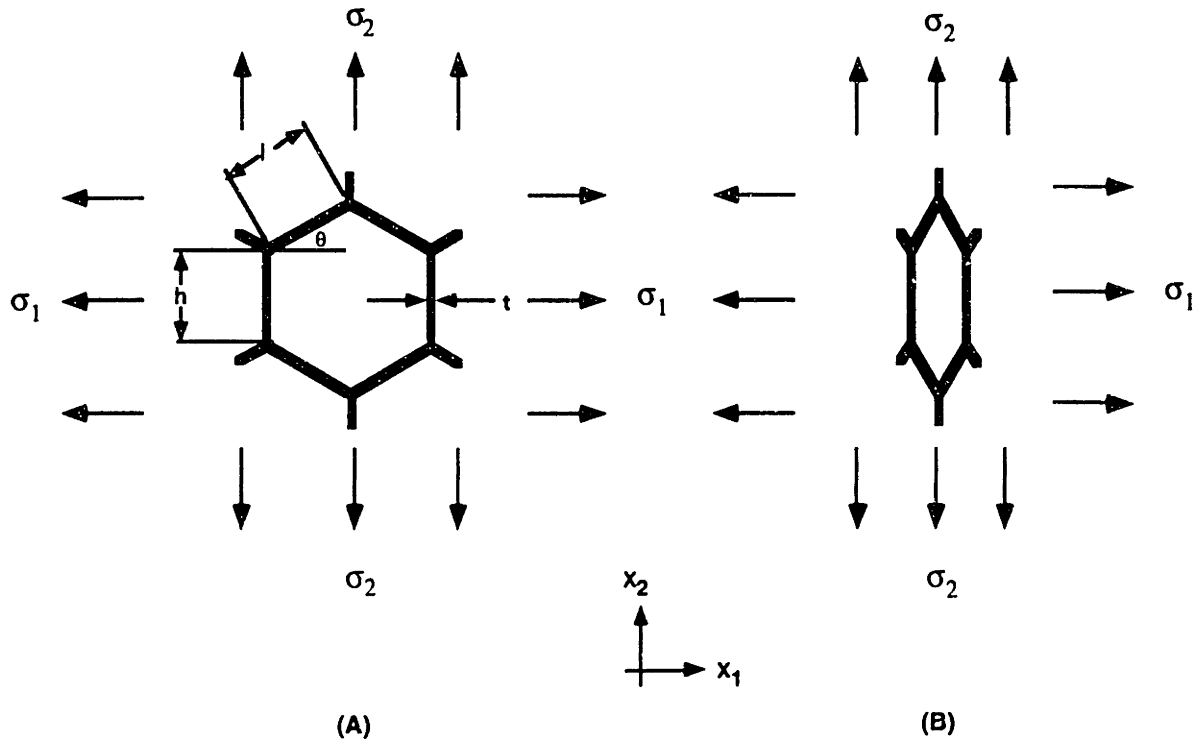

Figure 1: Unit cells of hexagonal honeycombs used to model failure under biaxial loads. The cell shape is described by parameters h/l and θ; the relative density is proportional to the aspect ratio of the cell walls t/l. (A) Regular, isotropic unit cell with h/l = 1 and θ = 30°. (B) Anisotropic unit cell. Anisotropy is introduced when either $h/l \neq 1$ or $\theta \neq 30°$.

The application of remote uniaxial stresses σ_1 and σ_2 produces a bending moment M and an axial stress σ_a on the inclined member of the unit cell (Fig. 2). The maximum bending moment and the axial stress in the cell wall are given by

$$M = \frac{(P_1 \sin\theta - P_2 \cos\theta)l}{2} \tag{2}$$

$$\sigma_a = \frac{P_1 \cos\theta + P_2 \sin\theta}{bt} \tag{3}$$

where P_1 and P_2 are the loads applied to the oblique strut in the X_1 and X_2 directions, respectively. These loads on the oblique strut relate to the remotely applied stresses σ_1 and σ_2 through the following equations:

$$P_1 = \sigma_1(h + l\sin\theta)b \tag{4}$$

$$P_2 = \sigma_2(l\cos\theta)b. \tag{5}$$

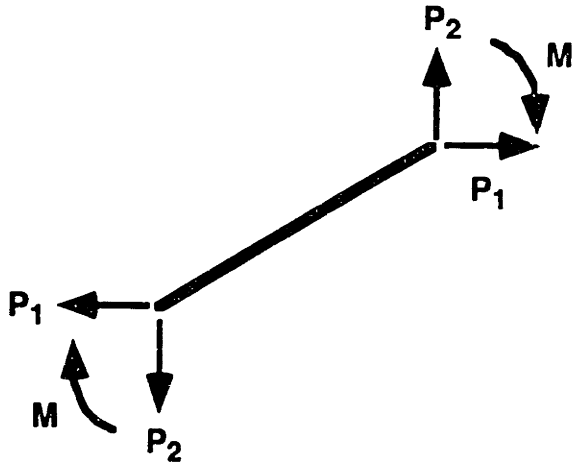

Figure 2: The application of remote stresses in the vertical (X_2) and horizontal (X_1) directions produces bending moments M and axial forces P_1 and P_2 on the inclined members of the honeycomb unit cell.

Failure of the honeycomb occurs when the cell wall has yielded across its entire section (Fig. 3). The depth of the neutral axis c is given by

$$c = \frac{t(\sigma'_{y1} + \sigma_a)}{\sigma'_{y1} + \sigma'_{y2}} \tag{6}$$

where σ_{ys}^{c} and σ_{ys}^{t} are the compressive and tensile yield strengths of the cell wall material, respectively (see Chapter 3). The fully plastic moment is then given by the force, F, times the moment arm, t/2:

$$M_p = \left(\sigma_{ys}^{t} - \sigma_a\right)\frac{bct}{2} \tag{7}$$

or

$$M_p = \frac{bt^2}{2}\left(\frac{\sigma_{ys}^{t}\sigma_{ys}^{c} + \left(\sigma_{ys}^{t} - \sigma_{ys}^{c}\right)\sigma_a - \sigma_a^2}{\sigma_{ys}^{t} + \sigma_{ys}^{c}}\right) \tag{8}$$

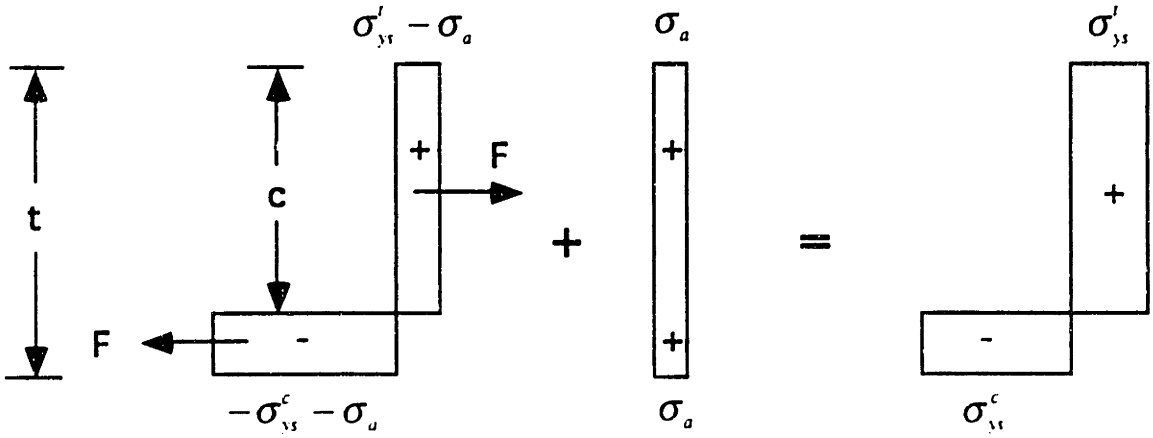

Figure 3: The bending, axial and total stress distributions across the section of an oblique strut that has failed as a result of plastic hinge formation. The depth of the neutral axis *c* is found by equating forces above and below the neutral axis.

The applied moment M (Eqn. 2, which can be positive or negative depending on the signs and relative magnitudes of σ_1 and σ_2) is equated with the plastic moment M_p (Eqn. 8), resulting in the equation governing the failure surface for the honeycomb under a biaxial stress state:

$$\pm\left(\frac{\sigma_1(h/l+\sin\theta)\sin\theta-\sigma_2\cos^2\theta}{(t/l)^2}\right)=$$

$$\frac{1}{\sigma_{ys}^c+\sigma_{ys}^t}\left(\sigma_{ys}^t\sigma_{ys}^c+\frac{\sigma_{ys}^t-\sigma_{ys}^c}{t}\left(\sigma_1(h+l\sin\theta)\cos\theta+\sigma_2 l\cos\theta\sin\theta\right)\right. \tag{9}$$
$$\left.-\frac{1}{t^2}\left(\sigma_1(h+l\sin\theta)\cos\theta+\sigma_2 l\cos\theta\sin\theta\right)^2\right)$$

4.3 Results: Honeycomb

The solution to Equation 9 is two intersecting ellipses that define the failure surface for plastic yielding of the honeycomb under biaxial loading. To demonstrate the effects of anisotropy on the shape of the failure envelope, the envelope was calculated for both an isotropic honeycomb($h/l = 1$, $\theta = 30°$) and for an anisotropic honeycomb ($h/l = 2$, $\theta = 60°$, Fig. 4). These calculations were performed assuming that the compressive strength of the cell wall material was 40% higher than the tensile strength (R = $\sigma_{ys}^c/\sigma_{ys}^t = 1.4$), and assuming $t/l = 0.2$. An increase in the anisotropy of the honeycomb corresponded to a distortion of the isotropic yield envelope in the ratios of the uniaxial yield strengths.

To demonstrate the effect of strength asymmetry in the cell wall material, the case where the compressive strength of the cell wall material was 40% higher than the tensile strength (R = $\sigma_{ys}^c/\sigma_{ys}^t = 1.4$) was plotted with the case where the tensile and compressive strengths of the cell wall were equal (Fig. 5). The difference in cell wall strength ratio had the largest impact in the tension-tension quadrant, since the extreme point on the failure envelope in this quadrant corresponds to pure axial tension in the cell walls. In contrast, the change in cell wall strength ratio had very little effect on the failure envelope in the compression-compression quadrant.

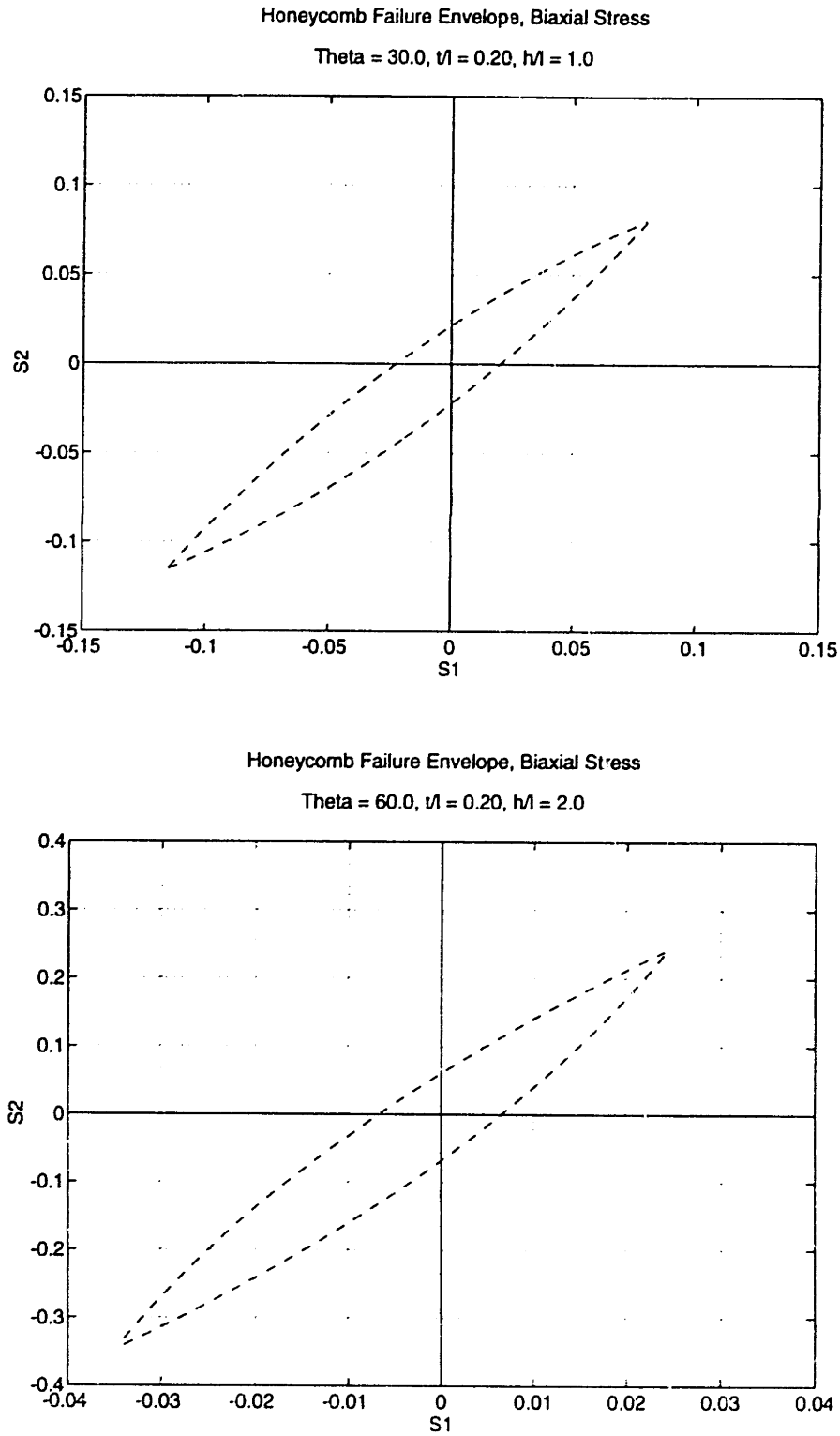

Figure 4: Yield surface for isotropic (top) and anisotropic (bottom) honeycombs under biaxial loading. S1 and S2 are the stresses in the X_1 and X_2-directions, respectively, normalized by the compressive strength of the cell wall material σ^c_{ys}. Surfaces are plotted assuming that the compressive strength of the cell wall material is 40% higher than the compressive strength.

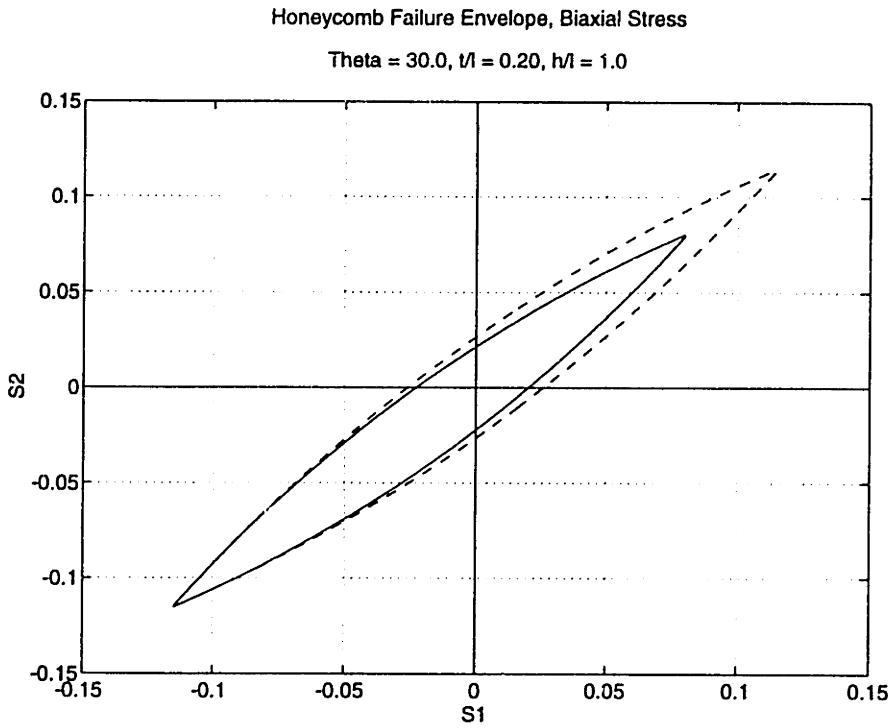

Figure 5: Yield surface for isotropic honeycomb with ratio of compressive to tensile strength of the cell wall material R = 1.4 (solid line), compared with yield surface assuming no strength asymmetry in the cell wall material (R = 1.0, dashed line).

4.4 Analysis: Foams

The mechanisms of deformation and failure in foams are similar to those in honeycombs. As in the previous chapter, it is assumed that a microstructural element comprised of a single vertical strut with three oblique struts joining at equal angles captures the essential features of the mechanical behavior (Fig. 6). Each strut has a square cross section of width t. A tetrahedral element, with four struts of equal length meeting at equal angles, is used to model more isotropic foams; anisotropy is increased by changing the angle θ. The behavior of this microstructural element is now analyzed under a three-dimensional state of stress using dimensional arguments. The case where the principal stresses σ_1, σ_2 and σ_3 are aligned with the principal material directions is analyzed here;

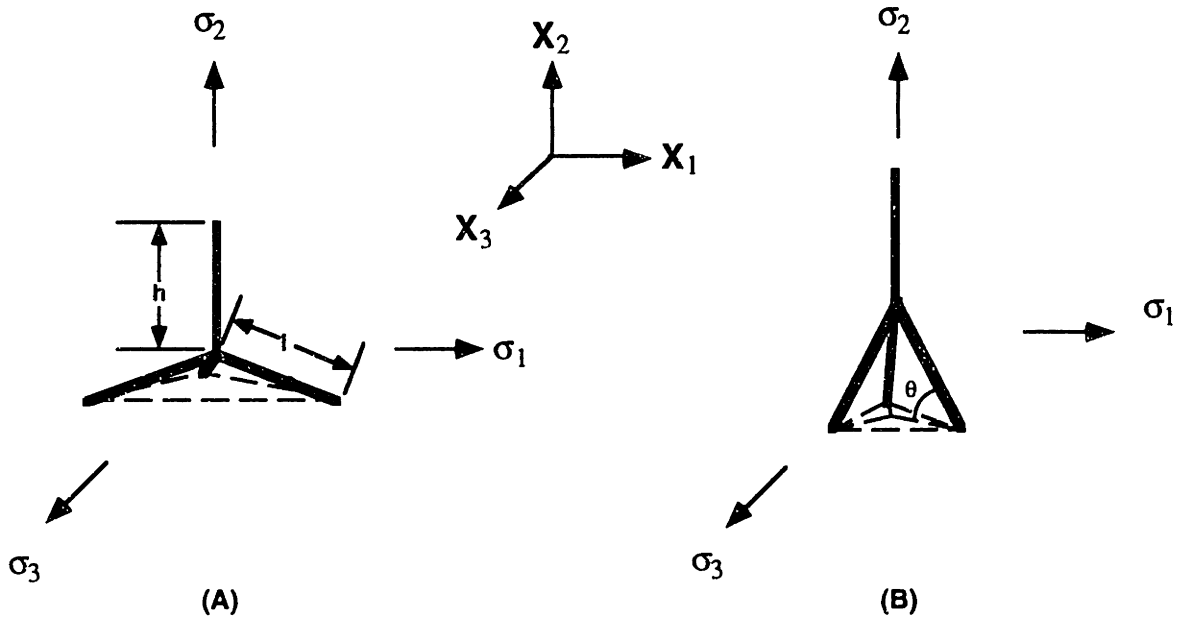

Figure 6: Microstructural elements used to study multiaxial failure in foams. Each strut has a square cross section with width *t*. (A) Four struts of equal length meeting at equal tetrahedral angles. (B) Struts of unequal length, or at angles other than the tetrahedral angle, model more anisotropic foams.

the considerably more complex case where principal stresses are not aligned with the principal material directions is treated in the Appendix.

To determine the failure surface, the applied moment in each oblique strut (due to the application of the remote stresses σ_1, σ_2 and σ_3) is equated with the moment required to form a plastic hinge in that strut. By contrast to the honeycomb analysis (where the moments applied to each oblique strut were equal), here the applied moment can be different in each strut and therefore each oblique strut must be analyzed separately. The applied moment and axial stress in strut A (Fig. 8B) are given by

$$M_A = \left(P_3 \sin\theta - \frac{P_2}{3}\cos\theta \right)\frac{l}{2} \tag{10}$$

$$\sigma_{a.A} = \left(P_3 \cos\theta + \frac{P_2}{3}\sin\theta \right)\frac{1}{t^2} \tag{11}$$

where P_1, P_2, and P_3 are the local forces applied to the microstructural element in the X_1, X_2, and X_3 directions (Fig. 7). The applied moments and axial stresses are equal in struts B and C (Fig. 7C, D); they are given by

$$M_{B,C} = \frac{l}{2}\left[\left(P_1 \sin\phi - \frac{P_2}{3}\cos\phi\right)^2\left(1-\frac{1}{4}\cos^2\theta\right)+\left(\frac{P_3}{2}\sin\psi - \frac{P_2}{3}\cos\psi\right)^2\left(1-\frac{3}{4}\cos^2\theta\right)\right]^{\frac{1}{2}}$$

$$\sigma_{a,B} = \sigma_{a,C} = \frac{1}{t^2}\left(\frac{\sqrt{3}}{2}P_1\cos\phi + \frac{P_2}{3}\sin\theta + \frac{P_3}{4}\cos\psi\right) \qquad (12)$$

where $\tan\phi = \tan\theta\sec 30^\circ$, $\tan\psi = \tan\theta\csc 30^\circ$ (Fig. 7B). In the case where the principal stresses are aligned with the principal material directions, the vertical strut is subjected to only an axial force with no bending moment; therefore, the deformation of the vertical strut is negligible with respect to the oblique struts, and it need not be included in the analysis. It is assumed that for a single microstructural element, the remote stress σ_2 acts over an area proportional to $(l\cos\theta)^2$ (the product of the characteristic dimensions of the microstructural element in the X_1- and X_3-directions), and therefore $P_2 = k_2\sigma_2 l^2\cos^2\theta$. Similarly, it is assumed that the remote stresses σ_1 and σ_3 each act over an area proportional to $l\cos\theta(l\sin\theta + h)$ (the product of the characteristic dimensions of the microstructural element in the X_2 and X_3 directions), and therefore $P_1 = k_1\sigma_1 l\cos\theta(l\sin\theta + h)$ and $P_3 = k_3\sigma_3 l\cos\theta(l\sin\theta + h)$. k_1, k_2 and k_3 are unknown constants of proportionality related to the spatial arrangement of unit cells within the material. The moment required to form a plastic hinge in each strut is given by

$$M_{p,i} = \frac{t^3}{2}\left(\frac{\sigma_{ys}^t\sigma_{ys}^c + \left(\sigma_{ys}^t - \sigma_{ys}^c\right)\sigma_{a,i} - \sigma_{a,i}^2}{\sigma_{ys}^t + \sigma_{ys}^c}\right) \qquad (13)$$

where i = 1,2,3. Failure of the material is defined when the applied moment in any strut equals the fully plastic moment for that strut. Therefore, failure occurs whenever one of the following conditions is met:

Condition 1 (Applied moment = plastic moment in strut A):

$$\left(k_1\sigma_3 rH\sin\theta-\frac{k_2}{3}\sigma_2 r^2\right)\frac{l}{2}= \tag{14}$$

$$\frac{t^3}{2\left(\sigma_{ys}^c+\sigma_{ys}^t\right)}\left(\sigma_{ys}^t-\frac{1}{t^2}\left(k_3\sigma_3 rH\cos\theta+\frac{k_2}{3}\sigma_2 r^2\sin\theta\right)\right)\left(\sigma_{ys}^t+\frac{1}{t^2}\left(k_3\sigma_3 rH\cos\theta+\frac{k_2}{3}\sigma_2 r^2\sin\theta\right)\right)$$

Condition 2 (Applied moment = plastic moment in struts B or C):

$$\begin{aligned}&\frac{l}{2}\left[\left(k_1\sigma_1 rH\sin\phi-\frac{k_2}{3}\sigma_2 r^2\cos\phi\right)^2\left(1-\frac{1}{4}\cos^2\theta\right)\right.\\&\qquad\left.+\left(\frac{k_3}{2}\sigma_3 rH\sin\psi-\frac{k_2}{3}\sigma_2 r^2\cos\psi\right)\left(1-\frac{3}{4}\cos^2\theta\right)\right]^{\frac{1}{2}}\\&=\frac{t^3}{2}\left(\sigma_{ys}^t-\frac{1}{t^2}\left(\frac{\sqrt{3}}{2}k_1\sigma_1 rH\cos\phi+\frac{k_2}{3}\sigma_2 r^2\sin\theta+\frac{k_3}{4}\sigma_3 rH\cos\psi\right)\right)\\&\qquad\left(\sigma_{ys}^t+\frac{1}{t^2}\left(\frac{\sqrt{3}}{2}k_1\sigma_1 rH\cos\phi+\frac{k_2}{3}\sigma_2 r^2\sin\theta+\frac{k_3}{4}\sigma_3 rH\cos\psi\right)\right)\end{aligned} \tag{15}$$

where $r=l\cos\theta$ and $H=h+l\sin\theta$.

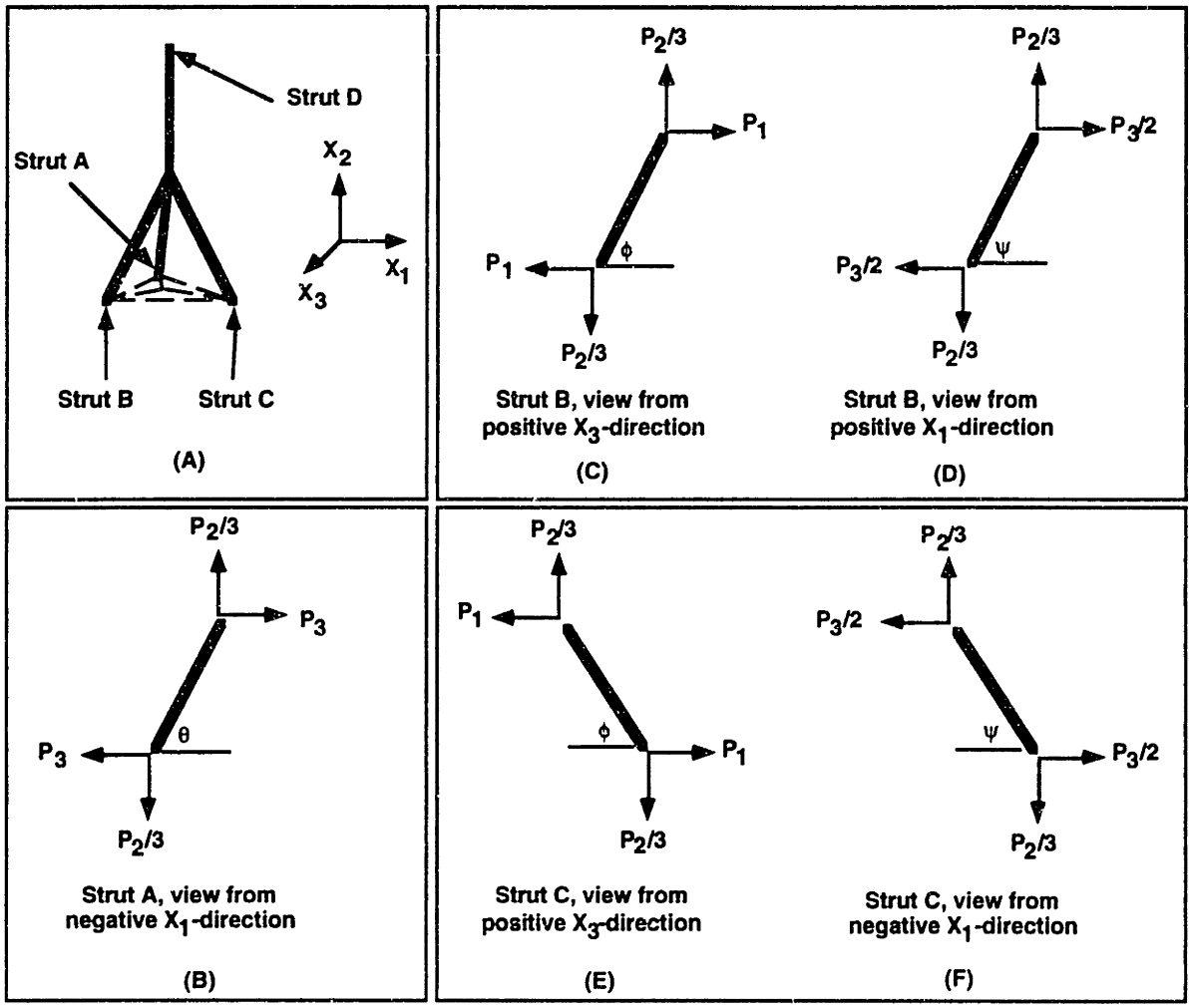

Figure 7: Detail of forces acting locally on each strut of the microstructural element due to the application of normal stresses in the X_1, X_2 and X_3-directions. (A) Struts A, B and C experience both bending moments and axial forces as a result of the remotely applied stresses. Strut D experiences only axial loading, and therefore is not included in the analysis. (B - F) Detail of local forces acting on struts A, B and C.

4.5 Results: Foam

The failure surface was plotted for two different states of stress: triaxial loading with $\sigma_1 = \sigma_3$ (Fig. 8), and biaxial loading with $\sigma_1 = 0$ (Fig. 9). To demonstrate the effects of anisotropy, the failure surface for each state of stress was plotted for both the tetrahedral element ($h/l = 1$, $\theta = 19°$) and for a more anisotropic element ($h/l = 2$, $\theta = 45°$). Each failure surface was calculated assuming that the compressive strength of the cell wall material was 40% higher than the tensile strength ($R = \sigma^c_{ys}/\sigma^t_{ys} = 1.4$), and with a strut aspect ratio t/l of 0.2. To determine reasonable values for the constants of proportionality k_1, k_2 and k_3, it was assumed that the microstructural element occupies a volume equal to that of a circular cylinder, with height equal to the height of the microstructural element H and radius equal to half of the width of the element (r). Therefore, k_1, k_2 and k_3 were set equal to 2, π, and 2, respectively. The choice of a circular cylinder to represent the unit cell volume results in a constant of proportionality between the strut aspect ratio t/l and the relative density (or volume fraction of solid) ranging from about 1.0 (for $\theta = 19°$) to 2.7 (for $\theta = 60°$), consistent with regular, space-filling structures such as tetrakaidecahedra and pentagonal dodecahedra (Gibson and Ashby, 1988).

For the triaxial stress state, the failure surface had an ellipsoidal shape, elongated along the line representing hydrostatic stress (transverse stress = axial stress). When anisotropy was increased, this elongated ellipsoid was distorted in the ratios of the uniaxial strengths (Fig. 8). For the biaxial stress state with $\sigma_1 = 0$, the failure envelope took a shape resembling a parallelogram with vertical sides curved outward (Fig. 9). The sharp corners in the failure envelope occur at stress states where the equations defining failure of individual struts (Eqns. 14, 15) intersect. As in the case of triaxial stress, an increase in anisotropy resulted in a distortion of the failure envelope in the ratio of the uniaxial strengths.

To assess the effects of strength asymmetry in the cell wall material, failure envelopes were plotted with R = 1.4 and R = 1.0, for both the triaxial and biaxial stress states (Fig. 10). For the triaxial stress state, the decrease in tensile strength relative to compressive strength of the cell wall material had a relatively large effect on the failure envelope in the triaxial tension quadrant, and a much smaller effect in the triaxial compression quadrant. For the biaxial stress state, the decrease in tensile relative to compressive strength of the cell wall material resulted in contraction of the failure envelope in all quadrants.

4.6 Comparison of Analytical and Tsai-Wu Failure Envelopes

The analytical failure criterion developed here and the Tsai-Wu failure criterion developed experimentally in Chapter 2 were compared for both axisymmetric and biaxial states of stress. Yield surfaces based on the von Mises failure criterion are also included in the comparison, since the von Mises criterion has been used by previous investigators to model trabecular bone behavior (Lotz *et al.*, 1991b; Lotz *et al.*, 1991a) Since accurate predictions of strength magnitudes from the analytical model are not possible without accurate measurements of the strength properties of trabecular tissue, the calculated failure stresses (from both the analytical and Tsai-Wu criteria) were normalized by the uniaxial compressive strengths of the cellular material in the principal material directions (i.e., all σ_1 values were normalized by the uniaxial compressive strength in the 1-direction, etc.). Input geometric parameters for the analytical model ($\theta = 60°$, $h/l = 0.5$) were chosen such that the predicted strength anisotropy ratio (i.e. ratio of axial to transverse strengths) was consistent with the anisotropy ratio predicted by the Tsai-Wu criterion. The predicted analytical failure envelope (for a strut aspect ratio of 0.4) and the Tsai-Wu failure envelope for an apparent density of 0.4 (relative density of 0.2) are plotted together in Fig. 11 for triaxial (axisymmetric) and biaxial states of stress. For the axisymmetric case, the failure

envelopes both have elongated shapes, and are oriented in a similar manner relative to the axial and transverse stress axes. In the triaxial compression quadrant, the analytical criterion predicts substantially higher stresses at failure for stress states approaching hydrostatic compression than the Tsai-Wu criterion. In the triaxial tension quadrant, and in the quadrants where the axial and transverse stresses are in opposite directions, the two criteria are qualitatively similar in shape. The von Mises yield surface is open in the triaxial tension and compression quadrants, because the criterion depends only on the deviatoric stress in the material and has no dependence on the mean stress. For the biaxial stress state, the analytical and Tsai-Wu failure envelopes cover similar areas in all quadrants, although the analytical criterion contains relatively sharp corners where the failure equations for individual struts in the microstructural element intersect. In the biaxial tension and compression quadrants, both the analytical and Tsai-Wu yield envelopes predict higher stresses at failure than the von Mises criterion, again because the von Mises criterion has no mean stress dependence.

4.7 Discussion

In the preceding chapter, it was demonstrated that compression-strong, density-dependent strength asymmetry can arise in a cellular material when two conditions are met: the cell wall material is stronger in compression than in tension, and members are loaded simultaneously by axial forces and bending moments. In this chapter these mechanisms were incorporated into the derivation of failure surfaces for cellular materials under a general, three-dimensional state of stress, which can be formulated for varying degrees of anisotropy. The derived failure surfaces are applicable to materials that are isotropic or nearly transversely isotropic, whose cell walls fail by yielding or microcracking (and therefore exhibit considerable ductility), and materials which fail by the same mechanisms in both tension and compression.

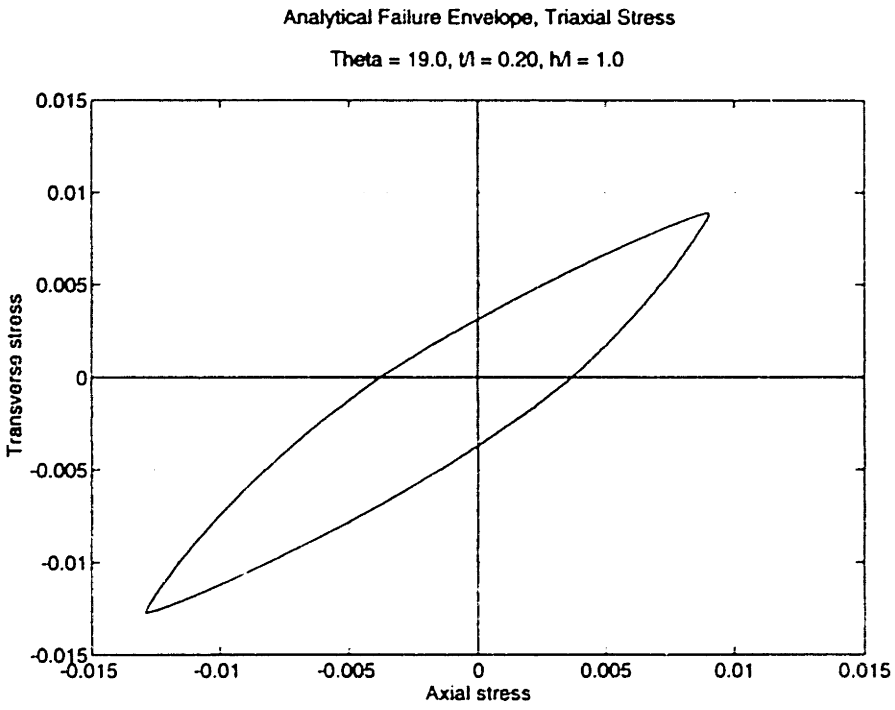

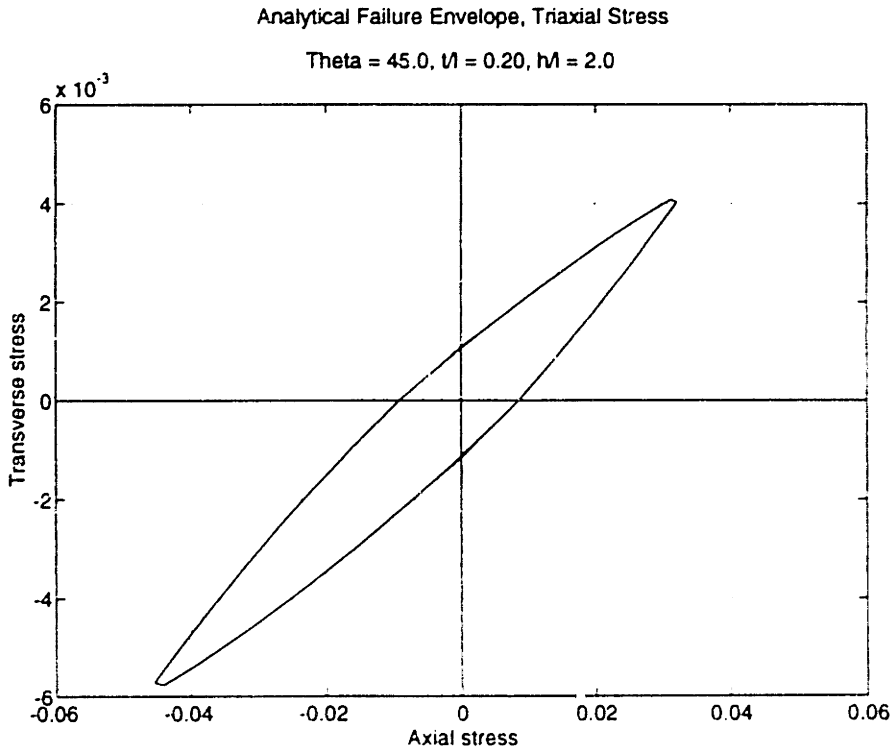

Figure 8: Sections through the plastic yield surface for an isotropic (top) and anisotropic (bottom) foam, under axisymmetric loading, assuming a ratio of compressive to tensile strength of the cell wall material of R = 1.4. Axial and transverse stresses are normalized by the compressive strength of the cell wall material σ^c_{ys}.

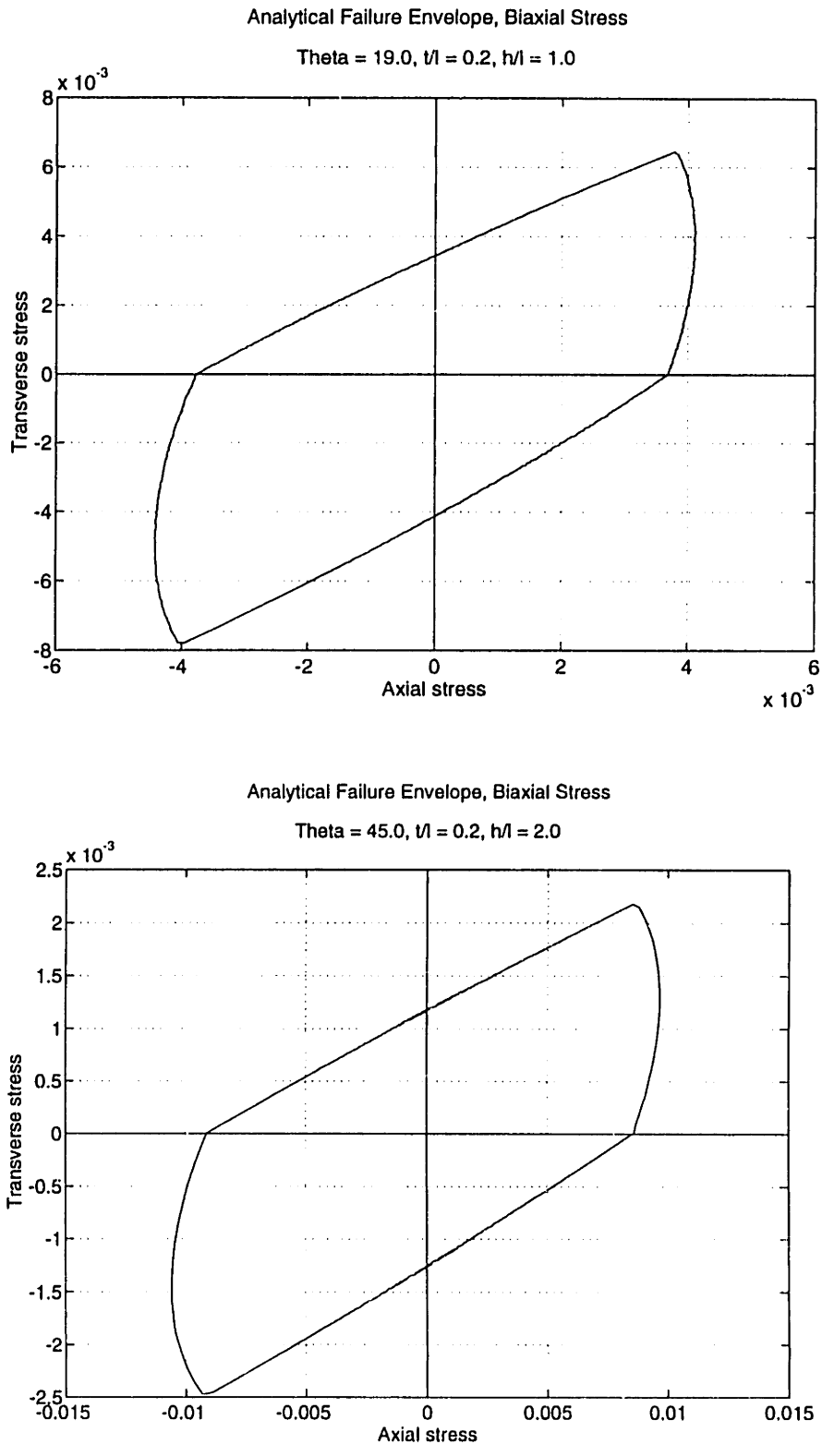

Figure 9: Sections through the plastic yield surface for a nearly isotropic (top) and an anisotropic (bottom) foam under biaxial loading with $\sigma_1 = 0$, assuming a ratio of compressive to tensile strength of the cell wall material of R = 1.4. Axial and transverse stresses are normalized by the compressive strength of the cell wall material σ_{ys}^{c}.

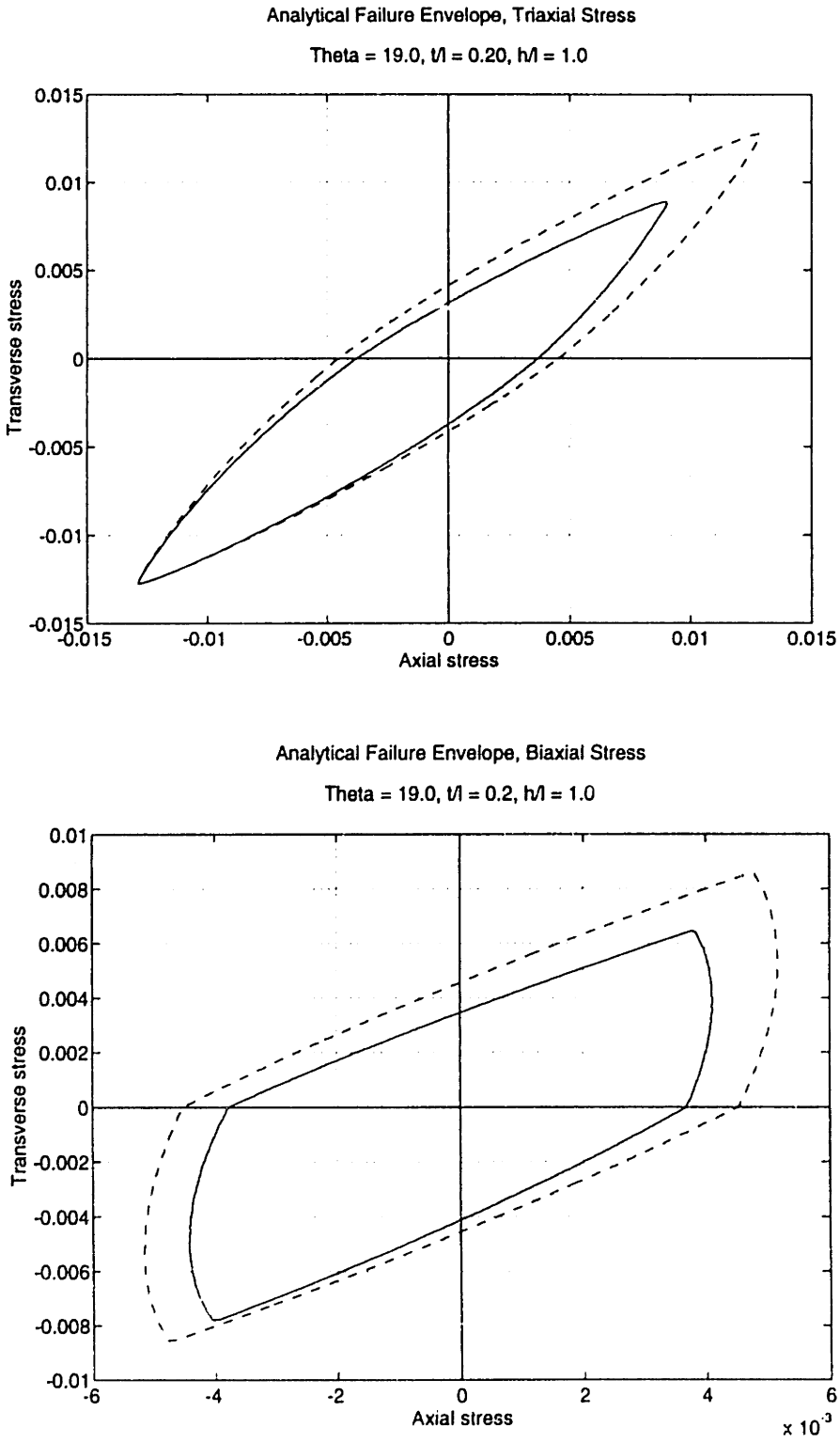

Figure 10: Section through the yield surface for a (nearly) isotropic foam under axisymmetric loading (top) and biaxial loading (bottom), with ratio of compressive to tensile strength of the cell wall material R = 1.4 (solid line), compared with yield surface assuming no strength asymmetry in the cell wall material (R = 1.0, dashed line).

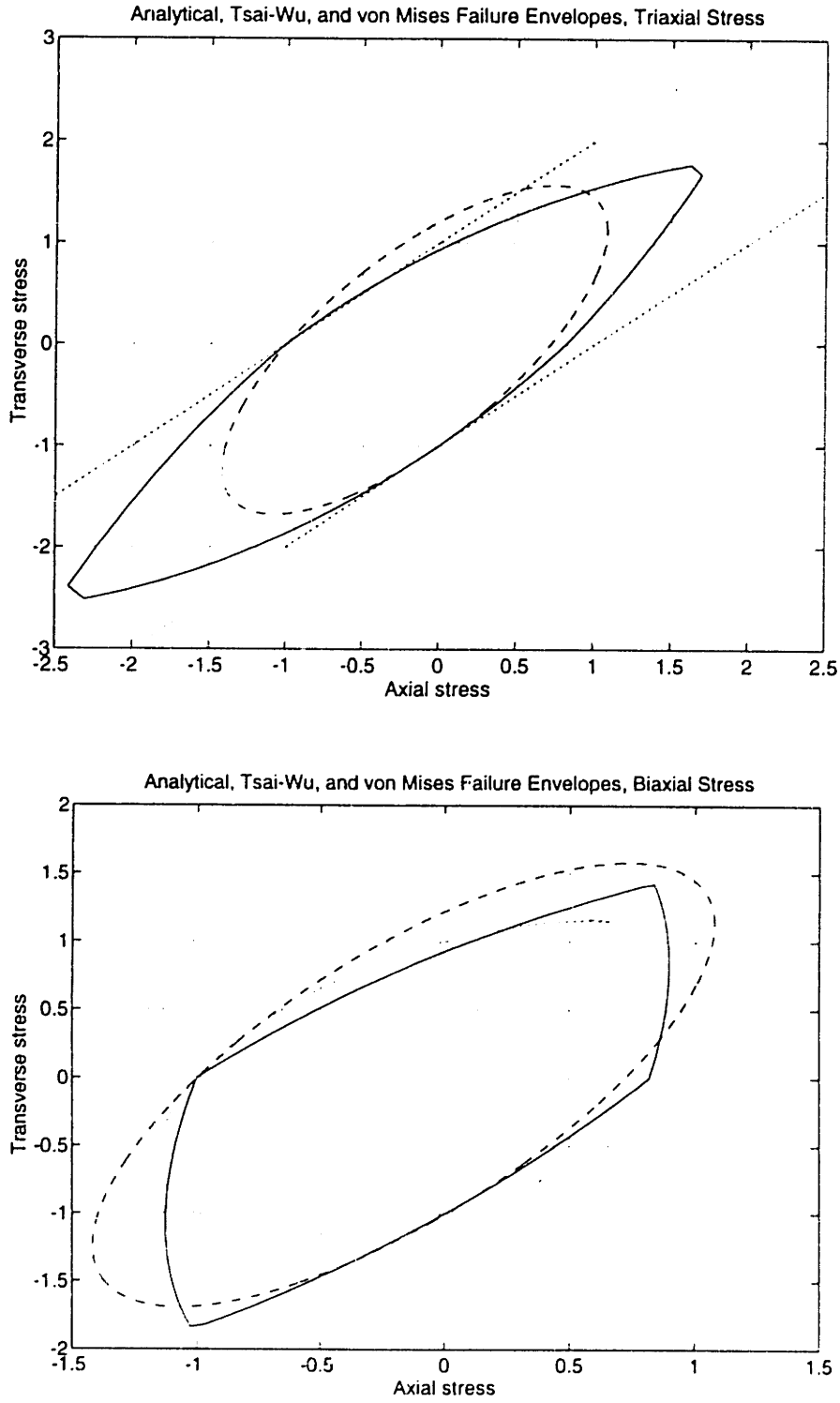

Figure 11: Yield surfaces for the analytical criterion developed here (solid line), the Tsai-Wu criterion developed in Chapter 2 (dashed line), and the von Mises yield condition (dotted line), for axisymmetric (top) and biaxial (bottom) states of stress.

The failure criterion developed in this chapter represents an extension of a previously developed failure criterion for foams, described by Gibson *et al.* (1989). In this analytical model, the yield surface for foams was derived using dimensional arguments: the analysis was based on a simple, cubic unit cell, and geometrical factors were lumped into an unknown constant of proportionality. Although the resulting failure criterion gave good predictions of the multiaxial strength behavior of several foams, it was less successful in predicting the strength behavior of materials that exhibit density-dependent differences in tensile and compressive strength (such as rigid polyurethane foams [Triantafillou *et al.*, 1989] and trabecular bone [Borchers, 1991]). A possible explanation for this is that the dimensional analysis did not allow for struts to be loaded simultaneously by axial forces and bending moments during uniaxial loading, a prerequisite for obtaining density-dependent differences in uniaxial strengths (Chapter 3). In addition, the previous model did not allow for differences between the tensile and compressive strengths of the cell wall material. The analysis techniques presented by Gibson *et al.* were applied to a microstructural element that allows simultaneous bending and axial forces in struts, and allows for strength asymmetry in the cell wall material, thereby effectively extended the previous failure criterion to allow for density-dependent differences in tensile and compressive strength of the cellular material. When the tensile and compressive strengths of the cell wall material are equal in the newly developed failure criterion, the shape of the failure envelope is similar to that of the previous model for the triaxial stress state (with the exception that the new criterion predicts somewhat lower strengths in hydrostatic tension and compression, Fig. 12). For the biaxial stress state, the shapes of the failure envelopes are similar except that the newly developed criterion predicts higher stresses at failure for ratios of transverse to axial stress greater than about 1.5. In addition, the new failure criterion is not perfectly isotropic (because of the geometry of the microstructural element) and therefore predicts uniaxial strengths in the transverse directions that are slightly lower than in the axial direction.

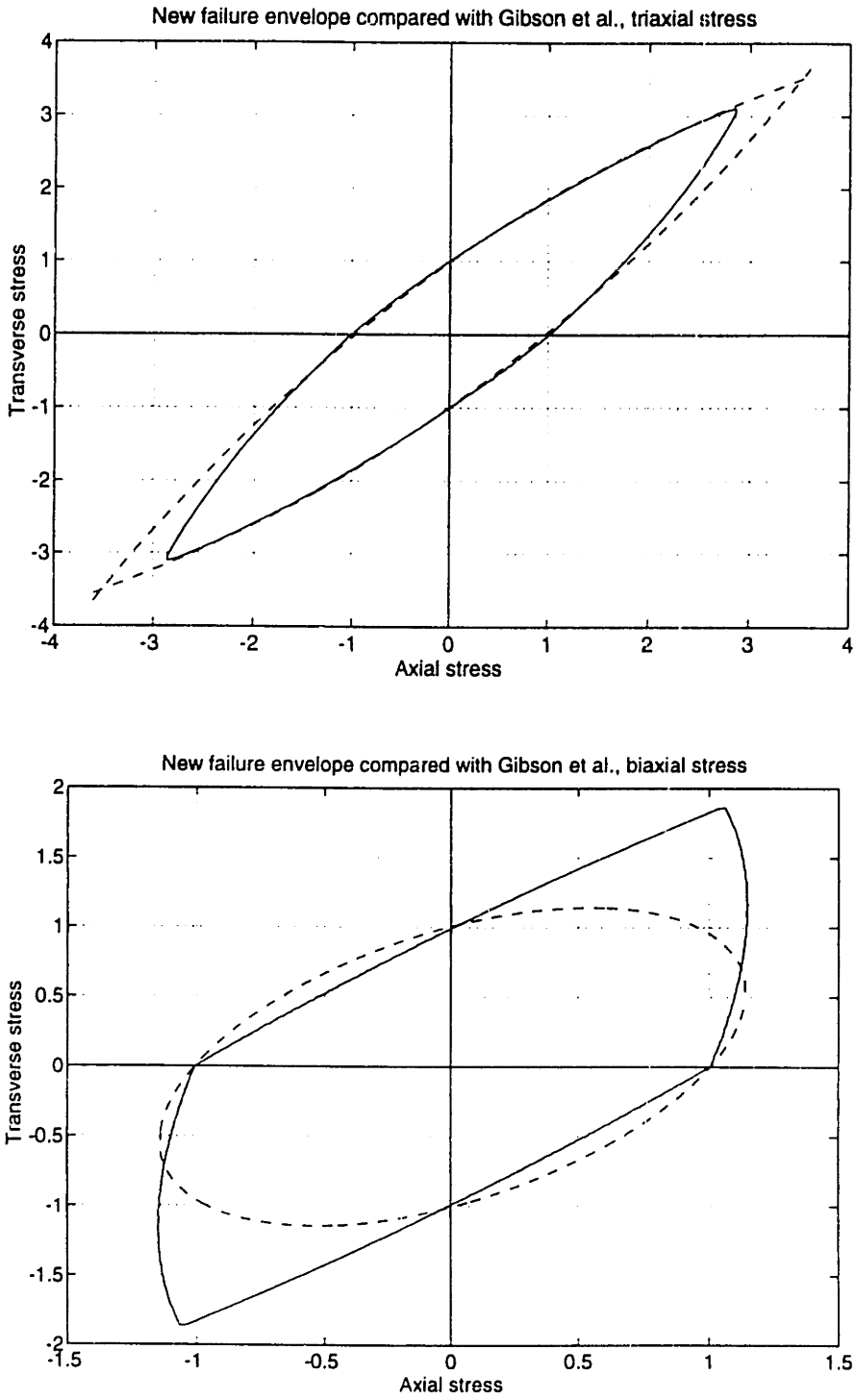

Figure 12: Comparison of failure surfaces derived here (isotropic case, assuming no strength asymmetry in the cell wall material, solid line) with failure surfaces derived by Gibson *et al.* (1989) for axisymmetric (top) and biaxial (bottom) loading. Axial and transverse stresses were normalized by the yield strength of the cellular material in the axial direction.

In general, there was good qualitative agreement between the predictions of the analytical failure criterion presented here, and the Tsai-Wu criterion developed in Chapter 2. However, for the triaxial state of stress, the analytical failure criterion predicted substantially higher stresses at failure for stress states approaching hydrostatic compression (Fig. 11). One possible explanation for this is that the new model does not account for trabecular buckling, which is a possibility whenever any of the principal stresses is compressive. For states of stress other than triaxial compression, however, the failure envelopes derived analytically and those derived experimentally are qualitatively similar. The good qualitative agreement of the shapes of the surfaces suggests that the failure mechanisms used to derive the analytical criterion (i.e., the combination of bending and axial forces acting on struts, coupled with differences in the tensile and compressive strengths of trabecular tissue) do in fact actively contribute to trabecular failure under multiaxial loads.

Due to the limited amount of experimental data available regarding multiaxial failure properties of trabecular bone, it was not possible to fully test the predictive ability of the analytical failure criterion developed here. However, a small amount of data was available from experiments performed by Borchers (1991), who performed triaxial experiments (axial load plus radial pressure) on bovine humeral trabecular bone. Ratios of radial to axial stress at failure from these experiments (for specimens which were approximately transversely isotropic) were compared to ratios predicted by the analytical model. The value of θ used as input to the model was chosen such that the predicted strength anisotropy ratio (i.e. ratio of axial to transverse uniaxial strengths) matched the strength anisotropy ratio measured in the experiments (defined as the ratio of axial strength to the average of the transverse strengths). Values of the geometric parameters h/l and t/l were chosen as 1.0 and 0.3, but these parameters do not significantly effect the predicted ratio of radial to axial stress at failure. Although the model consistently underestimated the stress ratio at failure,

the model predictions agree within about 20% with measured values for five of the nine specimens (Table 1). The underestimation of the stress ratio (caused by an overestimation of the axial stress at failure) may be due to the fact that trabeculae buckled during triaxial compression, a phenomenon not accounted for in the model. However, given the tremendous scatter present in the trabecular bone data (due in part to inhomogeneities in density and anisotropy within specimens), and given the technical difficulties involved in measuring multiaxial failure properties of trabecular bone, these comparisons are encouraging. Prospective tests need to be performed under multiple loading conditions (including conditions where one or more of the principal stresses is tensile) and with specimens whose trabecular alignment is strictly controlled to determine the predictive accuracy of the model presented here.

Specimen ID	Strength anisotropy ratio	θ (°)	radial/axial stress at failure	predicted radial/axial stress
TR07	3.1	38	0.46	0.17
TR23	3.9	42	0.39	0.12
TR28	4.0	43	0.31	0.13
TR05	1.4	25	0.43	0.34
TR10	1.8	29	0.24	0.20
TR18	2.2	32	0.26	0.21
TR20	2.4	34	0.27	0.25
TR24	1.8	29	0.24	0.15
TR30	1.9	30	0.07	0.06

Table 1: Comparison of measured and predicted ratios of radial to axial stress for nine trabecular bone specimens from the bovine proximal humerus. Data taken from Borchers (1991). A value of θ was chosen for each specimen such that the predicted strength anisotropy ratio (ratio of axial to transverse uniaxial strengths) matched the measured strength anisotropy ratio (ratio of axial strength to average transverse strength).

The failure criterion presented here was developed based on a microstructural element whose geometry can represent a nearly isotropic or transversely isotropic material.

Therefore, the failure surfaces presented here are not necessarily appropriate for fully orthotropic trabecular bone. However, the failure mechanisms active in isotropic and transversely isotropic trabecular bone are likely to be the same as those active in orthotropic trabecular bone. Therefore, the general shapes of the failure surfaces derived here are probably similar to those for orthotropic bone, with the surfaces for orthotropic bone simply scaled according to the uniaxial strengths in the principal material directions.

Although the criterion developed here represents an improvement in our understanding of multiaxial failure mechanisms in trabecular bone, further work is required before the criterion can be effectively used to predict absolute stress magnitudes with high accuracy. The largest obstacle to using this criterion to predict absolute stress magnitudes is the lack of data regarding the compressive and tensile strengths of trabecular tissue. Although several investigators have attempted to measure the elastic properties of trabecular tissue (Townsend *et al.*, 1975; Ashman and Rho, 1988; Kuhn *et al.*, 1989; Mente and Lewis, 1989; Choi *et al.*, 1990), technical difficulties related to the small size of individual trabeculae have precluded accurate measurements of the uniaxial tensile and compressive strengths. Recent developments in micromachining of individual trabeculae (Kuhn *et al.*, 1989), however, may ultimately allow for accurate measurement of trabecular tissue strength properties. In addition to requiring accurate values for the uniaxial strengths of trabecular tissue, the use of the criterion developed here to predict absolute strength values requires an understanding of what model geometric parameters are appropriate for use with particular trabecular architectures and apparent densities. Since the level of anisotropy predicted by the model depends primarily on the geometric parameter θ (and less so on h/l), knowledge of the level of anisotropy in a particular specimen of trabecular bone would allow for an appropriate choice of the parameter θ. When the parameter θ is fixed, the parameter t/l determines the magnitudes of the uniaxial strengths. Therefore, if accurate trabecular tissue properties are known, and if the uniaxial strengths of a specimen of trabecular bone are known (or are estimated from relationships between strength and

density or between strength and architectural parameters), the analytical model presented here allows for the prediction of the strength of that bone specimen under any three-dimensional state of stress. Prospective mechanical tests are needed, along with strength data for trabecular tissue, in order to determine if the criterion developed here can give accurate predictions of failure stress magnitudes. Even without these data, however, the analysis presented here provides substantial insight into the mechanisms of trabecular bone failure under multiaxial loads, and how the shapes of the failure surfaces relate to density and microstructure.

4.8 References

Ashman R. and Rho J. (1988) Elastic modulus of trabecular bone material. *J Biomech* **21**, 177-181.

Borchers R. (1991) *Multiaxial Failure Criteria for Trabecular Bone.* Master's Thesis, Massachusetts Institute of Technology.

Choi K., Kuhn J., Ciarelli M., and Goldstein S. (1990) The elastic moduli of human subchondral, trabecular, and cortical bone tissue and the size-dependence of cortical bone modulus. *J Biomech* **23**, 1103-1113.

Gibson L. and Ashby M. (1988) *Cellular Solids: Structure & Properties*, Pergamon Press, Oxford.

Gibson L. J., Ashby M. F., Zhang J., and Triantafillou T. C. (1989) Failure surfaces for cellular materials under multiaxial loads--I. Modelling. *Int J Mech Sci* **31**, 635-663.

Kuhn J., Goldstein S., Choi K., London M., Feldkamp L., and Matthews L. (1989) A comparison of the trabecular and cortical tissue moduli from human iliac crests. *J Orthop Res* **7**, 874-886.

Lotz J. C., Cheal E. J., and Hayes W. C. (1991a) Fracture prediction for the proximal femur using finite element models: Part 1-Linear analysis. *J Biomech Eng* **113**, 353-360.

Lotz J. C., Cheal E. J., and Hayes W. C. (1991b) Fracture prediction for the proximal femur using finite element models: Part 2-Nonlinear analysis. *J Biomech Eng* **113**, 361-365.

Mente P. and Lewis J. (1989) Experimental method for the measurement of the elastic modulus of trabecular bone tissue. *J Orthop Res* **7**, 456-461.

Townsend P., Rose R., and Radin E. (1975) Buckling studies of single human trabeculae. *J Biomech* **8**, 199-201.

Triantafillou T. C., Zhang J., Shercliff T. L., Gibson L. J., and Ashby M. F. (1989) Failure surfaces for cellular materials under multiaxial loads--II. Comparison of models with experiment. *Int J Mech Sci* **31**, 665-678.

Appendix: Derivation of Failure Surface for States of Stress where Principal Stresses are not Aligned with Principal Material Directions

The analysis is now extended to include cases where the principal stresses are not aligned with the principal material directions, by allowing both normal and shear stresses to act on the microstructural element. In the previous analysis, forces acting on the microstructural element were limited to P_1, P_2, and P_3, which were caused by the application of the remote normal stresses σ_1, σ_2 and σ_3. Now, the forces induced by the application of remote shear stresses τ_{12}, τ_{23}, and τ_{13} are added to the forces P_1, P_2 and P_3. As in the previous analysis, each oblique strut is considered separately, and now the vertical strut is considered in the analysis since it experiences bending as well as axial deformation.

The applied moment and axial stress in strut A are given by

$$M_A = \frac{l}{2}\left\{\left(\left(P_3 + \frac{F_{23,3}}{3}\right)\sin\theta - \left(\frac{P_2}{3} + F_{23,2}\right)\cos\theta\right)^2 + \left(\left(\frac{F_{12,1}}{3} + F_{13,1}\right)\cos\theta\right)^2\right\}^{\frac{1}{2}} \qquad (A.1)$$

$$\sigma_{a,A} = \left\{\left(P_3 + \frac{F_{23,3}}{3}\right)\cos\theta + \left(\frac{P_2}{3} + F_{23,2}\right)\sin\theta\right\}\frac{1}{t^2} \qquad (A.2)$$

where $F_{ij,k}$ is the force on the microstructural element in the k-direction due to the application of the remote shear stress τ_{ij}. Similarly, the applied moments and axial stresses in struts B and C are given by

$$M_B = \frac{l}{2}\left\{\left(\left(P_1 + \frac{F_{12,1}}{3} - \frac{F_{13,1}}{2}\right)\sin\phi - \left(\frac{P_2}{3} + F_{12,2} - \frac{F_{23,2}}{2}\right)\cos\phi\right)^2\left(1 - \frac{1}{4}\cos^2\theta\right)\right.$$
$$\left. + \left(\left(\frac{P_3}{2} - \frac{F_{23,3}}{3} - F_{13,3}\right)\sin\psi - \left(\frac{P_2}{3} + F_{12,2} - \frac{F_{23,2}}{2}\right)\cos\psi\right)^2\left(1 - \frac{3}{4}\cos^2\theta\right)\right\}^{\frac{1}{2}} \quad \text{(A.3)}$$

$$\sigma_{a,B} = \frac{1}{t^2}\left\{\frac{\sqrt{3}}{2}\left(P_1 + \frac{F_{12,1}}{3} - \frac{F_{13,1}}{2}\right)\cos\phi + \left(\frac{P_2}{3} + F_{12,2} - \frac{F_{23,2}}{2}\right)\sin\theta + \frac{1}{2}\left(\frac{P_3}{2} - \frac{F_{23,3}}{3} - F_{13,3}\right)\cos\psi\right\}$$

(A.4)

$$M_C = \frac{l}{2}\left\{\left(\left(P_1 - \frac{F_{12,1}}{3} + \frac{F_{13,1}}{2}\right)\sin\phi - \left(\frac{P_2}{3} - \frac{F_{23,2}}{2} - F_{12,2}\right)\cos\phi\right)^2\left(1 - \frac{1}{4}\cos^2\theta\right)\right.$$
$$\left. + \left(\left(\frac{P_3}{2} - \frac{F_{23,3}}{3} + F_{13,3}\right)\sin\psi - \left(\frac{P_2}{3} - \frac{F_{23,2}}{2} - F_{12,2}\right)\cos\psi\right)^2\left(1 - \frac{3}{4}\cos^2\theta\right)\right\}^{\frac{1}{2}} \quad \text{(A.5)}$$

$$\sigma_{a,C} = \frac{1}{t^2}\left\{\frac{\sqrt{3}}{2}\left(P_1 - \frac{F_{12,1}}{3} + \frac{F_{31,1}}{2}\right)\cos\phi + \left(\frac{P_2}{3} - \frac{F_{23,2}}{2} - F_{12,2}\right)\sin\theta + \frac{1}{2}\left(\frac{P_3}{2} - \frac{F_{23,3}}{3} + F_{13,3}\right)\cos\psi\right\}$$

(A.6)

Finally, the applied moment and axial stress in the vertical strut (strut D) are given by

$$M_D = \frac{h}{2}\left(F_{12,1}^2 + F_{23,3}^2\right)^{\frac{1}{2}} \quad \text{(A.7)}$$

$$\sigma_{a,D} = \frac{P_2}{t^2} \quad \text{(A.8)}$$

It is assumed that the remotely applied shear stresses which act in the 1-2 plane and in the 2-3 plane act over an area proportional to rH, the same area over which the normal stresses σ_1 and σ_3 act. Similarly, it is assumed the shear stresses in the 1-3 plane act over an area proportional to r^2, the same area over which the normal stress σ_2 acts. Therefore, the relationships between the forces $F_{ij,k}$ and the remote shear stresses are the following:

$$
\begin{aligned}
F_{12,1} &= \tau_{12} k_2 r^2 \\
F_{12,2} &= \tau_{12} k_1 rH \\
F_{23,2} &= \tau_{23} k_3 rH \\
F_{23,3} &= \tau_{23} k_2 r^2 \\
F_{13,1} &= \tau_{13} k_3 rH \\
F_{13,3} &= \tau_{13} k_1 rH
\end{aligned}
\tag{A.9}
$$

As in the previous analysis, failure occurs when the applied moment in any strut (Eqns. A.1, A.3, A.5, A.7) reaches its fully plastic moment. The fully plastic moment in each strut is given by Equation 13. Therefore, failure occurs when any one of the following four conditions are met:

Condition 1 (Applied moment = plastic moment in strut A):

$$
\frac{l}{2}\left\{\left(\left(k_3\sigma_3 rH + \frac{k_2}{3}\tau_{23}r^2\right)\sin\theta - \left(\frac{k_2}{3}\sigma_2 r^2 + \tau_{23}k_3 rH\right)\cos\theta\right)^2 + \left(\left(\frac{k_2}{3}\tau_{12}r^2 + k_3\tau_{13}rH\right)\cos\theta\right)^2\right\}^{\frac{1}{2}}
$$

$$
= \frac{t^3}{2\left(\sigma_{ys}^t + \sigma_{ys}^c\right)}\left(\sigma_{ys}^t\sigma_{ys}^c + \left(\sigma_{ys}^t - \sigma_{ys}^c\right)\left[\left(k_3\sigma_3 rH + \frac{k_2}{3}\tau_{23}r^2\right)\cos\theta + \left(\frac{k_2}{3}\sigma_2 r^2 + k_3\tau_{23}rH\right)\sin\theta\right]\frac{1}{t^2}\right.
$$

$$
\left. - \left[\left(k_3\sigma_3 rH + \frac{k_2}{3}\tau_{23}r^2\right)\cos\theta + \left(\frac{k_2}{3}\sigma_2 r^2 + k_3\tau_{23}rH\right)\sin\theta\right]^2\frac{1}{t^4}\right) \tag{A.10}
$$

Condition 2 (Applied moment = plastic moment in strut B):

$$\frac{l}{2}\left\{\left(\left(k_1\sigma_1 rH+\frac{k_2}{3}\tau_{12}r^2-\frac{k_3}{2}\tau_{13}rH\right)\sin\phi-\left(\frac{k_2}{3}\sigma_2 r^2+k_1\tau_{12}rH-\frac{k_3}{2}\tau_{23}rH\right)\cos\phi\right)^2\left(1-\frac{1}{4}\cos^2\theta\right)\right.$$
$$\left.+\left(\left(\frac{k_3}{2}\sigma_3 rH-\frac{k_2}{3}\tau_{23}r^2-k_1\tau_{13}rH\right)\sin\psi-\left(\frac{k_2}{3}\sigma_2 r^2+k_1\tau_{12}rH-\frac{k_3}{2}\tau_{23}rH\right)\cos\psi\right)^2\left(1-\frac{3}{4}\cos^2\theta\right)\right\}^{\frac{1}{2}}$$

$$=\frac{t^3}{2\left(\sigma_{ys}^t+\sigma_{ys}^c\right)}\left(\sigma_{ys}^t\sigma_{ys}^c+\left(\sigma_{ys}^t-\sigma_{ys}^c\right)\frac{1}{t^2}\left(\frac{\sqrt{3}}{2}\left(k_1\sigma_1 rH+\frac{k_2}{3}\tau_{12}r^2-\frac{k_3}{2}\tau_{13}rH\right)\cos\phi\right.\right.$$
$$+\left(\frac{k_2}{3}\sigma_2 r^2+k_1\tau_{12}rH-\frac{k_3}{2}\tau_{23}rH\right)\sin\theta+\frac{1}{2}\left(\frac{k_3}{2}\sigma_3 rH-\frac{k_2}{3}\tau_{23}r^2-k_1\tau_{13}rH\right)\cos\psi\Big)$$
$$-\frac{1}{t^4}\left(\frac{\sqrt{3}}{2}\left(k_1\sigma_1 rH+\frac{k_2}{3}\tau_{12}r^2-\frac{k_3}{2}\tau_{13}rH\right)\cos\phi+\left(\frac{k_2}{3}\sigma_2 r^2+k_1\tau_{12}rH-\frac{k_3}{2}\tau_{23}rH\right)\sin\theta\right.$$
$$\left.\left.+\frac{1}{2}\left(\frac{k_3}{2}\sigma_3 rH-\frac{k_2}{3}\tau_{23}r^2-k_1\tau_{13}rH\right)\cos\psi\right)^2\right) \qquad \text{(A.11)}$$

Condition 3 (Applied moment = plastic moment in strut C):

$$\frac{l}{2}\left\{\left(\left(k_1\sigma_1 rH-\frac{k_2}{3}\tau_{12}r^2+\frac{k_3}{2}\tau_{13}rH\right)\sin\phi-\left(\frac{k_2}{3}\sigma_2 r^2-\frac{k_3}{2}\tau_{23}rH-k_1\tau_{12}rH\right)\cos\phi\right)^2\left(1-\frac{1}{4}\cos^2\theta\right)\right.$$
$$\left.+\left(\left(\frac{k_3}{2}\sigma_3 rH-\frac{k_2}{3}\tau_{23}r^2+k_1\tau_{13}rH\right)\sin\psi-\left(\frac{k_2}{3}\sigma_2 r^2-\frac{k_3}{2}\tau_{23}rH-k_1\tau_{12}rH\right)\cos\psi\right)^2\left(1-\frac{3}{4}\cos^2\theta\right)\right\}^{\frac{1}{2}}$$

$$=\frac{t^3}{2\left(\sigma_{ys}^t+\sigma_{ys}^c\right)}\left(\sigma_{ys}^t\sigma_{ys}^c+\left(\sigma_{ys}^t-\sigma_{ys}^c\right)\frac{1}{t^2}\left(\frac{\sqrt{3}}{2}\left(k_1\sigma_1 rH-\frac{k_2}{3}\tau_{12}r^2+\frac{k_3}{2}\tau_{13}rH\right)\cos\phi\right.\right.$$
$$+\left(\frac{k_2}{3}\sigma_2 r^2-\frac{k_3}{2}\tau_{23}rH-k_1\tau_{12}rH\right)\sin\theta+\frac{1}{2}\left(\frac{k_3}{2}\sigma_3-\frac{k_2}{3}\tau_{23}r^2+k_1\tau_{13}rH\right)\cos\psi\Big)$$
$$-\frac{1}{t^4}\left(\frac{\sqrt{3}}{2}\left(k_1\sigma_1 rH-\frac{k_2}{3}\tau_{12}r^2+\frac{k_3}{2}\tau_{13}rH\right)\cos\phi+\left(\frac{k_2}{3}\sigma_2 r^2-\frac{k_3}{2}\tau_{23}rH-k_1\tau_{12}rH\right)\sin\theta\right.$$
$$\left.\left.+\frac{1}{2}\left(\frac{k_3}{2}\sigma_3-\frac{k_2}{3}\tau_{23}r^2+k_1\tau_{13}rH\right)\cos\psi\right)^2\right) \qquad \text{(A.12)}$$

Condition 4 (Applied moment = plastic moment in vertical strut):

$$\frac{hk_2r^2}{2}\left(\tau_{12}{}^2+\tau_{23}{}^2\right)^{\frac{1}{2}}=\frac{t^3}{2\left(\sigma'_{ys}+\sigma^c_{ys}\right)}\left(\sigma'_{ys}\sigma^c_{ys}+\left(\sigma'_{ys}-\sigma^c_{ys}\right)\frac{k_2\sigma_2r^2}{t^2}-\left(\frac{k_2\sigma_2r^2}{t^2}\right)^2\right) \qquad \text{(A.13)}$$

Chapter 5

The Effect of Impact Direction on the Structural Capacity of the Proximal Femur During Falls

5.1 Introduction

The successful design of intervention efforts to reduce hip fracture incidence depends on a sound understanding of the dominant factors that contribute to hip fracture etiology. The reduction of bone mineral density at the hip with age (Riggs *et al.*, 1982; Steiger *et al.*, 1992), coupled with the demonstrated associations between bone density and femoral strength (Alho *et al.*, 1988; Esses *et al.*, 1989; Lotz and Hayes, 1990; Weber *et al.*, 1992; Courtney *et al.*, 1994; Courtney *et al.*, 1995), demonstrate that age-related bone loss contributes to *in vivo* hip fracture risk. Clinical evidence that the frequency of hip fracture increases as bone mineral density declines below a densitometric fracture threshold supports this contention (Riggs and Melton, 1986). However, since over 90 percent of hip fractures are the result of falls (Hedlund and Lindgren, 1987; Cummings *et al.*, 1990) and fewer than 5 percent of falls result in hip fracture (Tinetti, 1987; Nevitt *et al.*, 1989), the mechanics of falling must also contribute substantially to hip fracture risk. In this regard, both a fall to the side (Greenspan *et al.*, 1994) and impact near the hip (Hayes *et al.*, 1993; Nevitt and Cummings, 1993) have been shown to be significant predictors of hip fracture risk, regardless of bone mineral density. Elucidation of the mechanisms by which fall mechanics influence hip fracture risk, and incorporation of this knowledge into fracture risk assessment techniques, should result in an improved ability to measure hip fracture risk in the clinical setting.

Hip fracture risk can be quantified using a factor of risk, defined as the ratio of the force applied to the proximal femur divided by the structural capacity of the femur (Hayes

and Myers, 1994; Myers and Hayes, 1994). Intrinsic factors that affect the structural capacity include femoral geometry and material properties of the bone tissue. The direction of impact is an extrinsic factor that can also affect the structural capacity, because of the femur's complex geometry and inhomogeneous material properties. Although the role of bone density as a determinant of hip fracture has been extensively investigated *ex vivo* (Alho *et al.*, 1988; Esses *et al.*, 1989; Lotz and Hayes, 1990; Weber *et al.*, 1992; Courtney *et al.*, 1994; Courtney *et al.*, 1995), the contribution of loading direction has been largely ignored. Differences in loading direction may partly explain why investigators have reported structural capacities for fall loading conditions which differ by as much as a factor of three to four (Smith, 1953; Lotz and Hayes, 1990; Weber *et al.*, 1992; Courtney *et al.*, 1994; Courtney *et al.*, 1995, Table 1). Although comparison of these *ex vivo* studies indirectly suggests that loading direction may influence structural capacity, the results are confounded by inter-bone differences in geometry and bone density, as well as inter-study differences in loading rate, and therefore the effect of loading direction independent of these confounding factors is unknown.

It was hypothesized in this study that impact direction, independent of confounding factors such as geometry and bone mineral density, affects both femoral structural capacity and failure location. Testing of this hypothesis is well-suited to the finite element method because failure of a single femur can be simulated under several different loading conditions. In addition, finite element models have previously been used effectively to predict fracture of the femur under both gait and fall loading conditions (Lotz *et al.*, 1991a; Lotz *et al.*, 1991b). Therefore, a three-dimensional finite element model of the proximal femur was developed based on geometry and density data from Quantitative Computed Tomography (QCT) to address the following specific objectives: 1) to compare the structural capacity of the proximal femur under four fall loading configurations representing possible *in vivo* falls on the hip, ranging from a direct lateral impact to a posterolateral impact, and 2) to determine if the direction of impact influences the location of bone failure.

The theoretical information gained from this study should be useful in the development of new fracture risk assessment tools that account for fall mechanics as well as bone mineral density.

Study	Sample size	Force angle (deg)[a]	Diaphysis angle (deg)[b]	Loading rate (mm/sec)	Mean age (yr)	Mean failure load (N) ± S.D.
Smith, 1953	10	~0	not reported	impact	not reported	7330 ± 1000
Lotz, 1990	12	60	30	0.7	69.5	2110 ± 1060
Weber, 1992	10	60	30	0.7	55	2933 ± 1028
	4	60	30	14.0	55	3505 ± 1716
	6	60	30	4000	not reported	6017 ± 2291
Courtney, 1994	8	15	10	2.0	73.5	3440 ± 1330
	9	15	10	2.0	33	7200 ± 1090
	10	15	10	100	73.5	4162[c]
	10	15	10	100	33	8064[c]

[a] Relative to the femoral neck axis, as viewed from the superior aspect of the femoral head
[b] Relative to the horizontal
[c] Standard deviation not reported

Table 1. Literature review of mean values of femoral structural capacity from *ex vivo* studies that have used fall loading conditions. Differences in loading direction may account for the broad range of reported failure loads, although direct comparison is difficult because of inter-study differences in age and loading rate.

5.2 Materials and Methods

5.2.1 Finite Element Model

The right proximal femur from a 49 year-old man was obtained post-mortem. The femur was harvested fresh, and stored frozen at -20° C. Prior to scanning, the bone was thawed at room temperature and placed in a water bath. The bone mineral density of the femoral neck was measured using dual-energy x-ray absorptiometry (DXA; QDR-2000, Hologic, Inc., Waltham, MA), and found to be within the normal range based on age and sex (Wahner and Fogelman, 1994). The submerged femur was then scanned using a clinical CT scanner (model 9800, General Electric, Milwaukee, WI) set at 120 kilovolt potential and 240 milliampereseconds. The femur was scanned perpendicular to the diaphysis, with contiguous 3 mm slices beginning at the superior aspect of the femoral head until just distal to the lesser trochanter, and then with 10 mm slices through the diaphysis. The geometric and densitometric information in the QCT scan set was used to generate a finite element model of the femur using the IBID Software Suite (Hospital for Special Surgery, New York).

The finite element mesh consisted of 20-noded quadratic brick elements with 15-noded wedge elements in transition regions, for a total of 1560 elements and 6527 nodal points (Fig. 1). Bone was modeled as an isotropic but heterogeneous material. To incorporate material heterogeneity, each element in the model was assigned a unique elastic modulus based on the volume-weighted average of the QCT data sampled at 27 points within the element (Edidin, 1991; Keaveny and Bartel, 1993). To calculate the elastic modulus of each element, the following steps were taken. First, a general linear relationship between QCT data (in Hounsfield units, HU) and apparent density was assumed (Hvid *et al.*, 1989; Lotz *et al.*, 1990; Ciarelli *et al.*, 1991). To determine the

constants in this linear relationship, the mean Hounsfield Unit values at the center of the femoral head (449 HU) and in the mid-diaphysis (1650 HU) were matched with literature values reported for modulus, which were 332 MPa for the trabecular bone of the femoral head (Brown and Ferguson, 1978) and 18 GPa for the cortical bone of the diaphysis (Reilly and Burstein, 1975). The resulting equation between QCT data (HU) and apparent density (ρ) was $\rho = 1.106 \times 10^{-3}$ HU + 0.684, where apparent density was expressed in g cm^{-3}, and QCT data were calibrated such that air and water yield values of -1000 HU and 0 HU respectively. A quadratic relationship was then used between apparent density and modulus (E, MPa) for trabecular bone (Rice *et al.*, 1988), along with a linear relationship for cortical bone (Snyder and Schneider, 1991) :

$$E = 820\rho^2 + 70 \qquad \text{(trabecular bone)}$$

$$E = 21910\rho - 23500 \qquad \text{(cortical bone)}$$

The transition point between trabecular and cortical bone was defined at an apparent density of 1.12 g cm^{-3} (with a corresponding modulus of 1100 MPa), based on the intersection point of these empirical relationships. The resulting moduli in the finite element model ranged from 0.1 MPa (representing marrow space) to approximately 18 GPa for the stiffest portion of the diaphysis (Fig. 1). All pre- and post-processing of the finite element model were performed using PATRAN (Version 2.5, PDA Engineering, Costa Mesa, CA), and stresses were computed using ABAQUS (Version 5.3, Hibbitt, Karlsson & Sorensen, Pawtucket, Rhode Island).

5.2.2 Loads and Boundary Conditions

The loading configurations represented falls with lateral to posterolateral impact on the greater trochanter. The boundary conditions were derived from an *ex vivo* femoral

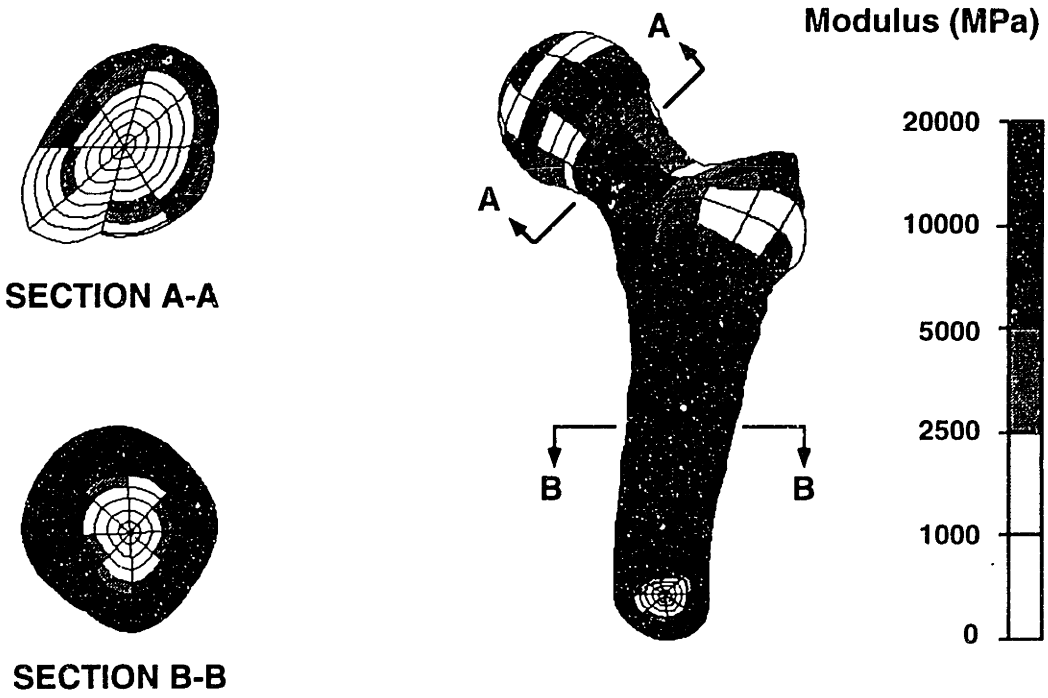

Figure 1: Finite element model of the right proximal femur from a 49 year old male donor, posterior view, showing modulus distribution at proximal (A-A) and distal (B-B) cross sections. The finite element mesh was composed of 1560 20-noded brick elements and 15-noded wedge elements in transition regions, for a total of 6527 nodal points.

fracture study (Courtney *et al.*, 1995) which was based on body configurations at impact during voluntary falls from standing height (van den Kroonenberg *et al.*, 1996). This loading configuration was chosen because it produced *ex vivo* fracture patterns similar to those observed clinically. Using the model, a fall with impact on the lateral aspect of the greater trochanter was simulated by placing the diaphysis of the femur at a 10° angle relative to the horizontal (Fig. 2). The femur was fixed distally against rotation about the diaphyseal axis, simulating the resistance to rotation provided by the knee joint and the inertia of the lower leg during a fall *in vivo*. A distributed load was applied over an area of

approximately 2 cm^2 on the inferior surface of the femoral head, with the resultant force acting through the center of the femoral head. The femoral head was constrained such that it could rotate about its center (simulating sliding of the femoral head within the acetabulum), but the center could translate only in the direction of the applied load (simulating the resistance to femoral head translation provided by the acetabulum). The greater trochanter was constrained vertically (simulating the constraint provided by the impact surface during a fall), but free to slide in the horizontal plane. Four variations of this loading condition were examined, all simulating falls with impact on the greater trochanter, but with variation in the angle between the load vector and the femoral neck axis (as viewed from the superior aspect of the femoral head). An angle of 15° (Fig. 3B) represented a typical body position at impact during experimental sideways falls (van den Kroonenberg *et al.*, 1996). This configuration has been shown to produce clinically realistic fracture patterns in *ex vivo* fracture studies (Courtney *et al.*, 1994; Bouxsein *et al.*, 1995; Courtney *et al.*, 1995). An angle of 0° simulated a fall in which the femur impacts in a more direct lateral direction on the greater trochanter relative to the 15° case (Fig. 3A). Angles of 30° and 45° represented falls in which the femur impacts more posterolaterally relative to the 15° case (Figs. 3C, D)

5.2.3 Failure Criterion

The non-linear stress-strain behavior of bone was simulated using an elastic-perfectly plastic material model based on the von Mises failure criterion. Differences between the tensile and compressive strengths for both cortical and trabecular bone were modeled as follows. First, the principal stresses in each element were determined using a linear elastic analysis. The primary mode of deformation in each element was then determined by comparing the absolute value of the maximum (tensile) and minimum (compressive) principal stresses. For elements where the tensile principal stress was

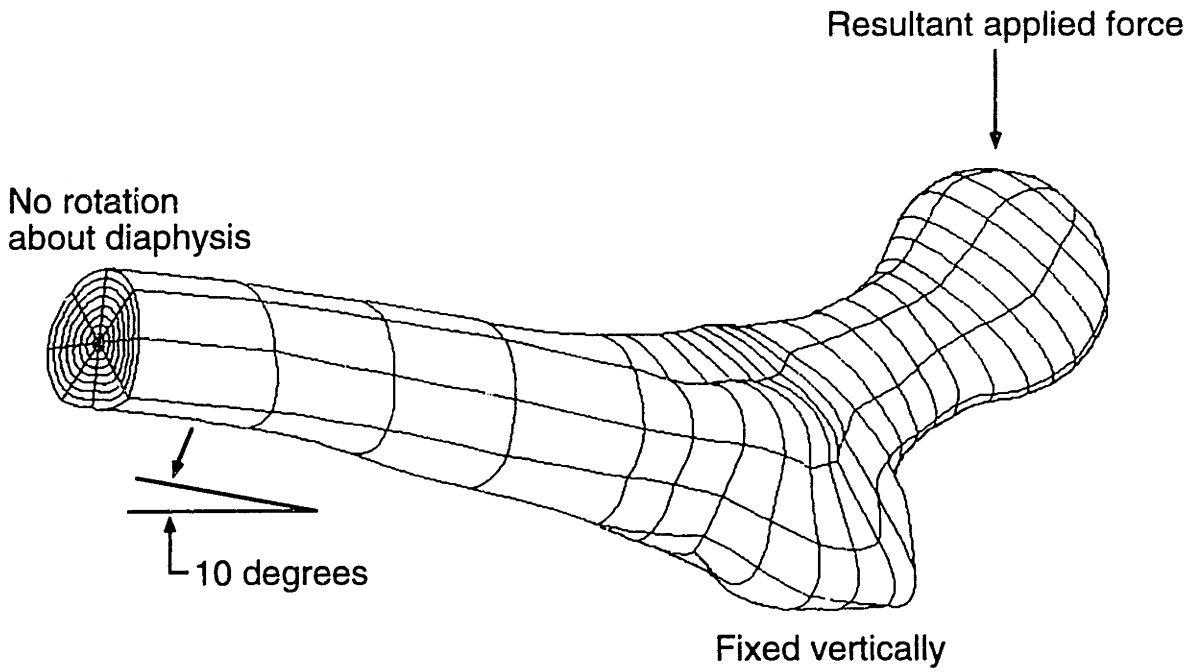

Figure 2: Boundary conditions used for all load cases. The angle of the femoral shaft with respect to the horizontal was 10°. The distal surface was constrained against rotation about the diaphyseal axis, and the greater trochanter was fixed vertically but free to slide in the horizontal plane. A force was applied vertically to the inferior surface of the femoral head, with the resultant acting through the center of the femoral head.

largest, strengths were assigned by multiplying the elastic modulus of the element by a constant tensile yield strain of 0.8% (based on reported yield strain values for trabecular bone [Keaveny *et al.*, 1994] and unpublished values for cortical bone). For elements where the compressive principal stress was largest, strengths were assigned by multiplying the elastic modulus by a constant compressive yield strain of 1.0% (Keaveny *et al.*, 1994). This technique resulted in maximum assigned tensile and compressive strengths of 144 MPa and 180 MPa, respectively, which is consistent with experimental results for cortical bone (Reilly and Burstein, 1975). Yielding in an individual element occurred when the

effective von Mises stress in the element reached the assigned strength of the element. The structural capacity of the femur was defined as the force required to cause the peak strain in cortical bone loaded in tension to reach an ultimate value of 3% (Reilly and Burstein, 1975), corresponding to the onset of structural collapse.

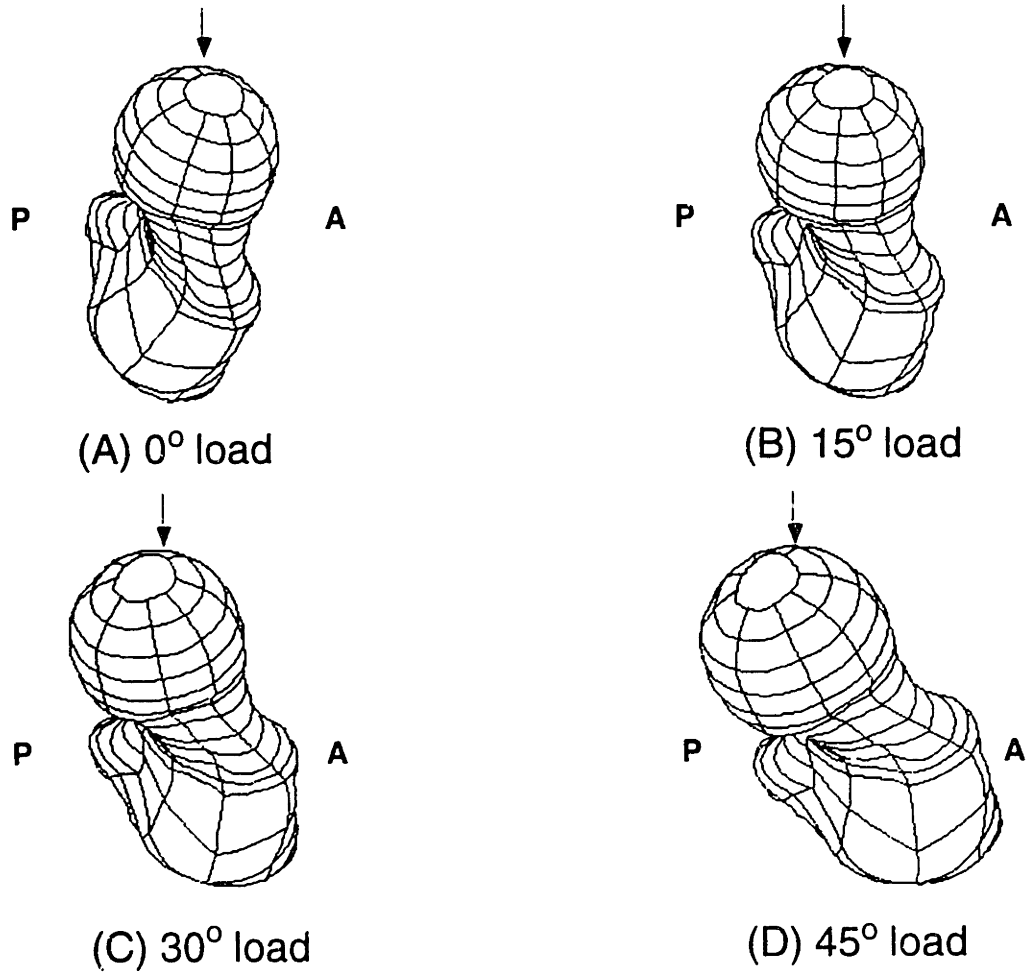

Figure 3: Variations in impact direction examined (view of right femur, looking down femoral axis from superior aspect of femoral head). The 15° case (B) represented a typical fall impacting on the greater trochanter. The 0° case (A) simulated a fall with the femur externally rotated relative to the 15° case, with impact occurring in a more direct lateral direction. The 30° and 45° cases represented falls with impact occurring more posterolaterally relative to the 15° case. A = anterior, P = posterior.

5.3 Results

As hypothesized, the structural capacity of the femur was highly dependent on the direction of impact, with differences in structural capacity of up to 26% depending on impact direction. The lowest predicted force of 2090 N occurred in the 45° case, and was 26% lower than the maximum force of 2820 N, which occurred in the 0° case (Fig. 4). A structural capacity reduction of 21% (from 2820 N to 2240 N) was predicted with a change of impact direction from 0° to 30°, and a reduction of 12% (from 2820 N to 2470 N) was predicted between 0° and 15°.

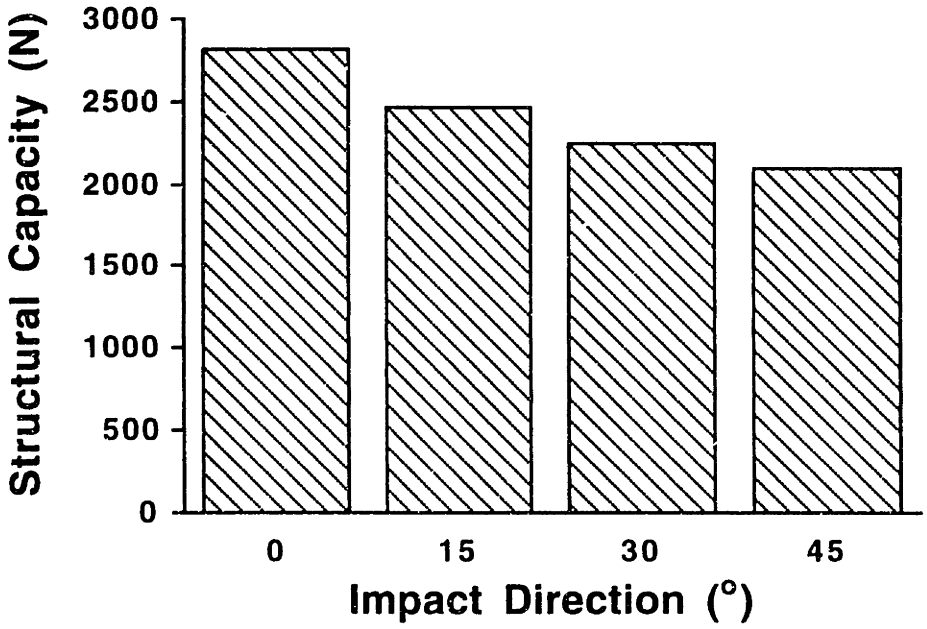

Figure 4: Structural capacity as a function of impact direction. The lowest structural capacity (2090 N) occurred in the 45° case, and was 26% lower than the maximum structural capacity (2820 N) which occurred in the 0° case.

By contrast to the range of structural capacities, the location of bone failure was similar in all cases. Local yielding was predicted first in the superior basicervical region, and subsequently spread to the inferior subcapital and midneck regions (Fig. 5). Ultimate failure of cortical bone in each case occurred at the inferior midneck. Therefore, although impact direction had a profound effect on structural capacity, it did not substantially effect the predicted fracture pattern.

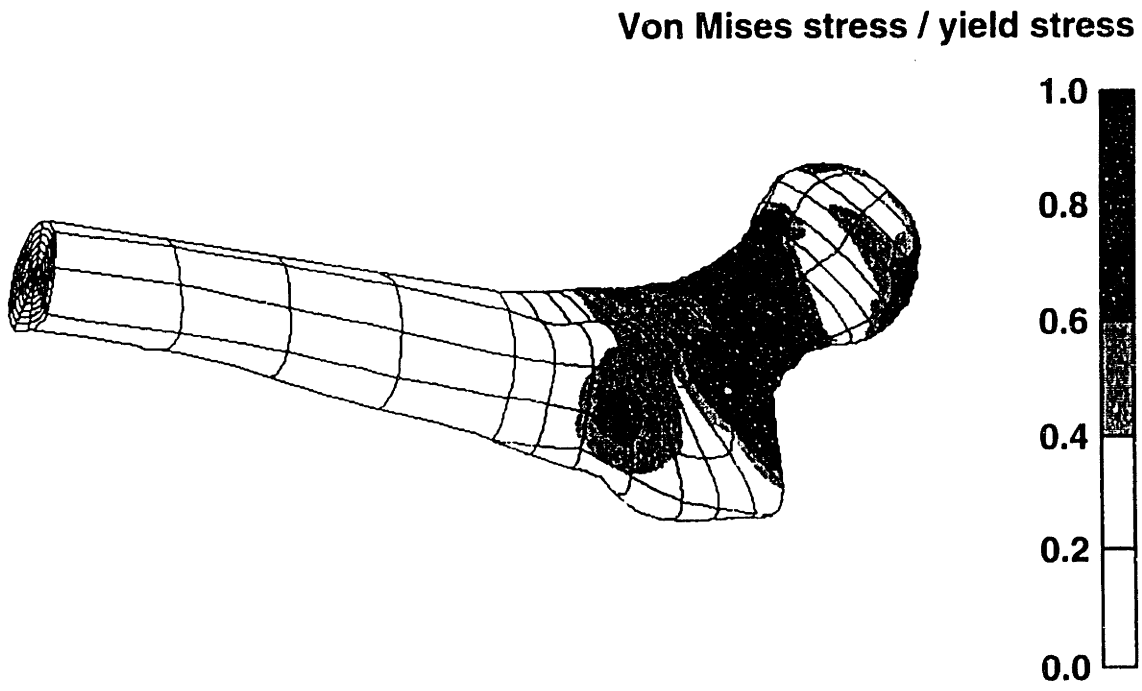

Figure 5: Contour plot of the ratio of von Mises stress to yield stress at the point of structural failure for the 0^{o} case. The stress distribution was qualitatively similar for all loading cases, with high stress ratios occurring in the midneck and superior basicervical regions. Ultimate tensile failure of cortical bone occurred at the inferior midneck.

5.4 Discussion

The objectives of this chapter were to quantify the effect of impact direction on femoral structural capacity during falls on the greater trochanter, where all potentially confounding effects such as inter-bone variations in density and geometry were eliminated, and also to determine if impact direction influences the location of bone failure. A change in the angle between the axis of the femoral neck and the line of action of the applied force from 0° (representing direct lateral impact) to 45° (representing posterolateral impact) decreased structural capacity by 26%, but did not affect the location of bone failure. These results indicate that the direction of impact is an important determinant of fall severity, and therefore the data obtained in this study can provide the basis for improving hip fracture risk prediction in the clinical setting.

Several important strengths of this study relate to the structural model used. First, failure of a single femur was modeled under several loading conditions, therefore eliminating the confounding effects of inter-bone variations in geometry and bone density. Second, the model incorporated detailed geometry as well as the full range of material heterogeneity found within the femur, which has not been done previously in finite element models of the femur during falls. Third, the three-dimensional nature of the model allowed incorporation of loads which lie outside the frontal plane, producing more physiological femoral loading conditions than have been used previously (Beck *et al.*, 1990; Yoshikawa *et al.*, 1994). The finding that the femur is weakest under loads that lie outside the frontal plane emphasizes that out-of-plane loading is an important consideration in the assessment of hip fracture risk. Fourth, the criterion used to determine bone failure accounted for the multiaxial nature of the strains within bone, as well as the strength asymmetries of both cortical and trabecular bone. Finally, the model predicted failure locations that are clinically realistic, lending support to both the validity of the model itself and to the loading configurations used. While the use of a single femur from a relatively young (49 year old)

donor may limit the generality of the results, recent *ex vivo* data suggest the reported trends do have generality. In particular, it has been shown that once bone mineral density is accounted for, elderly femurs tested to failure at 30° (n = 11) are 24% weaker than those tested at 0° (n = 11; Pinilla *et al.*, 1996), which compares favorably with the 21% reduction predicted by the finite element model. The strong agreement between the trends predicted by the model and these experimental results for elderly femurs supports the external validity of the results.

While the relative trends predicted by the model and therefore the conclusions are valid, the absolute magnitudes of the predicted structural capacities may be sensitive to modeling parameters such as the isotropy of the bone material properties and the chosen failure criterion. These modeling parameters may explain why the predicted failure load of 2470N for the 15° case is somewhat lower than the failure load of 3140N measured in the laboratory for the modeled femur. Since apparent density explains approximately 80% of the variance in trabecular bone modulus (Rice *et al.*, 1988), and the addition of architectural parameters results in only slight improvements in predictive accuracy (Snyder and Hayes, 1990), the use of fully heterogeneous but isotropic material properties for trabecular bone is reasonable. Most of the discrepancy between predicted and measured failure loads is probably due to the fact that while the material properties assigned to the model were appropriate for quasi-static loading, the loading rate used to measure the failure load in the laboratory (50 mm/sec) more closely reflected the fast loading rate experienced by the femur during a fall. An increase in loading rate from quasi-static conditions to conditions appropriate for a fall increases the structural capacity of the femur by approximately 20% (Courtney *et al.*, 1994). An increase of 20% would result in a model prediction of 2960N for fast loading, which is only 6% less than the measured value of 3140N.

With respect to the choice of failure criterion, element strengths were assigned based on observations that failure strains for bone are constant and independent of density and direction (Vahey *et al.*, 1987; Keaveny *et al.*, 1994), and also incorporated the strength

asymmetries of cortical and trabecular bone (Keaveny *et al.*, 1994). The major difference between the von Mises yield condition used here and either the analytical criterion developed in Chapter 4 or the Tsai-Wu criterion presented in Chapter 2 is that while the analytical and Tsai-Wu criteria depend on both the deviatoric and mean stresses in the material, the von Mises depends only on the deviatoric stress. The contribution of the mean and deviatoric stresses to the failure behavior of a cellular material is most readily demonstrated in the following equation describing the failure surface from Gibson and Ashby (1988):

$$\frac{\sigma_d}{\sigma^*} + 0.81\left(\frac{\sigma_m}{\sigma^*}\right)^2 = 1 \qquad (1)$$

where σ_d is the deviatoric stress, σ^* is the compressive yield stress, ρ^*/ρ_s is the relative density, and σ_m is the mean stress. If the term involving the mean stress is small relative to the term involving the deviatoric stress, then the equation essentially reduces to the von Mises yield condition. Post-processing of the finite element results revealed that for all yielded trabecular bone elements, the term in Equation 1 that includes the mean stress had a magnitude that was at most 0.014% of the magnitude of the term involving the deviatoric stress (even for apparent densities as large as 1.0). Therefore, for the states of stress present in this particular finite element model, incorporation of a failure criterion with a mean stress dependence would not significantly alter the results. However, for states of stress in trabecular bone where mean stresses are significant relative to deviatoric stresses (which could arise in the femur for other loading conditions or at anatomic sites other than the femur), the use of a failure criterion that incorporates mean stress effects would be important for accurate failure prediction.

To place the effects of impact direction in perspective relative to other factors which contribute to hip fracture, it is possible to compare the predicted changes in structural

capacity as a function of impact direction with an estimate of the change that occurs due to age-related bone loss. An average individual experiences a uniform bone loss of 7% per decade (Mazess, 1982). Using a linear relationship between femoral neck bone mineral density and femoral fracture force reported by Courtney *et al.* (1995), this 7% per decade bone loss is associated with a structural capacity reduction of approximately 10% per decade. Therefore, the predictions suggest that the effect of changes in impact direction on the femur (a potential weakening of 26%) is comparable to the effect of two to three decades of age-related bone loss.

These findings may provide the basis for improving estimates of an individual's risk for hip fracture in the clinical setting. Current techniques for estimating hip fracture risk relate the force applied to the femur to its structural capacity for a single fall loading condition (Myers *et al.*, 1994; Yoshikawa *et al.*, 1994). The finding that the structural capacity of the femur is sensitive to impact direction indicates that current fracture risk predictions are also sensitive to the impact direction considered. Since soft tissue can attenuate the force delivered to the femur during a fall (Robinovitch *et al.*, 1994), it is likely that the magnitude of the external force applied to the femur is also a function of impact direction. A refined estimate of an individual's fracture risk, that accounts for interactions between impact direction and soft tissue attenuation, could be achieved by considering a series of high-risk loading conditions (i.e., falls impacting the greater trochanter in a lateral to posterolateral direction as described in this study). The attenuation properties of an individual's trochanteric soft tissue could be estimated using measurements of tissue thickness (Maitland *et al.*, 1993) combined with data relating thickness to attenuation properties (Robinovitch *et al.*, 1994). This information, plus knowledge of body habitus, would provide estimates of the force delivered to the femur for the chosen impact directions. Then, the structural capacities of the femur for the same set of impact directions could be estimated using *ex vivo* data relating bone mineral density to structural capacity (Bouxsein *et al.*, 1995; Courtney *et al.*, 1995), combined with percentage changes in

structural capacity with impact direction reported in this study. The individual's fracture risk, then, would simply be the maximum calculated ratio of applied force to structural capacity for the range of impact directions considered. This scheme for assessing fracture risk could be further refined by weighting each calculated ratio by the probability of impact occurring in that particular direction, although further research into fall mechanics is required to produce this information. Even without this probability data, however, this scheme represents a logical step in the development of fracture risk assessment tools that consider the complex interactions between fall severity and bone fragility.

In summary, the structural capacity of the femur during falls is sensitive to changes in the direction of impact, and the magnitude of this effect is comparable to the effect of two to three decades of age-related bone loss. This finding supports the notion that factors related to fall mechanics are independent contributors to hip fracture risk (Hayes *et al.*, 1993; Nevitt and Cummings, 1993; Greenspan *et al.*, 1994), and provides further insight into why measurements of bone density only partially reflect the full domain of hip fracture risk. The most important clinical implication of this finding is that accurate evaluation of hip fracture risk for an individual requires consideration of a range of femoral structural capacities, since *in vivo* traumatic loads are not known a priori and can vary substantially. In addition, the effects of impact direction must be considered when evaluating new modalities for reducing fracture risk, particularly in the evaluation of therapeutic interventions aimed at slowing age-related bone loss. Future modeling efforts directed toward further quantifying the independent effects of aging and loading on structural capacity for a wide range of femoral morphologies, as well as potential interactions between these effects, should increase our understanding of hip fracture etiology and improve our ability to predict hip fracture risk.

5.5 References

Alho A., Husby T., and Hoiseth A. (1988) Bone mineral content and mechanical strength: an *ex vivo* study on human femora at autopsy. *Clin Orthop* **227**, 292-297.

Beck T. J., Ruff C. B., Warden K. E., Scott W. W., and Rao G. U. (1990) Predicting femoral neck strength from bone mineral data: A structural approach. *Invest Radiol* **25**, 6-18.

Bouxsein M., Courtney A., and Hayes W. (1995) Ultrasound and densitometry of the calcaneus correlate with the failure loads of cadaveric femurs. *Calcif Tissue Int* **56**, 99-103.

Brown T. D. and Ferguson A. B. (1978) The development of a computational stress analysis of the femoral head. *J Bone Joint Surg* **60-A**, 619-629.

Ciarelli M. J., Goldstein S. A., Kuhn J. L., and Cody D. D. (1991) Evaluation of orthogonal mechanical properties and density of human trabecular bone from the major metaphyseal regions with materials testing and computed tomography. *J Orthop Res* **9**, 674-682.

Courtney A. C., Wachtel E. F., Myers E. R., and Hayes W. C. (1994) Effects of loading rate on strength of the proximal femur. *Calcif Tissue Int* **55**, 53-58.

Courtney A. C., Wachtel E. F., Myers E. R., and Hayes W. C. (1995) Age-related reductions in the strength of the femur tested in a fall loading configuration. *J Bone Joint Surg [Am]* **77**, 387-395.

Cummings S. R., Black D. M., and Nevitt M. C. (1990) Appendicular bone density and age predict hip fracture in women. *JAMA* **263**, 665-668.

Edidin A. A. (1991) *Modeling of bone material properties from CT scans - Considerations in biomechanical structural models.* PhD Dissertation, Cornell University.

Esses S. I., Lotz J. C., and Hayes W. C. (1989) Biomechanical properties of the proximal femur determined in vitro by single-energy quantitative computed tomography. *J Bone Min Res* **4**, 715-722.

Gibson L. and Ashby M. (1988) *Cellular Solids: Structure & Properties*, Pergamon Press, Oxford.

Greenspan S. L., Myers E. R., Maitland L. A., Resnick N. M., and Hayes W. C. (1994) Fall severity and bone mineral density as risk factors for hip fracture in ambulatory elderly. *JAMA* **271**, 128-133.

Hayes W. C. and Myers E. R. (1994) Biomechanics of age-related fracture risk. In *Osteoporosis: Etiology, Diagnosis and Management*, Ed. Riggs B. L., and Melton L. J., Raven Press, New York.

Hayes W. C., Myers E. R., Morris J. N., Gerhart T. N., Yett H. S., and Lipsitz L. A. (1993) Impact near the hip dominates fracture risk in elderly nursing home residents who fall. *Calcified Tissue International* **52**, 192-198.

Hedlund R. and Lindgren U. (1987) Trauma type, age and gender as determinants of hip fracture. *J Orthop Res* **5**, 242-246.

Hvid I., Bentzen S. M., Linde F., Mosekilde L., and Pongsoipetch B. (1989) X-ray quantitative computed tomography: the relations to physical properties of proximal tibial trabecular bone specimens. *J Biomech* **22**, 837-844.

Keaveny T. M. and Bartel D. L. (1993) Effects of porous coating and collar support on early load transfer for a cementless hip prosthesis. *J Biomech* **26**, 1205-1216.

Keaveny T. M., Wachtel E. F., Ford C. M., and Hayes W. C. (1994) Differences between the tensile and compressive strengths of bovine tibial trabecular bone depend on modulus. *J Biomech* **27**, 1137-1146.

Lotz J. C., Cheal E. J., and Hayes W. C. (1991a) Fracture prediction for the proximal femur using finite element models: Part 1-Linear analysis. *J Biomech Eng* **113**, 353-360.

Lotz J. C., Cheal E. J., and Hayes W. C. (1991b) Fracture prediction for the proximal femur using finite element models: Part 2-Nonlinear analysis. *J Biomech Eng* **113**, 361-365.

Lotz J. C., Gerhart T. N., and Hayes W. C. (1990) Mechanical properties of trabecular bone from the proximal femur: a quantitative CT study. *J Comp Assist Tomog* **14**, 107-114.

Lotz J. C. and Hayes W. C. (1990) The use of quantitative computed tomography to estimate risk of fracture of the hip from falls. *J Bone Joint Surg [Am]* **72**, 689-700.

Maitland L., Myers E., Hipp J., Hayes W., and Greenspan S. (1993) Read my hips: Measuring trochanteric soft tissue thickness. *Calcif Tissue Int* **52**, 85-89.

Mazess R. B. (1982) On aging bone loss. *Clin Orthop* **165**, 239-252.

Myers E., Robinovitch S., Greenspan S., and Hayes W. (1994) Factor of risk is associated with frequency of hip fracture in a case-control study. *Trans 40th ORS* **19**, 526.

Myers E. R. and Hayes W. C. (1994) Age-related hip fractures. *Current Opinion in Orthopaedics* **5**, 9-15.

Nevitt M. C. and Cummings S. R. (1993) Type of fall and risk of hip and wrist fractures: The study of osteoporotic fractures. *J Am Geriatr Soc* **41**, 1226-1234.

Nevitt M. C., Cummings S. R., Kidd S., and Black D. (1989) Risk factors for recurrent nonsyncopal falls: A prospective study. *JAMA* **261**, 2663-2668.

Reilly D. T. and Burstein A. H. (1975) The elastic and ultimate properties of compact bone tissue. *J Biomech* **8**, 393-405.

Rice J. C., Cowin S. C., and Bowman J. A. (1988) On the dependence of the elasticity and strength of cancellous bone on apparent density. *J Biomech* **21**, 155-168.

Riggs B. L. and Melton L. J. (1986) Involutional osteoporosis. *New England J Med* **314**, 1676-1686.

Riggs B. L., Wahner H. W., Seeman E., Offord K. P., Dunn W. L., Mazess R. B., Johnson K. A., and Melton L. J. (1982) Changes in bone mineral density of the proximal femur and spine with aging. *J Clin Invest* **70**, 716-723.

Robinovitch S. N., McMahon T. A., and Hayes W. C. (1994) Increased soft tissue thickness over the hip lowers femoral impact force during simulated falls on the hip. *Trans 40th ORS* **19**, 528.

Smith L. D. (1953) The role of muscle contraction or intrinsic forces in the causation of fractures of the femoral neck. *J Bone Joint Surg* **35-A**, 367-383.

Snyder B. D. and Hayes W. C. (1990) Multiaxial Structure-Property Relations in Trabecular Bone. In *Biomechanics of Diarthrodial Joints*, 31-59, Ed. Mow V. C., Ratcliffe A., and Woo S. L.-Y., Springer-Verlag, New York.

Snyder S. M. and Schneider E. (1991) Estimation of mechanical properties of cortical bone by computed tomography. *J Orthop Res* **9**, 422-431.

Steiger P., Cummings S. R., Black D. M., Spencer N. E., and Genant H. K. (1992) Age-related decrements in bone mineral density in women over 65. *J Bone Miner Res* **7**, 625-632.

Tinetti M. E. (1987) Factors associated with serious injury during falls among elderly persons living in the community. *J. Am Geriatr Soc* **35**, 644-648.

Vahey J. W., Lewis J. L., and Vanderby R. (1987) Elastic moduli, yield stress, and ultimate stress of cancellous bone in the canine proximal femur. *J Biomech* **20**, 29-33.

van den Kroonenberg A., Hayes W. C., and McMahon T. A. (1996) Hip impact velocities and body configurations for voluntary falls from standing height. *J Biomech* **29**, 807-811.

Wahner H. W. and Fogelman I. (1994) *The Evaluation of Osteoporosis: Dual Energy X-Ray Absorptiometry in Clinical Practice*, University Press, Cambridge, England.

Weber T. G., Yang K. H., Woo R., and Fitzgerald R. H. (1992) Proximal femur strength: Correlation of the rate of loading and bone mineral density. *ASME Adv in Bioengineering* **22**, 111-114.

Yoshikawa T., Turner C. H., Peacock M., Slemenda C. W., Weaver C. M., Teegarden D., Markwardt P., and Burr D. B. (1994) Geometric structure of the femoral neck measured using Dual-Energy X-Ray Absorptiometry. *J Bone Min Res* **9**, 1053-1064.

Chapter 6

Three-Dimensional Patterns of Bone Loss in the Proximal Femur

6.1 Introduction

Age-related reductions in bone density are an important etiologic determinant of hip fractures in the elderly. Prospective cohort studies have repeatedly demonstrated associations between densitometric indicators of osteopenia and the incidence of hip fracture (Cummings *et al.*, 1990; Cummings *et al.*, 1993; Melton *et al.*, 1993; Nevitt *et al.*, 1994; Cummings *et al.*, 1995). For example, a study of over 9000 women 65 years and older demonstrated that a decrease in femoral bone mineral density (BMD) of one standard deviation is associated with a 2.6-fold increase in the age-adjusted risk of hip fracture (Cummings *et al.*, 1993). Long-term follow-up of over 300 women has also shown that a one standard deviation in femoral BMD is equivalent, in terms of fracture risk, to a 13-year increase in age (Melton *et al.*, 1993). The results of several case-control studies (Riggs *et al.*, 1982; Mazess *et al.*, 1988; Aloia *et al.*, 1992; Greenspan *et al.*, 1994b) are consistent with these longitudinal investigations.

Although the existence of a connection between age-related bone loss and increased hip fracture risk is indisputable, the precise relationship between a reduction in bone density and a reduction in structural capacity of the femur has not been adequately explained. The ability of the femur to bear loads is directly related to its material properties, which are determined by the three-dimensional distribution of bone density. Any change in density distribution (such as that which occurs as an individual experiences bone loss) results in a change in the distribution of material properties, with a concomitant change in stress distribution and load-bearing capacity of the femur. If reductions in bone density are

non-uniform in the femur, then the resulting redistribution of material properties and therefore stresses may be dramatic given the power law relationships that relate density to bone modulus and strength (Carter and Hayes, 1976; Rice *et al.*, 1988). Detailed knowledge of the three-dimensional patterns of bone loss in the femur, then, is critical to explaining the relationship between bone loss and increased fracture risk. Despite their potential importance, the three-dimensional patterns of bone loss that occur with aging in the femur are unknown.

The rate of bone loss experienced by an individual can depend, among other factors, on the type of bone (i.e. cortical versus trabecular), the age of the individual, and anatomic site (Mazess, 1982). On average, women lose about one third of their cortical bone and half of their trabecular bone over their lifetime; however, age-related decrements in bone density can differ depending on anatomic site (Riggs *et al.*, 1981; Riggs *et al.*, 1982; Schaadt and Bohr, 1988; Elliot *et al.*, 1990; Hannan *et al.*, 1992; Harris and Dawson-Hughes, 1992; Steiger *et al.*, 1992; Greenspan *et al.*, 1994a). Much of the apparently conflicting data from anatomical and densitometric studies regarding rates of trabecular bone loss (Riggs and Melton, 1986) can probably be explained by inter-study differences in anatomic site used for density assessment. However, in addition to differences in bone loss that exist *between* skeletal sites, there is also evidence to suggest that bone loss is variable *within* certain skeletal sites. For example, in the proximal femur, both longitudinal (Greenspan *et al.*, 1994a) and cross-sectional studies (Riggs *et al.*, 1982; Hannan *et al.*, 1992; Steiger *et al.*, 1992; Greenspan *et al.*, 1994a) have revealed differential rates of bone loss in the femoral neck, trochanteric, and intertrochanteric regions using clinical densitometric techniques.

Although densitometric techniques such as DXA and dual-photon absorptiometry (DPA) have provided valuable clinical information regarding age-related bone loss, these technologies are limited because they provide only a two-dimensional projection of an individual's density distribution, and also because their output is dependent on bone

geometry. Therefore, data generated from these techniques cannot be used to assess patterns of age-related bone loss in three dimensions. In addition to densitometric studies, patterns of bone loss have been investigated in cadaveric femurs using both histomorphometry (Kawashima and Uhthoff, 1991) and radiography (Singh *et al.*, 1970). As with most clinical densitometric methods, however, these methods are inherently limited to analysis of density in a single plane (generally the frontal plane). The fact that the femur is particularly weak under loads that lie outside of the frontal plane (as demonstrated in Chapter 5) underscores the need for density information that is three-dimensional and not confined to projections in the frontal plane. In addition, the fact that rates of BMD loss in the femur can depend on location in the frontal plane (Greenspan *et al.*, 1994a) suggests that there are likely to be gradients in bone loss in the sagittal and coronal planes as well.

By contrast to clinical densitometric techniques such as DXA, Quantitative Computed Tomography (QCT) can provide extremely detailed three-dimensional bone density information. Due to its relatively high cost, high radiation dose, and difficulties in repositioning, QCT is much less practical than DXA for clinical assessment of femoral bone density. However, comparison of QCT data from cadaveric femurs can potentially provide a wealth of information regarding three-dimensional patterns of age-related bone loss, provided that the confounding effects of inter-bone differences in geometry can be accounted for. In this study, a geometric scaling technique was developed that allowed direct comparison of the three-dimensional QCT density distributions of cadaveric femurs with varying geometries. The specific objectives were to: 1) apply this scaling algorithm to QCT data from three groups of cadaveric femurs (chosen to represent a wide range of BMD levels) to determine the relationship between three-dimensional QCT density distribution and BMD, and 2) to use this relationship to determine (cross-sectionally) the three-dimensional patterns of bone loss associated with BMD levels defined as normal, osteopenic, and osteoporotic by an expert panel of the World Health Organization (Kanis *et al.*, 1994).

6.2 Methods

6.2.1 Development and Validation of Relationship between BMD Level and Three-Dimensional Density Distribution

Through previous *ex vivo* fracture studies of the proximal femur performed in this laboratory (Courtney *et al.*, 1994; Courtney *et al.*, 1995; Pinilla *et al.*, 1996), both QCT and DXA data were available for a large number of femurs spanning a broad range of ages and BMD levels. QCT and DXA data for all femurs were obtained using the following protocols. Proximal femurs were placed in water and fixed distally such that both the diaphysis and femoral neck were parallel with the scan table. QCT scanning was performed using the bone algorithm of a clinical CT scanner (model 9800, General Electric, Milwaukee, WI). Scans were taken perpendicular to the diaphysis, with contiguous three mm slices beginning at the superior aspect of the femoral head until just distal to the lesser trochanter, and then with 10 mm slices to the mid-diaphysis. Femurs were positioned in water in the same manner for DXA scanning. DXA scans of each femur were obtained using the pencil-beam mode of a Hologic QDR-2000 densitometer (Hologic Inc., Waltham, MA). Standard measures of areal bone mineral density and bone mineral content were obtained for the femoral neck, trochanteric, and intertrochanteric regions (Wahner and Fogelman, 1994).

The DXA database was examined to identify three groups of femurs whose BMD values were high, medium, and low relative to the available population. Although complete medical records were not available for the femur donors, the available information (Table 1) was used to rule out metastatic disease or disorders known to directly affect bone metabolism. Three femurs were chosen at each BMD level such that when average regional BMD values were calculated for each group (in the femoral neck, trochanteric and

intertrochanteric regions), the coefficients of variation in BMD were as small as possible. Therefore, each group (high-BMD, mid-BMD, and low-BMD) consisted of three femurs with different geometries but similar BMD values (Table 2).

Using publicly available software (NIH Image, version 1.58), the transverse QCT dataset for each femur (Fig. 1a) was reconstructed and resliced in the frontal plane to create a stack of consecutive frontal images. The axis of the femoral neck was identified from the frontal images, and then the frontal stack was resliced perpendicular to the neck axis, with the position and thickness of the slices determined by anatomic landmarks as follows. First, a line perpendicular to the neck axis was placed such that it was tangent to the medial aspect of the femoral head. Five contiguous slices were taken between this position and the start of the femoral neck (subcapital site, Fig. 1b). Five contiguous slices were then taken between the subcapital site and the base of the femoral neck, defined as the point where the line just contacted the tip of the greater trochanter. Another five contiguous slices were taken from the base of the femoral neck to the edge of the trochanteric region, defined by the most lateral point on the femur.

Age (yrs.)	Sex	Cause of death
High-BMD group:		
21	F	Pulmonary embolus
48	M	Head trauma; motor vehicle accident
31	F	Primary brain tumor
Mid-BMD group:		
78	F	Sepsis; bladder cancer
83	F	Cardiogenic shock
69	F	Hepatic failure
Low-BMD group:		
88	F	Sepsis
79	F	Myocardial infarction
89	F	Myocardial infarction

Table 1: Age at time of death, sex and cause of death of femur donors.

ID	Sex	Group	femoral neck BMD ($g\ cm^{-2}$)	trochanteric BMD ($g\ cm^{-2}$)	intertrochanteric BMD ($g\ cm^{-2}$)
1293	F	L	0.451	0.439	0.676
1328	F	L	0.423	0.422	0.713
1355	F	L	0.393	0.411	0.578
mean ± S.D.			0.422 ± 0.029	0.424 ± 0.014	0.656 ± .070
1233	F	M	0.695	0.692	0.907
1317	F	M	0.694	0.598	0.966
1386	F	M	0.691	0.558	0.901
mean ± S.D.			0.693 ± 0.002	0.616 ± 0.069	0.924 ± 0.036
9018	F	H	0.909	0.745	1.126
9037	M	H	0.864	0.737	1.152
9044	F	H	0.901	0.792	1.225
mean ± S.D.			0.891 ± 0.024	0.758 ± 0.030	1.168 ± 0.051

Table 2: Regional BMD values of cadaveric femurs used to derive a relationship between BMD and three-dimensional density distribution. F, female; M, male; L, low-BMD group; M, mid-BMD group; H, high-BMD group.

Once the QCT data from all nine femurs were sampled according to the above protocol, a geometric scaling algorithm was applied to each slice which mapped the density distributions to a constant geometry (Fig. 1c), and therefore facilitated inter-bone comparisons of density distribution. First, a smoothing and an edge detection filter were applied to each slice. The edge detection filter generated both horizontal and vertical derivatives at each point, and replaced each pixel of the original slice with the larger of the two derivative values. The contour representing the outer edge of each slice was then identified by thresholding the filtered image. The contour just inside the outer boundary where the cortical density was a maximum was also identified. The bone pixels within the outer boundary were then mapped to a constant geometry using in-house software as

follows. After locating the medial and lateral borders of a slice, each line of pixels in the anterior/posterior direction was interpolated such that it spanned a distance of 150 points. The resulting rectangular array was then reinterpolated in the medial/lateral dimension to a distance of 150 points, resulting in a 150 by 150 array of QCT density values (outer contour, Fig. 1c). During this geometric manipulation, the locations of the cortical peaks were tracked. The square array representing each bone slice was then re-interpolated in two dimensions such that the cortical peaks were located at the same positions for each slice (inner contour, Fig. 1c).

The geometry-adjusted density distributions for each slice were then averaged (point by point) within each group to determine a 'typical' three-dimensional density distribution for that slice that was representative of the group's BMD level (Fig. 1d). The coefficient of variation in density was also calculated at each point in the distribution to quantify the similarity in density distribution within each group. Once a 'typical' density distribution was established for each slice and BMD level, the density distribution for any BMD level could be predicted by interpolating between the averaged levels (Fig. 1e). The described method, therefore, led to the development of a relationship between BMD level and three-dimensional density distribution. The predicted density distributions could then be mapped to any available femur geometry, using the reverse of the scaling algorithm described above (Fig. 1f).

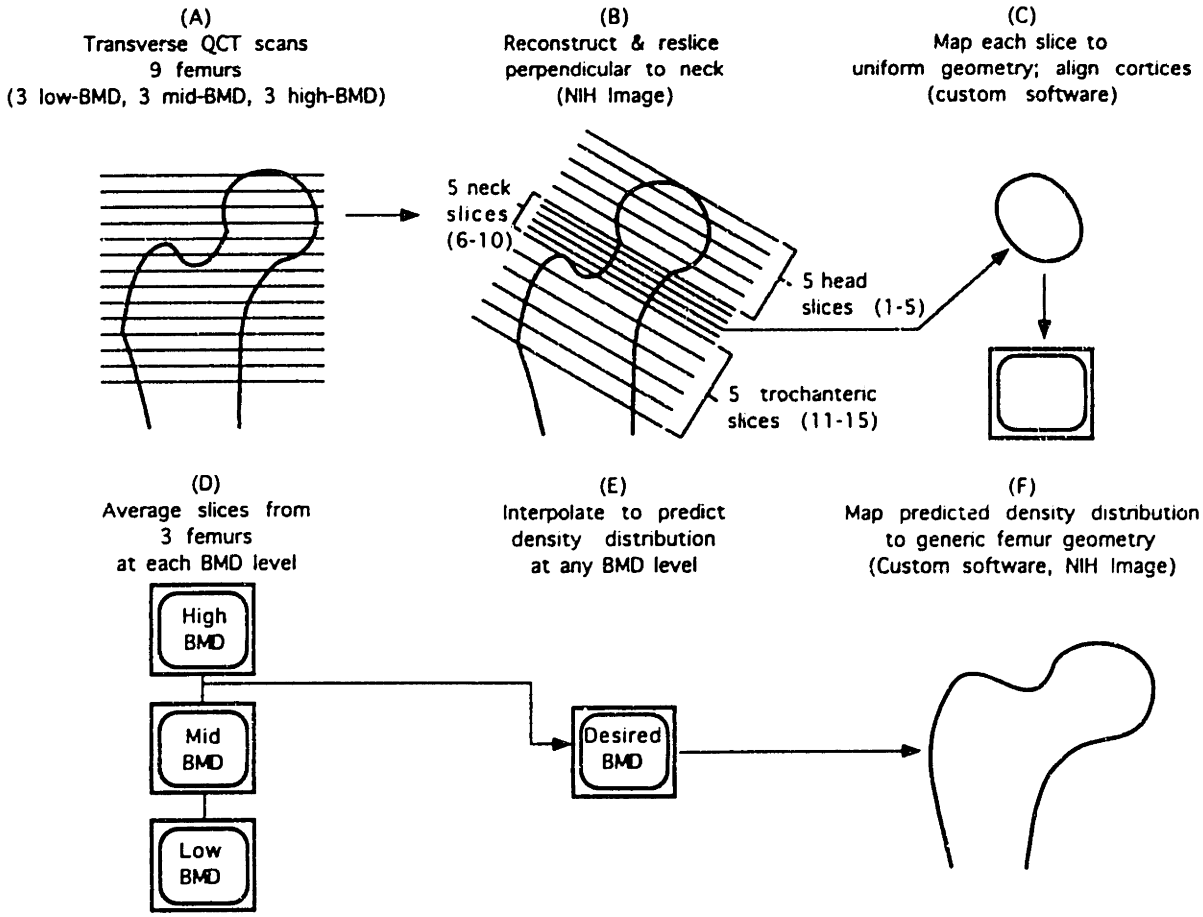

Figure 1: Flow chart describing the geometric scaling algorithm used to determine a relationship between BMD level and three-dimensional density distribution. (A) Nine proximal femurs were scanned transversely using QCT, with contiguous 3 mm slices from the superior aspect of the femoral head to below the lesser trochanter. (B) A stack of frontal images was created from the transverse scans, and resliced perpendicular to the femoral neck. (C) Each slice was then mapped to a constant geometry (outer boundary), and reinterpolated in two dimensions such that the cortial peaks were in the same position for each slice (inner boundary). (D) Geometry-adjusted density distributions for each slice were averaged (point by point) within each group. (E) For each slice, the density distribution for any BMD level could be predicted by interpolating between the averaged levels. (F) The predicted density distribution could then be mapped to any available femur geometry using the reverse of the scaling algorithm described in steps A through C.

To determine the predictive ability of the relationship between BMD level and three-dimensional density distribution, two femurs were chosen from our femur DXA database whose BMD levels were a maximum distance from the averaged BMD levels used in the derivation. One femur was chosen whose regional BMD values were between the high and medium averaged levels, and one whose regional BMD values were between the medium and low levels (Table 3). Femurs were chosen in this manner to provide the most rigorous test of the derived relationship. First, the (geometry-independent) three-dimensional density distributions of these two femurs were predicted, using only their regional BMD values and the derived relationship between BMD and three-dimensional density distribution. Then, the geometric scaling algorithm described previously was applied to the actual QCT data (which were smoothed once to remove noise), and the predicted density distribution was compared to the actual density distribution. To quantify the error in the predictions, we calculated the percentage difference in density, point by point, between the predicted and the actual densities for each slice.

ID	Age	Sex	femoral neck BMD ($g\ cm^{-2}$)	trochanteric BMD ($g\ cm^{-2}$)	intertrochanteric BMD ($g\ cm^{-2}$)
1244	49	M	0.761	0.534	1.113
1298	82	F	0.505	0.505	0.832

Table 3: Regional BMD values, age and sex of femurs used for validation of the relationship between BMD level and three-dimensional density distribution

6.2.2 Determination of Patterns of Age-Related Bone Loss

Using the derived relationship between BMD level and three-dimensional density distribution, density distributions were predicted for three BMD levels representing young normal, osteopenic, and osteoporotic women, based on the World Health Organization

(WHO) diagnostic criteria for osteoporosis and osteopenia (Kanis *et al.*, 1994). The WHO diagnostic approach defines osteopenia as a BMD that is between 1 and 2.5 standard deviations below the young adult mean value, and osteoporosis as a BMD that is more than 2.5 standard deviations below the young adult level. The three BMD levels examined in this study (Table 4) were chosen based on data from Looker *et al.* (1995), who measured BMD levels of U.S. women as part of the third National Health and Nutrition Examination Survey.

Diagnostic category	femoral neck BMD ($g\ cm^{-2}$)	trochanteric BMD ($g\ cm^{-2}$)	intertrochanteric BMD ($g\ cm^{-2}$)
Normal	0.849	0.703	1.086
Osteopenic	0.659	0.546	0.864
Osteoporotic	0.511	0.424	0.688

Table 4: Regional BMD values used to represent normal, osteopenic, and osteoporotic diagnostic levels. Diagnostic categories are as defined by an expert panel of the World Health Organization (Kanis *et al.*, 1994); BMD levels are based on data reported by Looker *et al.* (1995)

For ease of viewing results, each of the (geometry-independent) predicted density distributions was mapped to the same generic femur geometry, using the reverse of the geometric scaling algorithm described previously (Fig. 1f). The density loss between the normal and osteopenic levels and between the osteopenic and osteoporotic levels was assessed at each point in the femur by calculating the percent difference between the predicted density distributions at each BMD level.

6.3 Results

6.3.1 Relationship between DXA measurements and three-dimensional density distribution

Once inter-bone differences in geometry were accounted for, femurs within each group (high-BMD, medium-BMD, and low-BMD) had similar three-dimensional density distributions. The mean coefficients of variation in density for a slice through the mid-neck (slice 8, Fig. 1b) in the high-BMD, medium-BMD, and low-BMD groups were 6.9%, 7.4%, and 4.6%, respectively, demonstrating that the variability in QCT density between femurs within each group was reasonably small (Fig. 2). The coefficients of variation for a slice through the mid-trochanteric region (slice 13, Fig. 1b) were similarly small, with means of 6.4%, 7.9%, and 6.2% in the high-BMD, mid-BMD and low-BMD groups, respectively (Fig. 3). The coefficients of variation in QCT density for all other slices were similar in magnitude and distribution to those for the mid-neck and trochanteric slices (Table 5), demonstrating that, on average, the variability in QCT density within each group was of the same order as the variability in BMD. In addition, remarkable similarities in the shapes of the density distributions of femurs within each BMD group were noted upon visual inspection of the geometry-adjusted slices (Fig. 4).

The three-dimensional density distributions predicted from the BMD levels of two femurs using our derived relationship compared favorably with the actual density distributions measured by QCT. For the first femur (BMD between the high-BMD and medium-BMD averaged levels), the mean percent difference between the actual and predicted density distributions ranged from -5.3% - 2.3%, for five slices sampled from the proximal region (Fig. 5). For these five slices, the minimum and maximum percent errors were -26.5% (occurring in the trochanteric slice) and 49.3% (occurring in the subcapital slice), respectively (Table 6). Absolute errors greater than 10% occurred for only 6.7% of

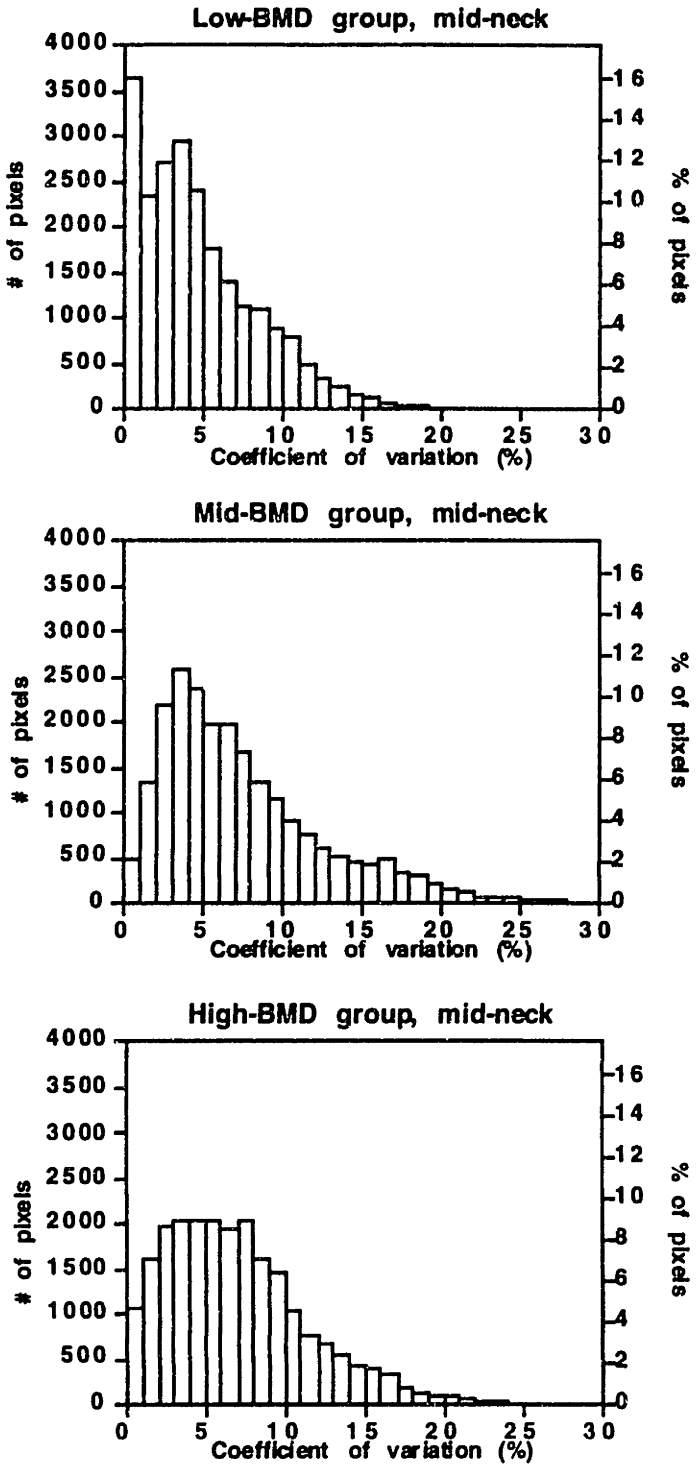

Figure 2: Histograms showing the frequency distribution of coefficients of variation for a (geometry-adjusted) slice through the mid-neck (slice 8, Fig. 1b), for the low-BMD, mid-BMD, and high-BMD groups. Only 5.7%, 9.8%, and 0.9% of pixels in the low-BMD, mid-BMD, and high-BMD groups, respectively, had coefficients of variation greater than 15%.

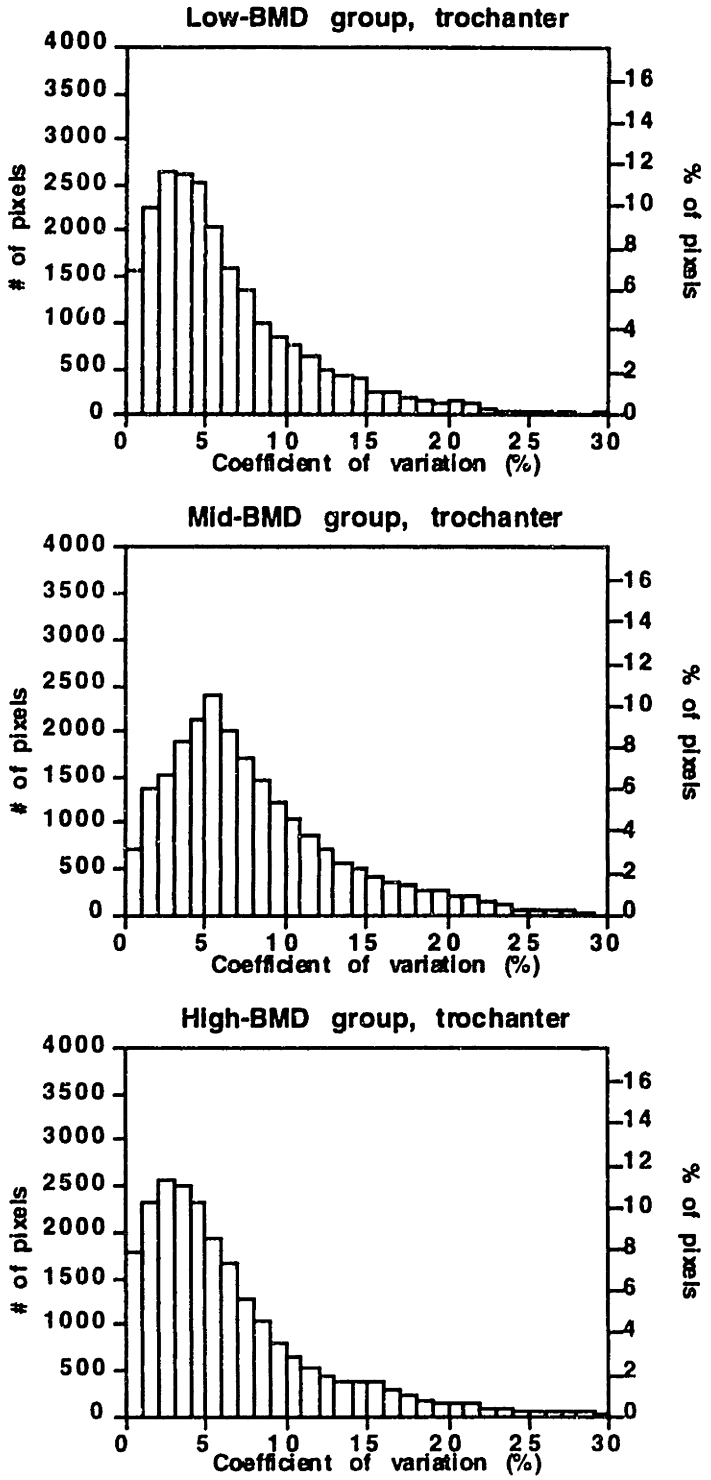

Figure 3: Histograms showing the frequency distribution of coefficients of variation for a (geometry-adjusted) slice through the trochanteric region (slice 13, Fig. 1b), for the low-BMD, mid-BMD, and high-BMD groups. Only 6.4%, 10.9%, and 8.8% of pixels in the low-BMD, mid-BMD, and high-BMD groups, respectively, had coefficients of variation greater than 15%.

Slice	Mean cov (max) low-BMD group (%)	Mean cov (max) mid-BMD group (%)	Mean cov (max) high-BMD group (%)
1	4.0 (11.3)	6.6 (19.4)	5.0 (16.2)
2	3.6 (12.3)	6.8 (16.3)	6.3 (24.2)
3	3.8 (12.9)	4.8 (17.8)	4.7 (13.6)
4	2.8 (13.8)	4.6 (18.8)	6.2 (18.4)
5	4.0 (17.8)	5.1 (22.7)	6.3 (23.0)
6	5.1 (23.9)	7.2 (27.9)	7.4 (30.3)
7	4.8 (20.7)	7.5 (29.2)	7.0 (28.9)
8	4.6 (19.0)	7.4 (28.7)	6.9 (25.6)
9	5.0 (18.4)	7.7 (31.5)	7.6 (26.3)
10	5.5 (23.7)	7.5 (34.4)	8.5 (31.9)
11	5.2 (22.2)	7.0 (28.7)	8.0 (29.0)
12	6.0 (34.8)	7.4 (29.0)	6.5 (42.0)
13	6.2 (32.0)	7.9 (31.7)	6.4 (35.3)
14	5.2 (35.2)	8.7 (33.9)	6.0 (33.7)
15	5.1 (34.0)	7.7 (35.8)	7.2 (35.0)

Table 5: Mean and maximum coefficients of variation (%) for each of 15 slices (see Fig. 1b) for the low, mid, and high-BMD groups

pixels in the five slices sampled (Fig. 6). Analysis of the predicted and actual density distributions for the second femur (BMD between the mid-BMD and low-BMD groups) revealed similarly low errors. In addition to the results of the quantitative error analysis, plots of each of the five slices visually demonstrate the excellent agreement between the predicted and actual density distributions (Fig. 7). It was concluded from these comparisons between predicted and actual density distributions that the derived relationship was effective in predicting the essential features of a femur's three-dimensional density distribution given only its regional BMD levels.

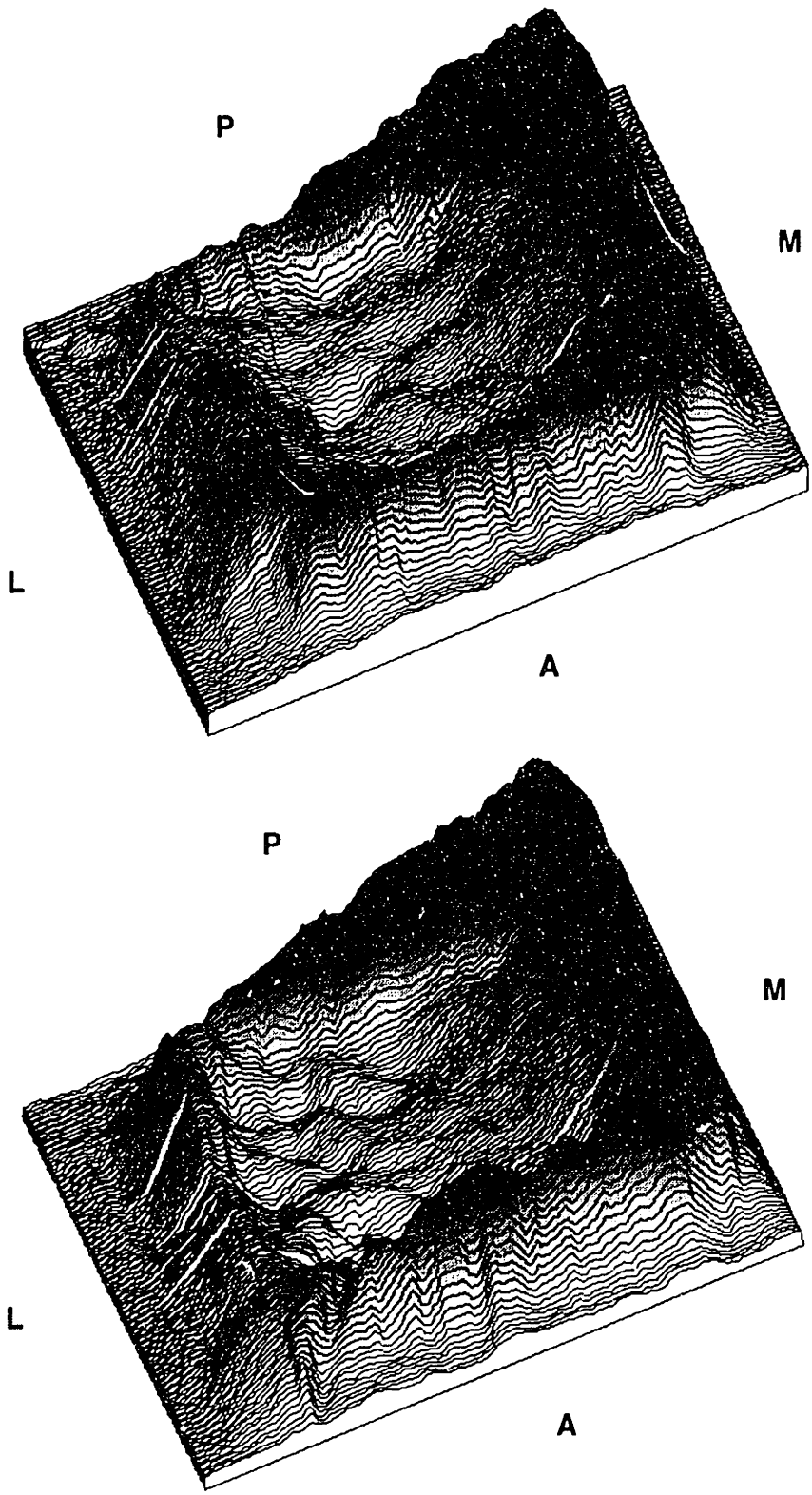

Figure 4: Geometry-adjusted density distributions at the mid-neck for two femurs from the high-BMD group. The height at each point is proportional to the density. A, anterior; P, posterior; M, medial; L, lateral. The density distributions are similar for the two femurs.

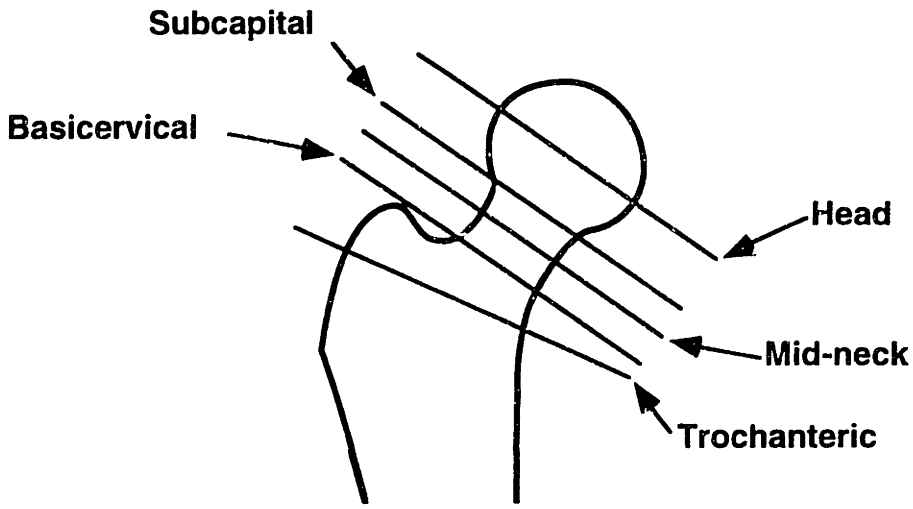

Figure 5: Locations of slices (one pixel thick) used for calculating the percent error between actual and predicted density distributions.

Slice	mean % error ± S.D.	minimum % error	maximum % error
head	-5.3 ± 4.6	-15.0	12.5
subcapital	2.3 ± 11.1	-22.1	49.3
midneck	-0.9 ± 7.3	-27.9	18.9
basicervical	-0.8 ± 5.6	-24.8	20.3
trochanteric	-0.8 ± 8.6	-26.5	32.8

Table 6: Percent errors between actual and predicted density distributions for femur with BMD between high-BMD and mid-BMD groups, for five slices through the proximal region.

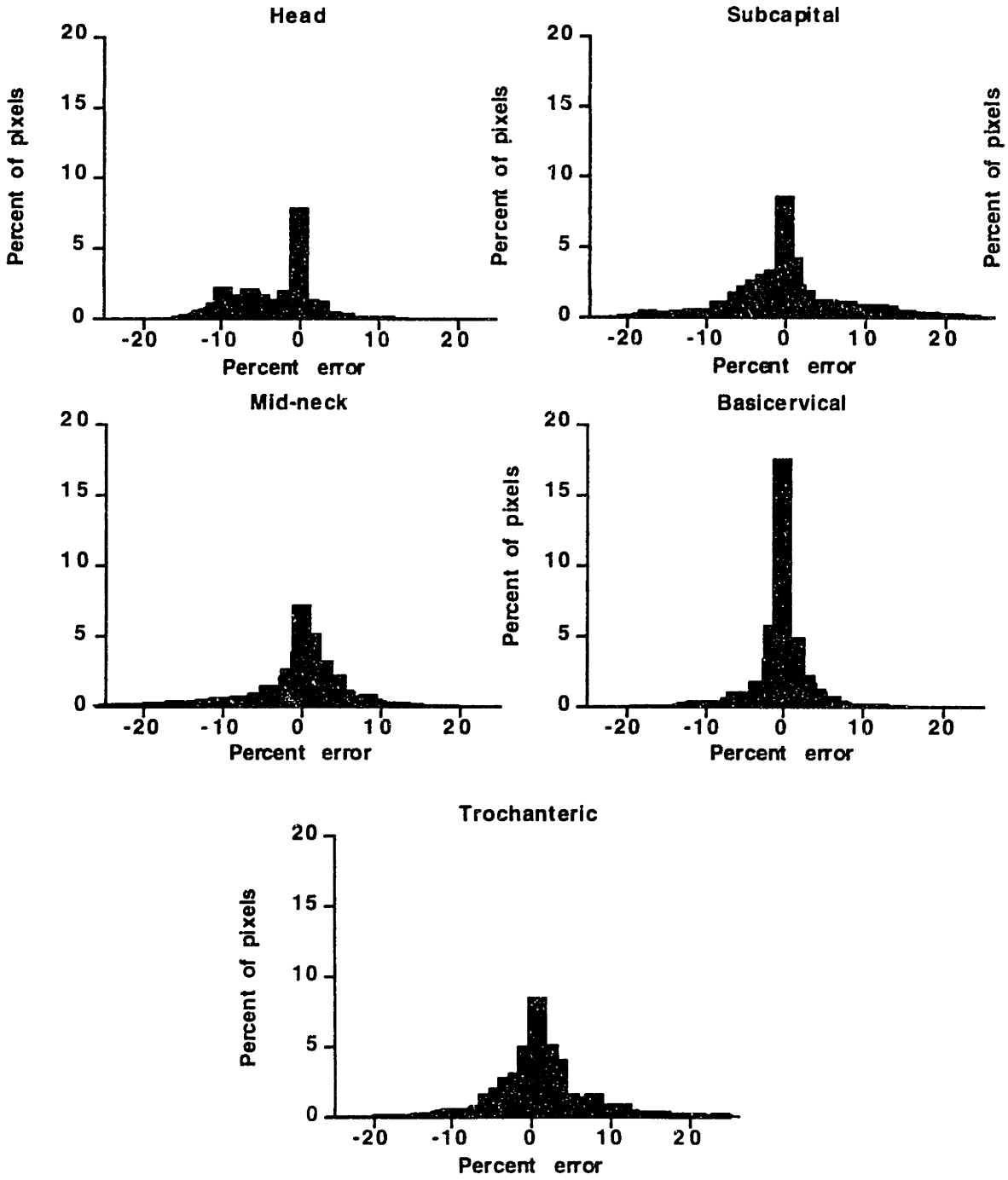

Figure 6: Histograms showing frequency distribution of percent error between actual and predicted density distributions, for five slices. The mean percent errors ranged from -5.3% (at the femoral head) to 2.3% (at the subcapital slice). Absolute errors greater than 10% occurred for only 6.7% of the pixels in the five slices sampled.

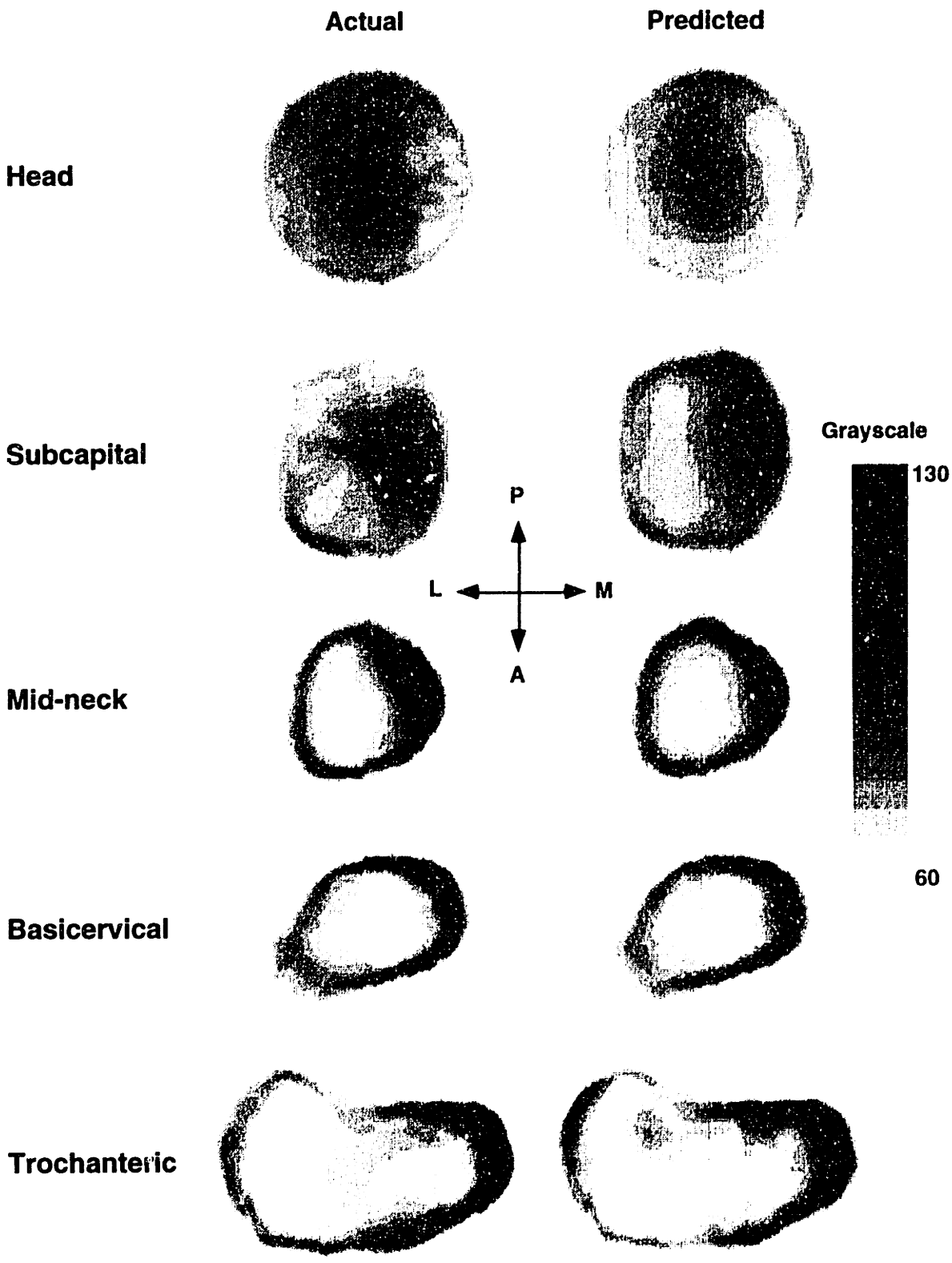

Figure 7: Plots of density distributions for five proximal slices, showing good agreement between actual (left) and predicted (right) distributions.

6.3.2 Patterns of Age-Related Bone Loss

The calculated reductions in QCT density depended strongly on both baseline BMD level and anatomic site. Between the normal and osteopenic BMD levels (representing a loss in BMD of about 22% in the femoral neck, trochanteric, and intertrochanteric regions), reductions in QCT density at the five proximal slices sampled ranged from 0% - 23%, depending upon anatomic location (Fig. 8, Table 7). The peak density reduction occurred at the posterior mid-neck. For a slice through the center of the femoral head, reductions in density were higher anteriorly than posteriorly. At the subcapital site, density reductions were highest near the center of the slice, and were lower medially than laterally. At the mid-neck, there were relatively high losses near the posterior and anterolateral cortices and in trabecular bone on the medial side, with almost no density loss occurring in the area of the medial cortex. As in the mid-neck, there were high losses in the posterior cortex at the basicervical slice. In the mid-trochanteric region, density reductions were highest posteromedially and lowest posterolaterally.

Reductions in density between the osteopenic and osteoporotic BMD levels (representing a loss in BMD of about 22% in the femoral neck, trochanteric, and intertrochanteric regions) also depended on anatomic site within the femur (Fig. 9, Table 8). The peak reduction in density occurred at the posterior aspect of the trochanteric slice. At the center of the femoral head, density reductions were fairly uniform except for relatively low losses anteromedially. Reductions at the subcapital site were also fairly uniform. At the midneck, basicervical and trochanteric slices, losses were on average higher medially than laterally.

The density reductions observed between the osteopenic and osteoporotic BMD levels had different distributions than the losses observed between the normal and osteopenic levels (Fig. 10). At the center of the femoral head, bone loss was *highest* anteriorly between the normal and osteopenic levels, while bone loss was *lowest* anteriorly

between the osteopenic and osteoporotic BMD levels. While losses at the subcapital site were essentially *uniform* between the osteopenic and osteoporotic levels, losses were highly *non-uniform* between the normal and osteopenic levels. At the mid-neck, losses in the medial cortex were higher between the osteopenic and osteoporotic levels than between the normal and osteopenic levels, but losses in the posterior and lateral cortices were higher between the normal and osteopenic levels than between the osteopenic and osteoporotic levels. Basicervically, relatively high losses were observed posteriorly and laterally between the normal and osteopenic levels, but were highest medially and anteriorly between the osteopenic and osteoporotic levels. At the trochanteric site, reductions were highest medially between both the normal and osteopenic and between osteopenic and osteoporotic levels.

In addition to the differences in the spatial distributions of bone loss, reductions in density were, on average, of a higher magnitude between the normal and osteopenic levels than they were between the osteopenic and osteoporotic levels (Tables 7, 8). The mean reductions in density for each slice (ranging from 5.5% - 7.0 % between the normal and osteopenic BMD levels and from 4.0% - 5.3% between the osteopenic and osteoporotic BMD levels) were also substantially lower than the BMD differences of about 22% that were used to define the normal, osteopenic and osteoporotic levels. In fact, for the five slices sampled, fewer than 1% of pixels had density reductions greater than or equal to 22% between the normal and osteopenic levels (Fig. 11), and no pixels had density reductions greater than or equal to 22% between the osteopenic and osteoporotic levels (Fig. 12).

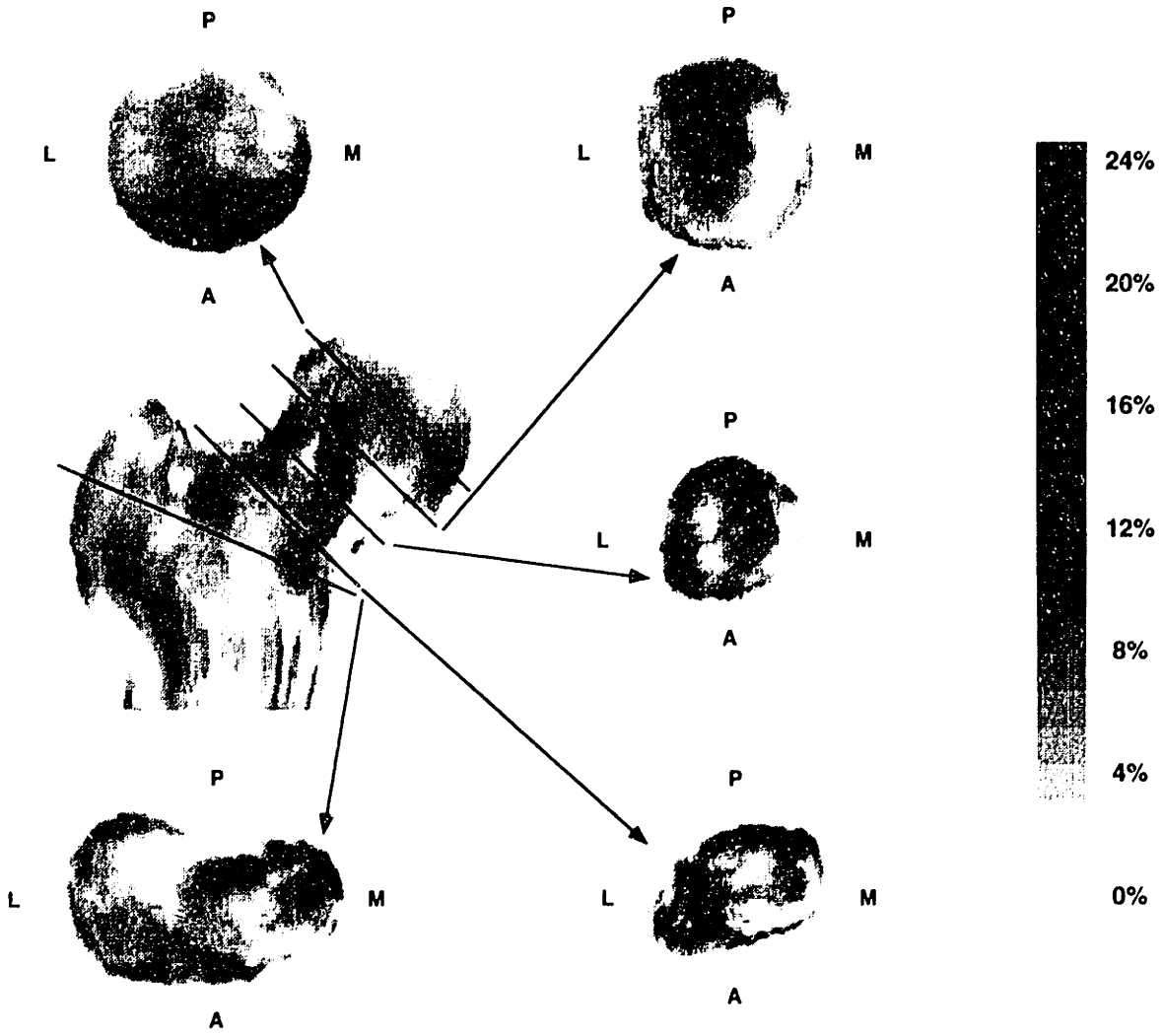

Figure 8: Reductions in QCT density (%) between the normal and osteopenic BMD levels, for five proximal slices. The peak density reduction of 24% occurred at the posterior aspect of the mid-neck slice. Density reductions depended strongly on anatomic location.

Slice	Density reduction mean ± SD (%)	Minimum density reduction (%)	Maximum density reduction (%)
Head	6.3 ± 4.3	0	17
Subcapital	6.2 ± 4.4	0	17
Mid-neck	7.0 ± 5.3	0	22
Basicervical	6.4 ± 4.7	0	23
trochanteric	5.5 ± 3.7	0	19

Table 7: Mean, minimum, and maximum density reductions (%) between the normal and osteopenic BMD levels, for five proximal slices

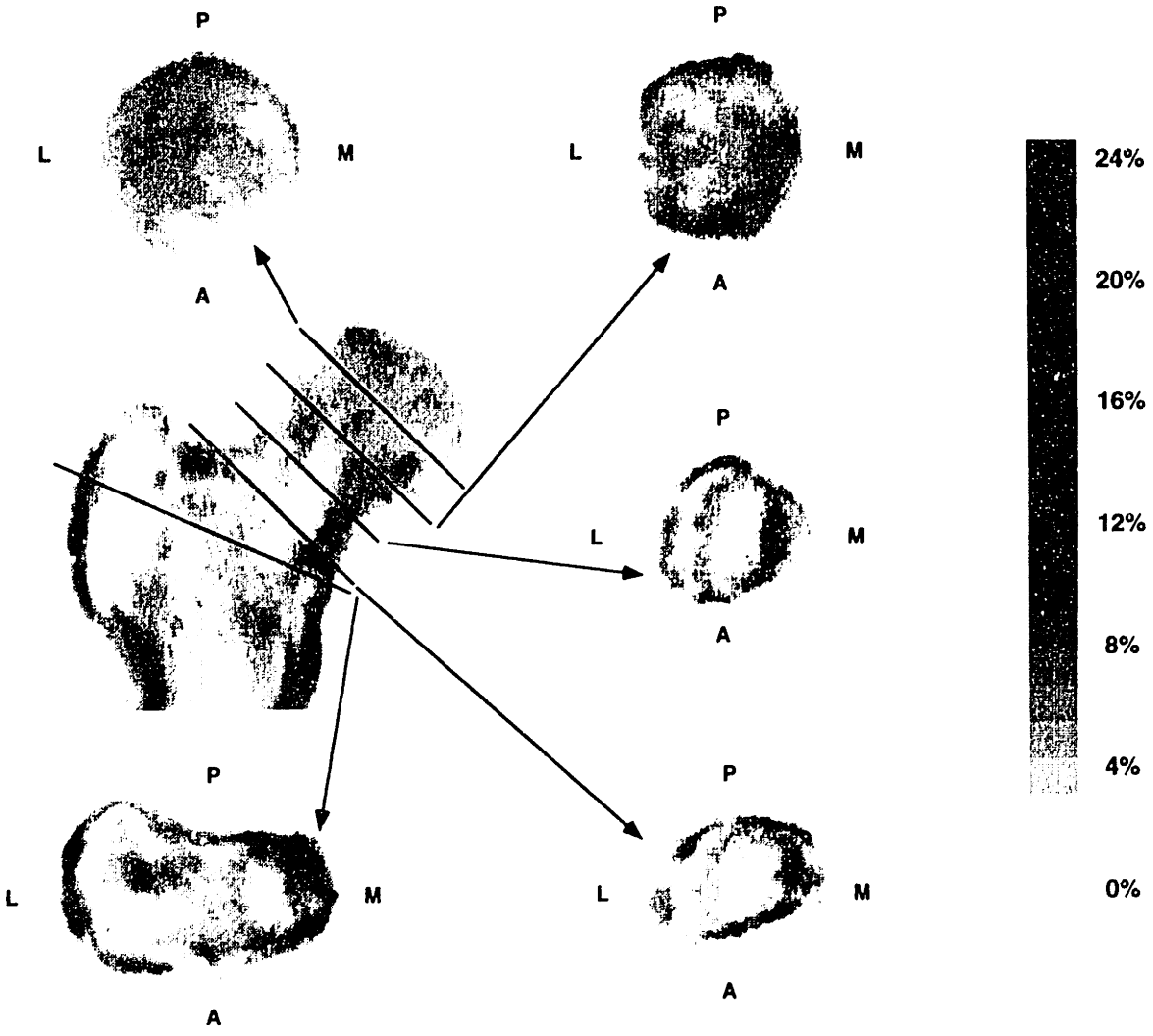

Figure 9: Reductions in QCT density (%) between the osteopenic and osteoporotic BMD levels, for five proximal slices. The peak density reduction of 19% occurred at the posterior aspect of the trochanteric slice. Density reductions depended strongly on anatomic location.

Slice	Density reduction mean ± SD (%)	Minimum density reduction (%)	Maximum density reduction (%)
Head	4.2 ± 2.3	0	9
Subcapital	5.3 ± 2.9	0	13
Mid-neck	4.3 ± 2.9	0	15
Basicervical	4.0 ± 3.2	0	16
trochanteric	4.5 ± 3.4	0	19

Table 8: Mean, minimum, and maximum density reductions (%) between the osteopenic and osteoporotic BMD levels, for five proximal slices

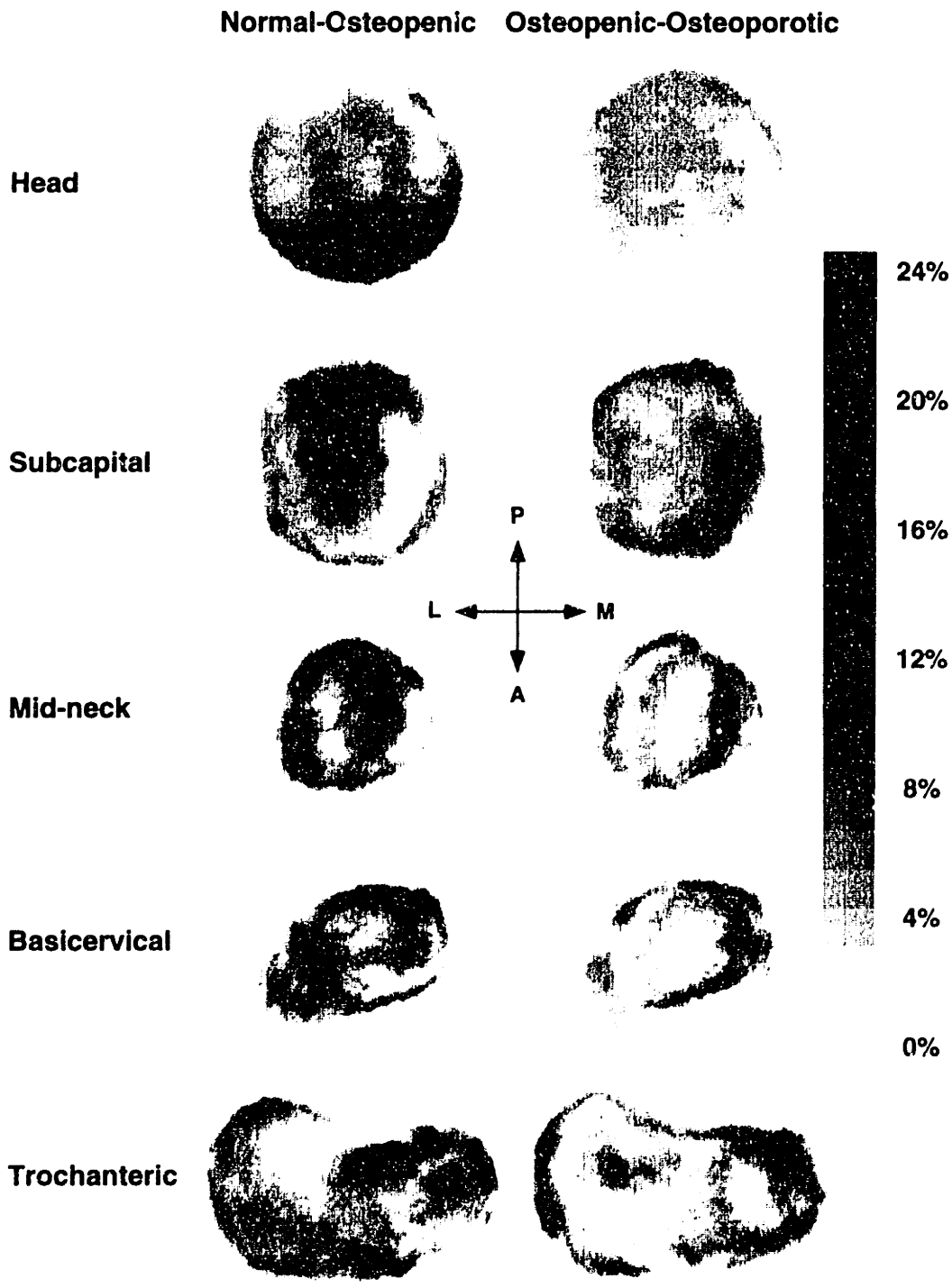

Figure 10: Comparison of density reductions (%) between the normal and osteopenic levels (left) and between the osteopenic and osteoporotic BMD levels (right). Patterns of bone loss were substantially different for the two BMD steps, and were on average higher between the normal and osteopenic levels than between the osteopenic and osteoporotic levels.

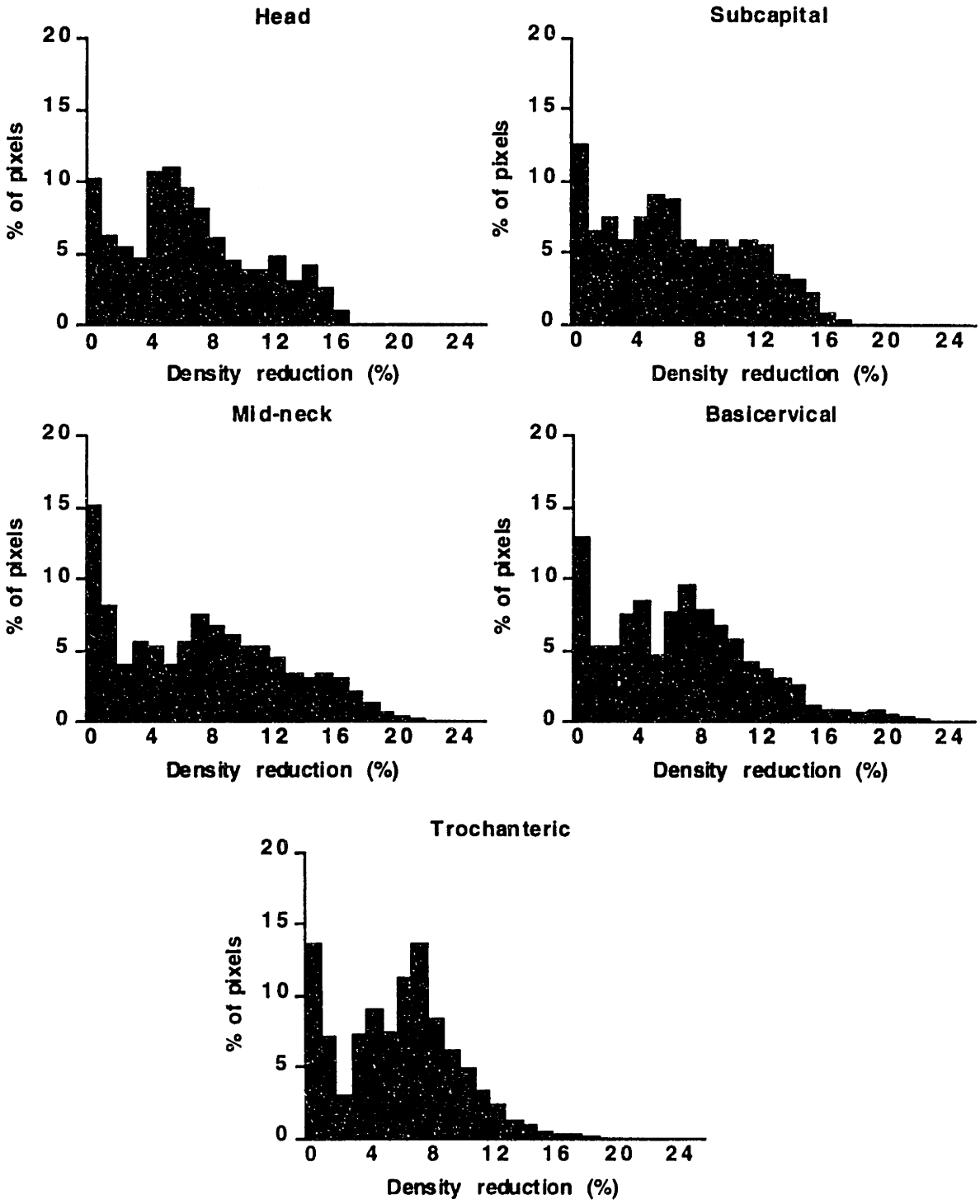

Figure 11: Histograms showing frequency distribution of density reductions between the normal and osteopenic BMD levels, for five proximal slices.

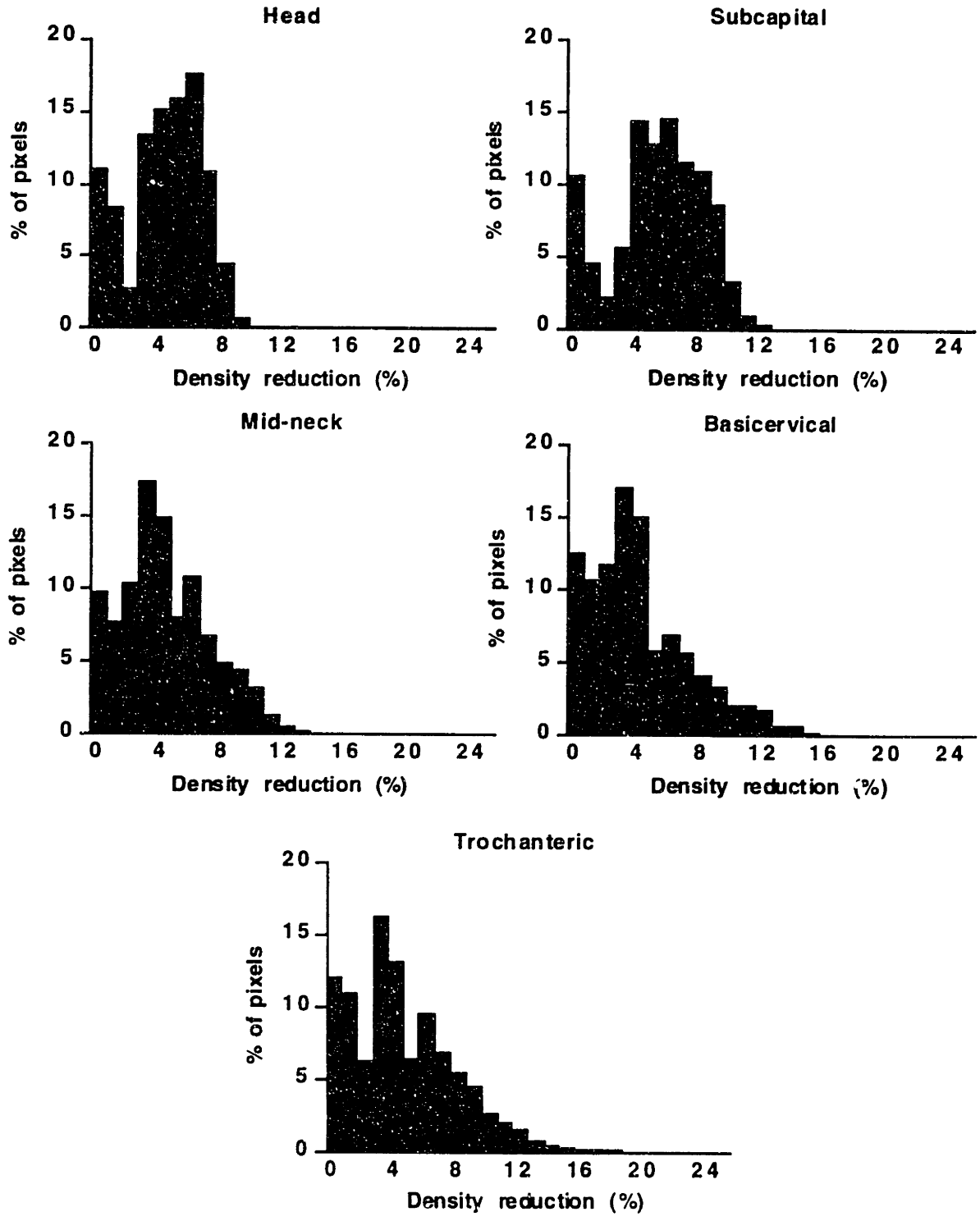

Figure 12: Histograms showing frequency distribution of density reductions between the osteopenic and osteoporotic BMD levels, for five proximal slices.

6.4 Discussion

The objectives of this study were twofold. The first objective was to apply a custom geometric scaling algorithm to QCT data from three groups of cadaveric femurs (low-BMD, mid-BMD, and high-BMD) to derive a relationship between BMD (a two-dimensional density measurement) and three-dimensional density distribution. We demonstrated that the derived relationship was effective in predicting the three-dimensional density distribution of a femur given only its regional BMD values. The second objective was to predict the three-dimensional density distributions associated with BMD levels defined as normal, osteopenic, and osteoporotic by an expert panel of the World Health Organization (Kanis *et al.*, 1994), and to use these predictions to examine (cross-sectionally) three-dimensional patterns of age-related bone loss. The results showed that bone loss that appeared 'uniform' based on clinical DXA exams was in fact the result of density reductions that were highly non-uniform when viewed in three dimensions. Both the patterns and magnitudes of bone loss observed between the normal and osteopenic BMD levels were substantially different from those observed between the osteopenic and osteoporotic levels, despite the fact that the BMD reductions used to define the levels were equal. Lastly, the mean QCT density reductions between normal and osteopenic and between osteopenic and osteoporotic levels were only about 20-30% as large as the BMD reductions defining the levels.

Although the results of this study represent a significant step in our understanding of bone loss patterns in the proximal femur, some limitations of the analysis deserve attention. First, the thinness of the cortical shell, combined with the volume averaging phenomenon present in the QCT data, makes measurement of cortical shell density with QCT extremely difficult. Since the voxel size of the QCT datasets used here (approximately 0.5 mm) was of the same order as the thickness of the cortical shell in some regions (Lotz *et al.*, 1991), and since the geometric scaling technique filtered out components of the QCT

density distribution with very high spatial frequencies, it was not possible to assess changes in cortical shell properties accurately with this analysis. However, the error analysis did demonstrate that most of the essential features of the desired density distribution could be predicted using the derived relationship. A combination of higher resolution QCT data and performance of the scaling algorithm at a higher resolution may allow for measurement of changes in cortical shell density in the future. Second, the relatively small sample size used in this analysis (three femurs per group) may limit extrapolation of the results to the general population. The femurs used in this analysis were chosen based on similarities in their regional BMD levels (Table 2). The inclusion of additional femurs from the available database in any of the groups would have substantially increased the variability in BMD (and therefore variability in true density) within each group. Since the relationship derived in this study (based on the analysis of only nine femurs) was reasonably successful in predicting three-dimensional density distributions, the inclusion of additional femurs and BMD levels in the analysis would likely result in even better predictions of three-dimensional density distribution. In addition to attempting to minimize the coefficients of variation in BMD within each group, an attempt was made to limit the analysis to femurs from female donors (those with the highest incidence of hip fracture), so that the potentially confounding effect of differences in density between men and women could be minimized. To achieve a sample size of three femurs in each group, we did include one femur from a male donor (in the high-BMD group). However, the fact that the coefficients of variation in density for the high-BMD group were similar to those for the mid-BMD and low-BMD groups (Table 5) suggests that the inclusion of a femur from a male donor did not significantly affect the analysis. This argument is also supported by the fact that the derived relationship between BMD and three-dimensional density distribution was effective in predicting the density distribution of a femur from a male donor.

In addition to gender, there are several other factors that can influence skeletal status and therefore may have confounded the results of this study. For example, if an individual is subjected to prolonged bed rest, his or her femoral density distribution may be different from that of an ambulatory individual with the same BMD. In addition, it may be that elderly and young individuals with the same BMD have different three-dimensional density distributions, or that individuals undergoing estrogen or glucocorticoid therapy have different density distributions than unmedicated individuals with the same BMD. Since complete medical records were not available for the donors used in this study, it was not possible to assess the contributions of these and other factors (such as menopausal status and disease) directly. The presence of any one of these factors in the donor population studied could have affected both the average density distributions determined for each group, as well as within-group variability. However, the confounding effects of these factors were probably smaller than the changes observed between the normal, osteopenic, and osteoporotic BMD levels, which were changes associated with relatively large variations in BMD. Although not critical to this study, the geometric scaling algorithm developed here could be used to study the differences in density distribution associated with any factor affecting skeletal status, provided these factors could be well-controlled in the study population.

The scaling algorithm developed in this study for QCT data allowed for elimination of the confounding influence of inter-bone differences in geometry, and therefore provided the first direct, quantitative and geometry-independent comparison of three-dimensional density distributions between bones. Once geometric influences were eliminated, mean reductions in true density were only about 20-30% as large as reductions in areal BMD. This result implies that differences in cross-sectional femoral geometry, rather than true density differences, may in fact be responsible for a portion of the variability in BMD that is observed within the population. This finding is consistent with the high correlations that exist between geometric parameters (such as femoral neck cross sectional area) and BMD

measurements (Beck *et al.*, 1990), and is also consistent with previous findings for the lumbar spine, where investigators demonstrated that areal BMD measurements depend on subject height (Carter *et al.*, 1992). The current study adds to our understanding of the relative importance of geometry and density by directly quantifying how much of the variability in BMD across the analyzed population (less than one-third) is due to true density reductions.

In addition to suggesting that differences in cross-sectional geometry are responsible for a relatively large portion of the variability in BMD within the population, the results suggest that the relative contributions of cross-sectional geometry and density may differ depending on BMD level. We showed that the true density differences present between the normal and osteopenic BMD levels were on average larger than the density differences present between the osteopenic and osteoporotic BMD levels (Tables 7, 8), even though the BMD reductions defining the levels were equal for each step. This result implies that cross-sectional geometry may play a more important role at lower BMD levels than at higher BMD levels in determining BMD variability within the population. Since the majority of hip fractures occur in individuals with low BMD, this result points to the need for better information about how geometric parameters affect the structural capacity of the femur and therefore the risk of hip fracture.

The results of this study may have implications for the longitudinal assessment of hip fracture risk in individuals. True density reductions between the normal and osteopenic and between the osteopenic and osteoporotic BMD levels were substantially smaller than the BMD reductions used to define the levels, suggesting that differences in cross-sectional femoral geometry are primarily responsible for the variations in BMD observed in the studied femur population, and probably also in other clinical and cadaveric study populations. The dominant effect of geometric parameters in a cross-sectional analysis is not surprising, given the tremendous variations in femoral geometry that are present across the population. In an individual, however, the relative contribution of geometric remodeling

to longitudinal changes in BMD is probably not as dramatic, since an individual is unlikely to experience the broad range of anatomic variations that are present across a population. Therefore, the trends in femoral strength observed as a function of BMD in cross-sectional fracture studies (Weber *et al.*, 1992; Courtney *et al.*, 1994; Courtney *et al.*, 1995; Pinilla *et al.*, 1996) may not reflect the changes in strength associated with longitudinal reductions in BMD in an individual. In addition, it may be that the relative contributions of geometric and density changes to reductions in BMD are different for different individuals (as they probably are for men and women [Beck *et al.*, 1992]), further complicating the relationship between BMD and fracture risk. Therefore, accurate assessment of changes in an individual's fracture risk over time may depend on determining the independent contributions of bone density and geometry to the structural capacity of the femur.

6.5 References

Aloia J., McGowan D., Erens E., and Miele G. (1992) Hip fracture patients have generalized osteopenia with a preferential deficit in the femur. *Osteoporosis Int* **2**, 88-93.

Beck T., Ruff C., Scott W., Plato C., Tobin J., and Quan C. (1992) Sex differences in geometry of the femoral neck with agina: A structural analysis of bone mineral data. *Calcif Tissue Int* **50**, 24-29.

Beck T. J., Ruff C. B., Warden K. E., Scott W. W., and Rao G. U. (1990) Predicting femoral neck strength from bone mineral data: A structural approach. *Invest Radiol* **25**, 6-18.

Carter D., Bouxsein M., and Marcus R. (1992) New approaches for interpreting projected bone densitometry data. *J Bone Min Res* **7**, 137-145.

Carter D. R. and Hayes W. C. (1976) Bone compressive strength: the influence of density and strain rate. *Science* **194**, 1174-1176.

Courtney A. C., Wachtel E. F., Myers E. R., and Hayes W. C. (1994) Effects of loading rate on strength of the proximal femur. *Calcif Tissue Int* **55**, 53-58.

Courtney A. C., Wachtel E. F., Myers E. R., and Hayes W. C. (1995) Age-related reductions in the strength of the femur tested in a fall loading configuration. *J Bone Joint Surg [Am]* **77**, 387-395.

Cummings S., Nevitt M., Browner W., Stone K., Fox K., Ensrud K., Cauley J., Black D., and Vogt T. (1995) Risk factors for hip fracture in white women. *N Engl J Med* **332**, 767-773.

Cummings S. R., Black D. M., and Nevitt M. C. (1990) Appendicular bone density and age predict hip fracture in women. *JAMA* **263**, 665-668.

Cummings S. R., Black D. M., Nevitt M. C., Browner W., Cauley J., Ensrud K., Genant H. K., Palermo L., Scott J., and Vogt T. M. (1993) Bone density at various sites for prediction of hip fractures. *Lancet* **341**, 72-75.

Elliot J. R., Gilchrist N. L., Wells J. E., Turner J. G., Ayling E., Gillespie W. J., Sainsbury R., Hornblow A., and Donald R. A. (1990) Effects of age and sex on bone density at the hip and spine in a normal caucasian New Zealand population. *NZ Med J* **103**, 33-36.

Greenspan S., Maitland L., Myers E., Krasnow M., and Kido T. (1994a) Femoral bone loss progresses with age: A longitudinal study in women over age 65. *J Bone Min Res* **9**, 1959-1965.

Greenspan S. L., Myers E. R., Maitland L. A., Resnick N. M., and Hayes W. C. (1994b) Fall severity and bone mineral density as risk factors for hip fracture in ambulatory elderly. *JAMA* **271**, 128-133.

Hannan M., Felson D., and Anderson J. (1992) Bone mineral density in elderly men and women: Results from the Framingham Osteoporosis Study. *J Bone Min Res* **7**, 547-553.

Harris S. and Dawson-Hughes B. (1992) Rates of change in bone mineral density of the spine, heel, femoral neck and radius in healthy postmenopausal women. *Bone and Mineral* **17**, 87-95.

Kanis J. A., Melton L. J., Christiansen C., Johnston C. C., and Khaltaev N. (1994) The diagnosis of osteoporosis. *J Bone Min Res* **9**, 1137-1141.

Kawashima T. and Uhthoff H. K. (1991) Pattern of bone loss of the proximal femur: a radiologic, densitometric, and histomorphometric study. *J Orthop Res* **9**, 634-640.

Looker A., Johnston C., Wahner H., Dunn W., Calvo M., Harris T., Heyse S., and Lindsay R. (1995) Prevalence of low femoral bone density in older U.S. women from NHANES III. *J Bone Min Res* **10**, 796-802.

Lotz J., Gerhart T., and Hayes W. (1991) Mechanical properties of metaphyseal bone in the proximal femur. *J Biomech* **24**, 317-329.

Mazess R., Barden H., Ettinger B., and Schultz E. (1988) Bone density of the radius, spine and proximal femur in osteoporosis. *J Bone Min Res* **3**, 13-18.

Mazess R. B. (1982) On aging bone loss. *Clin Orthop* **165**, 239-252.

Melton L., Atkinson E., O'Fallon W., Wahner H., and Riggs B. (1993) Long-term fracture prediction by bone mineral assessed at different skeletal sites. *J Bone Min Res* **8**, 1227-1233.

Nevitt M., Johnell O., Black D., Ensrud K., Genant H., and Cummings S. (1994) Bone mineral density predicts non-spine fractures in very elderly women. *Osteoporosis Int* **4**, 325-331.

Pinilla T., Boardman R., Bouxsein M., Myers E., and Hayes W. (1996) Impact direction from a fall influences the failure load of the femur as much as age-related bone loss. *Calcif Tissue Int* **58**, 231-235.

Rice J. C., Cowin S. C., and Bowman J. A. (1988) On the dependence of the elasticity and strength of cancellous bone on apparent density. *J Biomech* **21**, 155-168.

Riggs B., Wahner H., Dunn W., Mazess R., Offord K., and Melton L. (1981) Differential changes in bone mineral density of the appendicular and axial skeleton with aging. *J Clin Invest* **67**, 328-335.

Riggs B. L. and Melton L. J. (1986) Involutional osteoporosis. *New England J Med* **314**, 1676-1686.

Riggs B. L., Wahner H. W., Seeman E., Offord K. P., Dunn W. L., Mazess R. B., Johnson K. A., and Melton L. J. (1982) Changes in bone mineral density of the proximal femur and spine with aging. *J Clin Invest* **70**, 716-723.

Schaadt O. and Bohr H. (1988) Different trends of age-related diminution of bone mineral content in the lumbar spine, femoral neck, and femoral shaft in women. *Calcif Tissue Int* **42**, 71-76.

Singh M., Nagrath A., and Maini P. (1970) Changes in trabecular pattern of the upper end of the femur as an index of osteoporosis. *J Bone Joint Surg [Am]* **52**, 457-467.

Steiger P., Cummings S. R., Black D. M., Spencer N. E., and Genant H. K. (1992) Age-related decrements in bone mineral density in women over 65. *J Bone Miner Res* **7**, 625-632.

Wahner H. W. and Fogelman I. (1994) *The Evaluation of Osteoporosis: Dual Energy X-Ray Absorptiometry in Clinical Practice*, University Press, Cambridge, England.

Weber T. G., Yang K. H., Woo R., and Fitzgerald R. H. (1992) Proximal femur strength: Correlation of the rate of loading and bone mineral density. *ASME Adv in Bioengineering* **22**, 111-114.

Chapter 7

The Structural Consequences of Age-Related Bone Loss in the Proximal Femur

7.1 Introduction

Non-invasive densitometric techniques such as dual-energy x-ray absorptiometry and dual-photon absorptiometry have revolutionized the study and diagnosis of osteoporosis, because of the strong link between measures of bone mineral density (BMD) and age-related fracture risk. For example, prospective cohort studies have repeatedly demonstrated that BMD of the hip is a strong predictor of hip fracture (Cummings *et al.*, 1990; Cummings *et al.*, 1993; Melton *et al.*, 1993; Nevitt *et al.*, 1994; Cummings *et al.*, 1995), and laboratory investigations have revealed strong correlations between BMD and the structural capacity of the femur *ex vivo* (Weber *et al.*, 1992; Courtney *et al.*, 1994; Bouxsein *et al.*, 1995; Courtney *et al.*, 1995; Pinilla *et al.*, 1996). As a result of the impressive clinical and laboratory evidence linking BMD and hip fracture risk, measurements of BMD are now widely used as outcome variables in clinical trials of osteoporosis interventions, and have become the gold standard in the diagnosis of osteopenia and osteoporosis.

Although the existence of a connection between femoral BMD and hip fracture risk is indisputable, questions related to the mechanisms underlying this connection remain unanswered or only partly answered. For example, what is the relationship between a change in BMD for an individual and a change in structural capacity of the femur? Much of our understanding of this relationship comes from demonstrated correlations between BMD and the structural capacity of the femur *ex vivo* (Weber *et al.*, 1992; Courtney *et al.*, 1994; Bouxsein *et al.*, 1995; Courtney *et al.*, 1995; Pinilla *et al.*, 1996). Although these studies

have provided valuable insight into the relationship between BMD and femoral strength over a wide range of ages and loading rates, the reported relationships are subject to the potentially dramatic influence of confounding variables. For example, although the reported correlations between BMD (both at the femoral neck and total hip) and structural capacity of the femur are strong for loading rates representative of falls ($r^2 = 0.68 - 0.79$), femurs with nearly identical total BMD can have as much nearly a two-fold difference in structural capacity (Fig. 1). Conversely, femurs with nearly identical failure loads can have remarkably different total BMD values. Much of the scatter in BMD-failure load relationships can probably be explained by the confounding effects of inter-bone differences in geometry, as well as by inter-bone differences in regional BMD ratios (for example, the ratio of femoral neck to trochanteric BMD). As a result of these confounding factors (which cannot be controlled in an *ex vivo* study), relationships between BMD and failure load derived from *ex vivo* studies may not reflect the longitudinal changes in femoral strength that occur in an individual over time.

Age-related bone loss can occur at different rates in different regions of the proximal femur. In a recent longitudinal study of 85 elderly women, Greenspan *et al.* (1994a) found that the annual percent change in BMD of the femoral neck was not correlated at all ($r = 0.0$) with the annual percent change in BMD of the trochanteric region, and was only very weakly correlated with the annual percent changes at the intertrochanteric region ($r = 0.05$) and at the total hip ($r = 0.21$). It may be that bone loss in particular regions of the femur causes greater strength reductions than bone loss in other regions, however the independent effects of region-specific density changes on the load-bearing capacity of the femur have not been quantified. Knowledge of the structural consequences of non-uniform bone loss would be extremely useful for assessing an individual's change in hip fracture risk over time in the clinical setting.

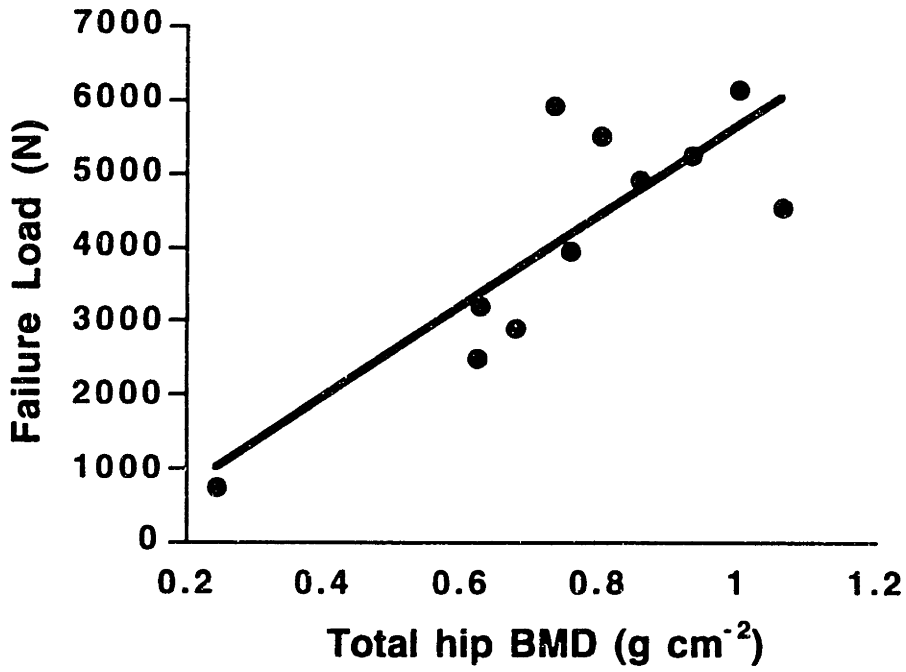

Figure 1: Relationship between total hip BMD and *ex vivo* failure load reported by Pinilla *et al.* (1996). Although the correlation is strong ($r^2 = 0.68$), femurs with similar total BMD can have dramatically different failure loads. Conversely, femurs with similar failure loads have markedly different total BMD values.

In the previous chapter, Quantitative Computed Tomography (QCT) data were used to determine the three-dimensional patterns of bone loss in the proximal femur, and the relationship between these patterns of bone loss and changes in clinical measures of BMD. In this chapter, a finite element model of the proximal femur is used to determine the structural consequences of these patterns of bone loss, independent of the confounding effects of changes in geometry. The specific objectives of this chapter are to: (1) examine the changes in femoral structural capacity and fracture pattern associated with clinically "uniform" bone loss, by determining the structural capacity of the femur (subject to loads simulating a fall on the hip) with BMD levels defined as normal, osteopenic, and

osteoporotic by an expert panel of the World Health Organization (WHO, Kanis *et al.*, 1994), (2) examine the effects of clinically "non-uniform" bone loss, by applying density reductions to the femoral neck, trochanteric and intertrochanteric regions independently and determining the changes in structural capacity and fracture pattern induced by these density reductions, and (3) determine if the changes in structural capacity and fracture pattern determined in (1) and (2) depend on the direction of impact during a fall.

7.2 Materials and Methods

7.2.1 Finite Element Model

The methods used to construct a finite element model of the proximal femur are described in detail in Chapter 5, and therefore only a brief summary is presented here. Geometric and densitometric data from QCT scans of a right proximal femur (donor age 49, male) were used to generate a finite element model of the femur using the IBID Software Suite (Hospital for Special Surgery, New York). Bone heterogeneity was modeled by assigning a unique, isotropic elastic modulus to each element, assuming a general linear relationship between QCT and apparent density, and the following equations between apparent density (ρ, g cm^{-3}) and modulus (E, MPa; Rice *et al.*, 1988; Snyder and Schneider, 1991):

$$E = 820\rho^2 + 70 \qquad \text{(trabecular bone, } \rho < 1.12 \text{ g cm}^{-3}\text{)}$$

$$E = 21910\rho - 23500 \qquad \text{(cortical bone, } \rho > 1.12 \text{ g cm}^{-3}\text{)}$$

resulting in a set of elastic moduli appropriate for quasi-static loading. During a fall, loads are applied to the femur at a rate that is approximately 50 times faster than typical quasi-static loading rates (Robinovitch *et al.*, 1991; Courtney *et al.*, 1994). Given that modulus is

proportional to strain rate to the power 0.06 (Carter and Hayes, 1976), each modulus in the model was multiplied by 50 (the ratio of loading rates for fast and quasi-static loading used *ex vivo* [Courtney *et al.*, 1994]) to the power 0.06, or 1.26. Each element was also assigned a unique strength, calculated by multiplying its modulus by a constant yield strain of either 0.8% (if the largest principal stress in the element was tensile, determined by preliminary linear analysis) or 1.0% (if the largest principal stress was compressive). Post-yield behavior was modeled using an elastic-perfectly plastic material model, based on the von Mises yield condition. The structural capacity of the femur was defined as the force required to cause the peak strain (elastic plus equivalent plastic) in cortical bone loaded in tension to reach an ultimate value of 3% (Reilly and Burstein, 1975), corresponding to the onset of structural collapse. Insight into fracture pattern was gained by examining the distribution of equivalent plastic strains in the model, which give an indication of the unrecoverable deformations present at the point of failure. Large displacement theory was used in all analyses. All pre- and post-processing of the finite element model was performed using PATRAN (Version 2.5, PDA Engineering, Costa Mesa, CA), and stresses were computed using ABAQUS (Version 5.3, Hibbitt, Karlsson & Sorensen, Pawtucket, Rhode Island).

7.2.2 Application of Age-Related Density Changes to Finite Element Model

Chapter 6 described the development of a technique for predicting a femur's three-dimensional QCT density distribution from its regional BMD values. For each of the regional BMD combinations used in this parametric study (described below), this technique was used to predict the three-dimensional density distribution. Since the geometric scaling algorithm used in this technique tends to filter out components of the density distribution with very high spatial frequencies (in particular the structurally important cortical shell), the predicted 3D density distributions were not used directly to assign material properties to the

finite element model. Instead, material properties associated with the desired BMD levels were assigned to the finite element model as follows. First, the predicted (geometry-independent) density distribution for the desired BMD levels was subtracted from the density distribution predicted from the BMD levels of the femur used in the original construction of the finite element model (Fig. 2a). The result of this subtraction was a prediction of the (geometry-independent) *difference* in three dimensional density distribution between the femur used to build the model and a femur with the desired density distribution. This predicted difference was then mapped to the geometry of the finite element model, and resliced using publicly available software (NIH Image, version 1.58) at the exact locations of the original transverse scans used to create the finite element model (Fig. 2b). This new set of transverse slices was then subtracted from the original transverse scans (Fig. 2c), resulting in a set of slices with geometry identical to the modeled femur, but with the desired density distribution. This new set of slices was then used to assign material properties to the model using the standard techniques summarized above and described in more detail in Chapter 6.

7.2.3 Parametric Studies of Age-Related Density Changes

7.2.3.1 Clinically Uniform Bone Loss

The technique described above was used to assign model material properties representative of BMD levels defined as normal, osteopenic, and osteoporotic by the WHO (Kanis *et al.*, 1994). As in Chapter 6, the specific regional BMD values used to define these diagnostic levels were derived from Looker *et al.* (1995, Table 1). Given that elderly women lose approximately 1% of their BMD each year (Greenspan *et al.*, 1994a), the reduction in BMD between the osteopenic and osteoporotic levels represents about two decades of age-related bone loss. Each of the three models was subjected to loads

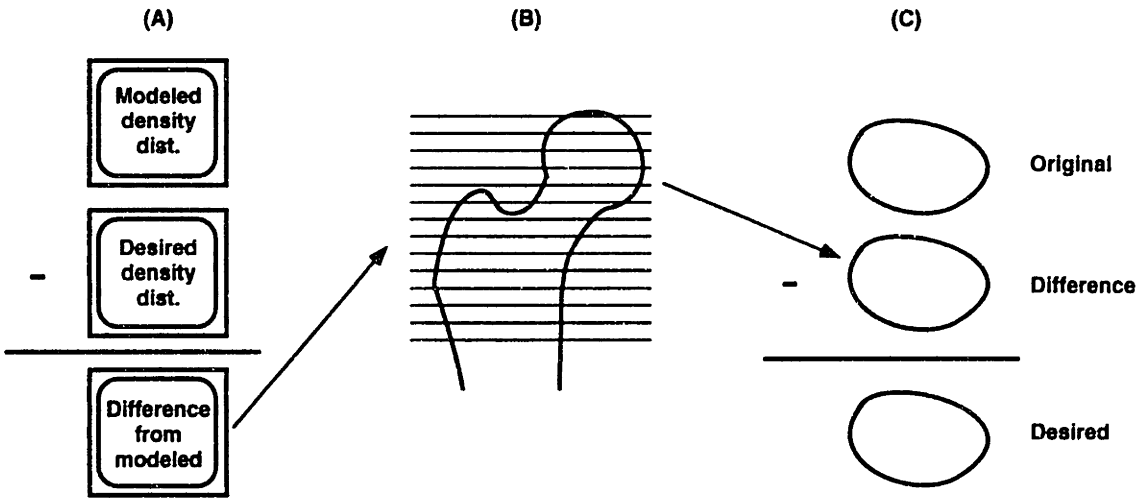

Figure 2: Flowchart describing the creation of a set of CT slices with density distribution representative of a desired BMD level. (A) The geometry-independent density distribution for the desired BMD level was predicted and subtracted from the distribution predicted from the BMD levels of the original femur used to create the finite element model. (B) This difference between the desired and modeled density distributions was then mapped to the geometry of the finite element model, and resliced at the exact locations of the original transverse CT scans used to build the model. (C) The transverse slices were then subtracted from the original CT scans, resulting in a set of transverse slices with density distribution representative of the desired BMD levels. These slices were then used to assign material properties to the finite element model.

simulating a fall with lateral impact on the greater trochanter, by placing the diaphysis at a 10° angle relative to the horizontal, and constraining it distally against internal and external rotation (simulating the resistance to rotation provided by the knee joint and the inertia of the lower leg during a fall *in vivo*, Fig. 3). A distributed load was applied to the inferior surface of the femoral head, with the resultant force acting through the center of the femoral head. The femoral head was constrained such that it could rotate about its center (simulating sliding of the femoral head within the acetabulum), but the center could translate only in the direction of the applied load (simulating the resistance to femoral head translation provided

by the acetabulum). The greater trochanter was constrained vertically (simulating the constraint provided by the impact surface during a fall), but free to slide in the horizontal plane.

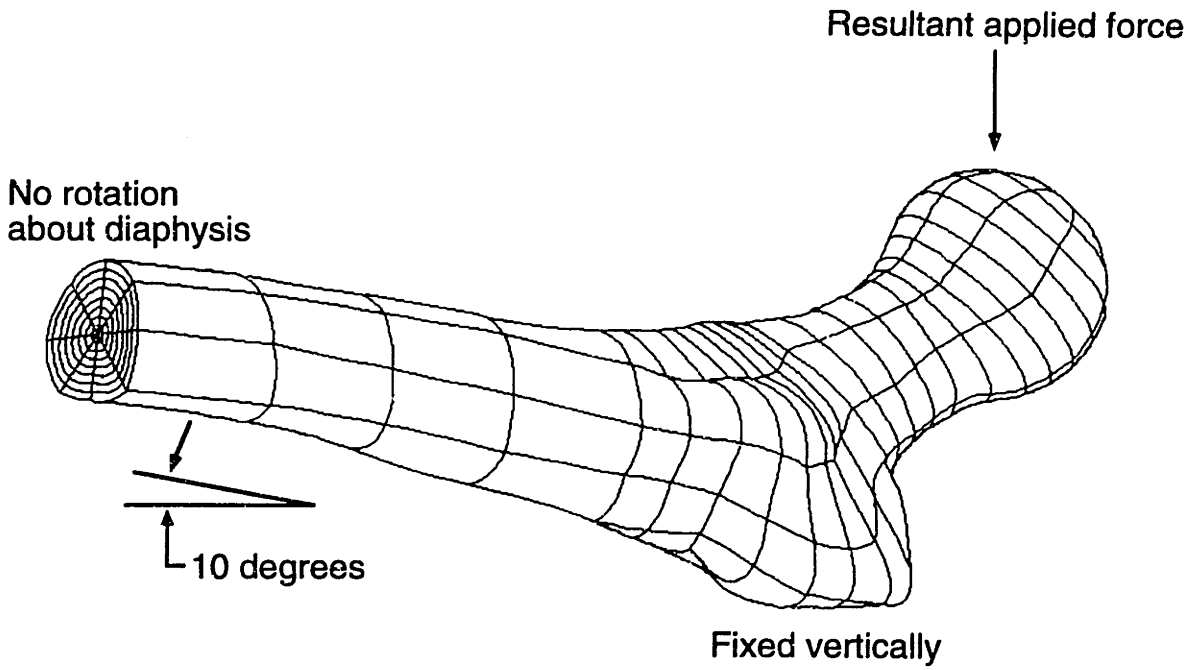

Figure 3: Posterior view of finite element model, showing loads and boundary conditions used to simulate falls with impact on the greater trochanter. The diaphysis was at a 10° angle relative to the horizontal, and fixed distally against internal and external rotation. The greater trochanter was fixed vertically but free to slide in the horizontal plane. The center of the femoral head was constrained to move only vertically. Loading was applied to the inferior surface of the femoral head, with resultant acting through the center of the femoral head.

To determine if age-related changes in structural capacity were sensitive the direction of impact during a fall, each of the models (normal, osteopenic, and osteoporotic) was subjected to two variations of the fall loading condition described above. Both variations simulated falls with impact on the greater trochanter, but with variation in the angle between the load vector and the femoral neck axis (as viewed from the superior

aspect of the femoral head). An angle of 15° (Fig. 4a) represented a typical body position at impact during experimental sideways falls (van den Kroonenberg *et al.*, 1996). An angle of 45° (Fig. 4b) simulated a fall with impact in a more posterolateral direction.

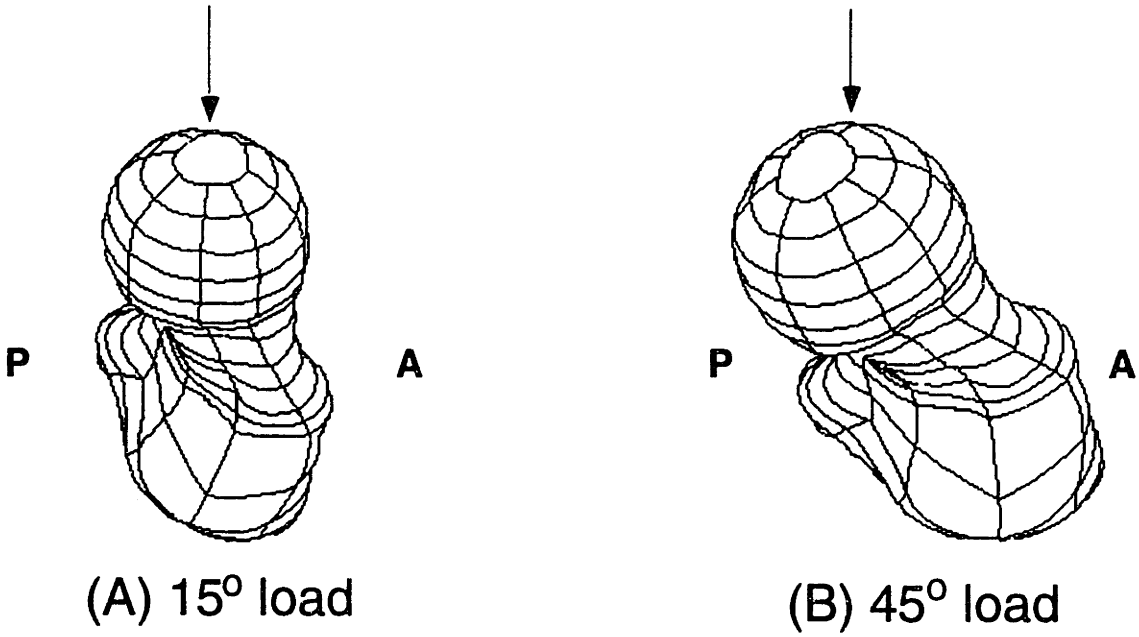

Figure 4: Superior views of finite element model, showing two impact directions examined. (A) An angle of 15° between the load vector and femoral neck axis simulated a fall with lateral impact on the greater trochanter. (B) An angle of 45° simulated a fall with posterolateral impact on the greater trochanter. A, anterior; P, posterior.

7.2.3.2 Clinically Non-Uniform Bone Loss

Although bone loss that occurs longitudinally in the trochanteric region of elderly women is correlated with bone loss in the intertrochanteric region (r = 0.63, [Greenspan *et al.*, 1994a]), neither of these regions experiences bone loss that is well correlated with BMD reductions at the femoral neck (trochanter, r = 0.0; intertrochanter, r = 0.05).

Therefore, clinically "non-uniform" bone loss was simulated by altering the BMD of the femoral neck independently from the trochanteric and intertrochanteric regions. Using the osteopenic model as a baseline representing an elderly individual (whose longitudinal changes in fracture risk would be of clinical interest), two types of non-uniform bone loss were examined (Table 2). First, loss of bone in the femoral neck was examined by applying femoral neck BMD reductions of 11% and 22% to the model, while keeping the trochanteric and intertrochanteric BMD values constant. The reduction of 22% in the femoral neck was the same as that used to model the reduction from osteopenic to osteoporotic in the study of clinically uniform bone loss, and therefore represents about two decades of femoral neck bone loss. Then, loss of bone in the trochanteric and intertrochanteric regions was examined by applying BMD reductions in these regions of 11% and 22%, keeping femoral neck BMD constant. As in the femoral neck, the reduction of 22% in the trochanteric and intertrochanteric regions represented about two decades of bone loss. The models representing each of these regional BMD combinations was subjected to the fall loading conditions described previously, with both lateral and posterolateral impact directions. Structural capacity of the femur and fracture pattern were predicted for each case.

Model	Femoral neck BMD ($g\ cm^{-2}$)	Trochanteric BMD ($g\ cm^{-2}$)	Intertrochanteric BMD ($g\ cm^{-2}$)
Osteopenic	0.659	0.546	0.864
Femoral neck bone loss, ~1 decade	0.585	0.546	0.864
Femoral neck bone loss, ~2 decades	0.511	0.546	0.864
Troch & intertroch bone loss, ~1 decade	0.659	0.485	0.776
Troch & intertroch bone loss, ~2 decades	0.659	0.424	0.688

Table 2: BMD values used to examine the effects of clinically non-uniform bone loss. The osteopenic model was used as a baseline.

7.3 Results

The uniform BMD reduction of 22% between the normal and osteopenic levels caused a reduction in structural capacity of 20.6%, from 2770N to 2200N, when the femur was subject to loads simulating lateral impact on the greater trochanter. The uniform BMD reduction of 22% between the osteopenic and osteoporotic levels caused a larger structural capacity reduction of 25.9%, from 2200N to 1630N (Fig. 5). Although uniform BMD reductions had a substantial effect on structural capacity, they did not cause the distribution of plastic strains in the femur to change significantly (Fig. 6). When loads simulating

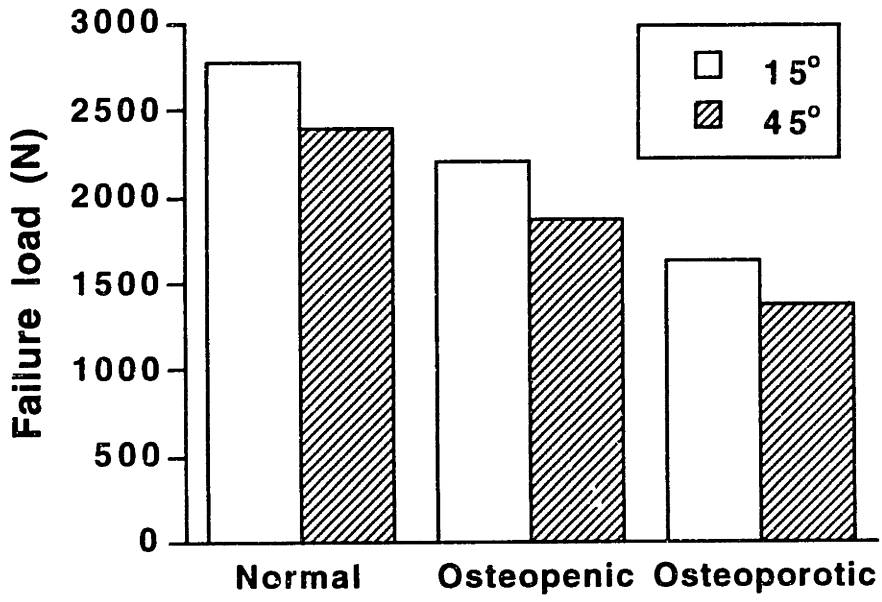

Figure 5: Predicted failure loads for the normal, osteopenic, and osteoporotic BMD levels, for both lateral impact (15°) and posterolateral impact (45°). For the case of lateral impact, failure load decreased by 20.6% between the normal and osteopenic levels, and decreased by 25.9% between the osteopenic and osteoporotic levels. For the case of posterolateral impact, failure load decreased by similar amounts, which were 21.8% between the normal and osteopenic levels and 26.7% between the osteopenic and osteoporotic levels.

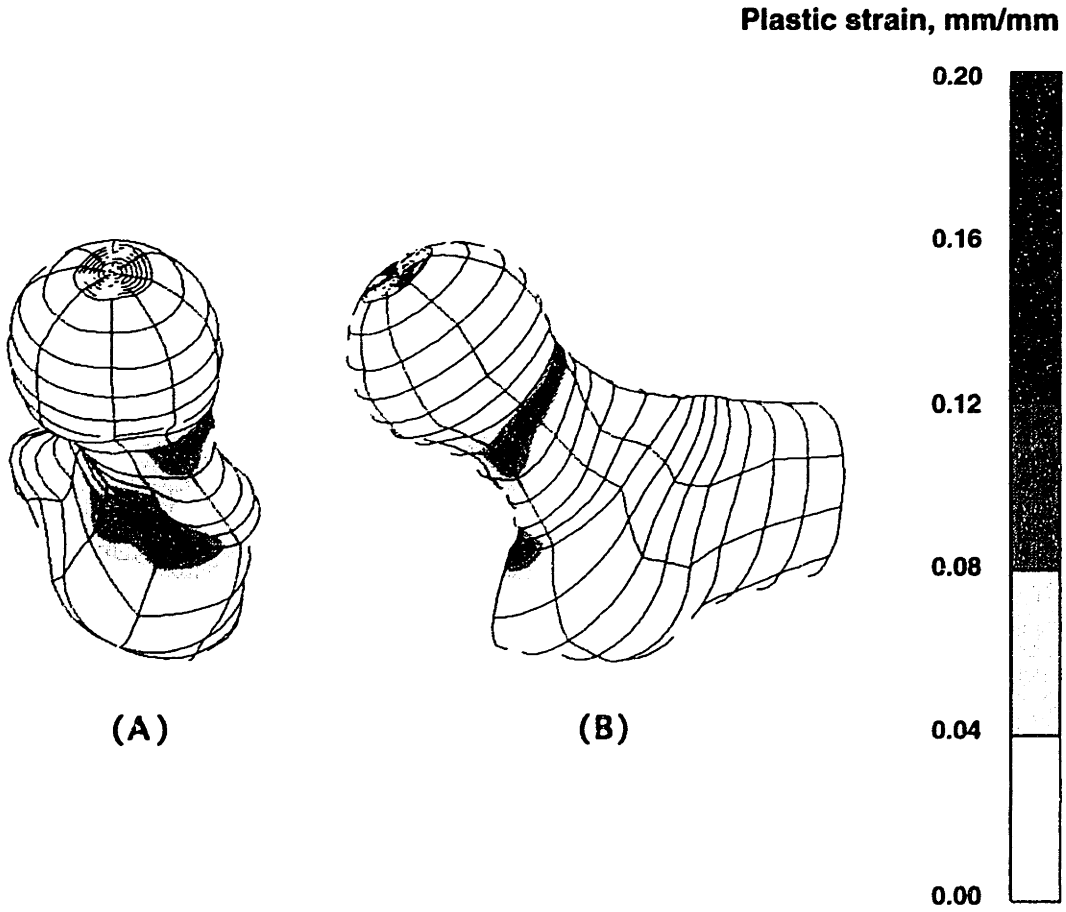

Figure 6: Equivalent plastic strain distribution at failure for the osteopenic model. High strains occurred anteriorly in the subcapital region, and superiorly at the border of the femoral neck and trochanteric regions. This distribution of plastic strains was similar to the distributions for the normal and osteoporotic models.

posterolateral impact were applied to the femur, structural capacity dropped by 21.8% between the normal and osteopenic BMD levels (from 2390N to 1870N), and dropped by 26.7% between the osteopenic and the osteoporotic BMD levels (from 1870N to 1370N, Fig. 5). Therefore, although the predicted failure loads for lateral impact were about 15% higher than for posterolateral impact (as expected given the results of Chapter 5), the direction of impact did not have a significant effect on the percent reductions in structural capacity associated with clinically uniform bone loss. As in the case of lateral impact, the distribution of plastic strains did not change appreciably as a function of BMD when loads simulating posterolateral impact were applied to the femur.

When subjected to loads simulating lateral impact, one decade of femoral neck bone loss applied to the osteopenic femur resulted in a structural capacity reduction of 7.3%, from 2200N to 2040N; two decades of femoral neck bone loss reduced structural capacity by 12.7%, to 1920N (Fig. 7a). Combined trochanteric and intertrochanteric bone loss caused a reduction in failure load of 12.7% (from 2200N to 1920N) over 1 decade, and caused a reduction of 16.8% (to 1830N) over two decades. Therefore, for the lateral impact direction, loss of bone in the trochanteric and intertrochanteric regions was associated with greater reductions in structural capacity than bone loss in the femoral neck. Failure load reductions were similar when loads simulating posterolateral impact were applied to the femur (Fig. 7b). In this case, one decade of femoral neck bone loss resulted in a drop in structural capacity of 8.6% (from 1870N to 1710N); two decades caused a drop of 14.4% (to 1600N). Combined trochanteric and intertrochanteric bone loss caused a reduction in failure load of 11.8% (from 1870N to 1650N) over one decade, and a reduction of 14.4% (to 1600N) over two decades.

The distribution of plastic strains in the femur at failure depended on the relative values of femoral neck and trochanteric BMD. For the baseline case (osteopenic), high plastic strains were located subcapitally on the anterior surface of the femur, and also near the border of the femoral neck and trochanteric regions, on the superior aspect of the femur

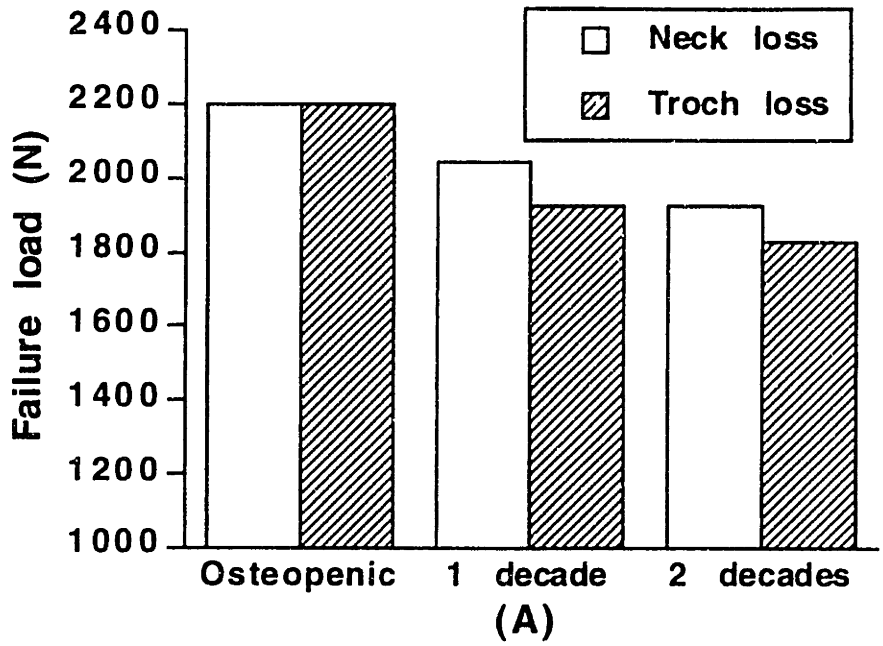

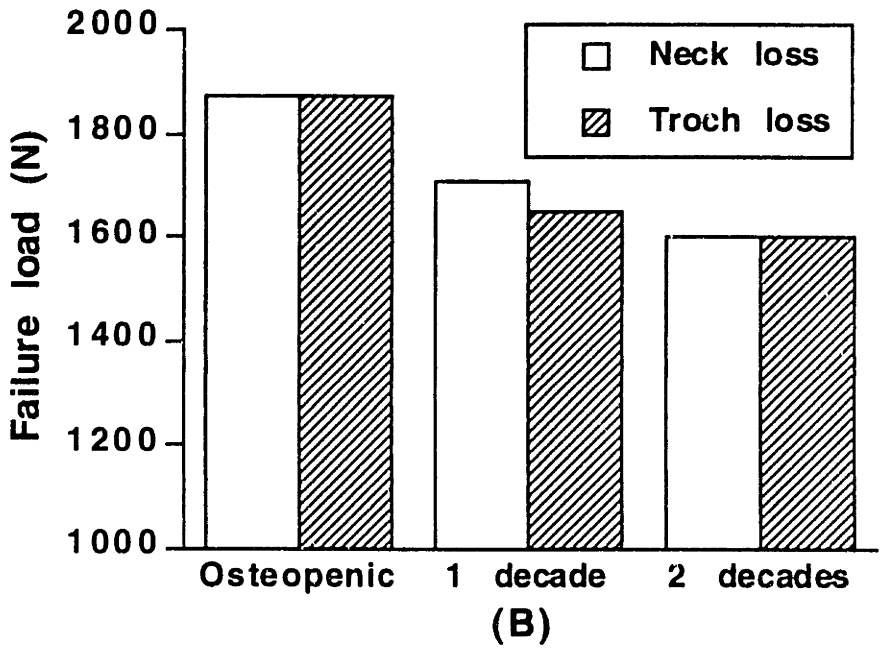

Figure 7: Failure loads for BMD levels representing non-uniform bone loss, for lateral (A) and posterolateral (B) impact directions. Loss of BMD in the trochanteric and intertrochanteric regions (filled bars) was associated with larger reductions in failure load than loss of BMD in the femoral neck (unfilled bars).

(Fig. 8a, b). When the femoral neck BMD was reduced and the trochanteric and intertrochanteric BMD values held constant, the plastic strains increased in the subcapital region and decreased near the trochanteric region relative to the baseline case (Fig. 8c, d). By contrast, when the trochanteric and intertrochanteric BMD values were decreased and the femoral neck BMD held constant, the plastic strains decreased at the subcapital site and increased near the trochanteric region relative to the baseline case (Fig. 8e, f). This shift in the distribution of plastic strains occurred for both the lateral (Fig. 8) and posterolateral (Fig. 9) loading directions, suggesting that fracture pattern may be sensitive to the relative values of femoral neck, trochanteric, and intertrochanteric BMD.

7.4 Discussion

The goal of this study was to determine the structural consequences of uniform and non-uniform BMD reductions in the proximal femur, independent of the confounding effects of inter-bone differences in geometry. By applying the three-dimensional patterns of bone loss determined in Chapter 6 to a finite element model of the femur, it was demonstrated that a reduction in BMD from a level defined as normal to a level defined as osteopenic (a uniform reduction in the femoral neck, trochanter, and intertrochanter of about 22%) reduced the structural capacity of the femur by 21%. A further reduction in BMD from the osteopenic level to a level defined as osteoporotic (also a uniform reduction of 22% in the three regions of interest) reduced structural capacity by 26%. In addition, loss of BMD in the trochanteric and intertrochanteric regions (with femoral neck BMD held constant) was associated with greater reductions in structural capacity than loss of BMD in the femoral neck (with trochanteric and intertrochanteric BMD held constant). Although the distribution of plastic strains at failure did not change with uniform BMD reductions, there were shifts in the strain distribution when non-uniform BMD reductions were applied to the

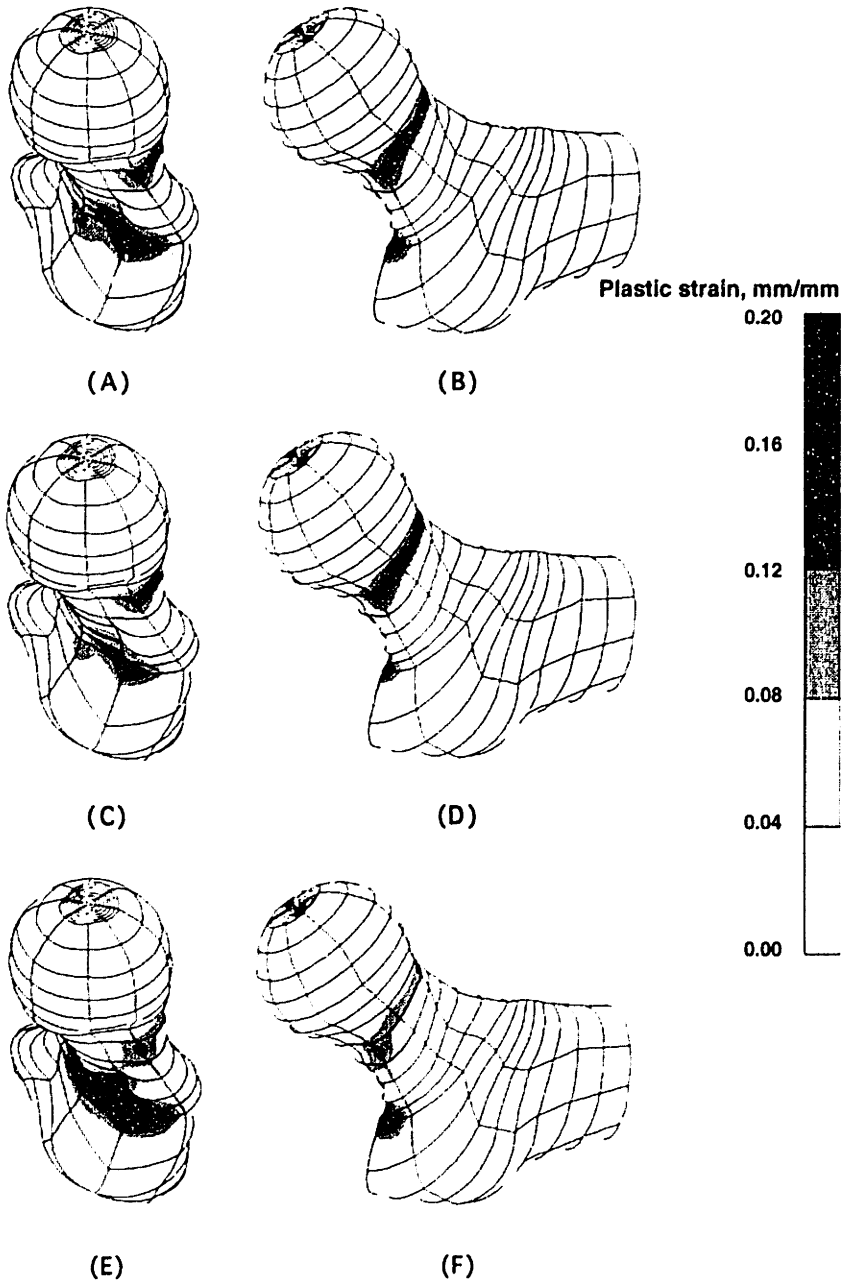

Figure 8: Plastic strain distributions at failure associated with non-uniform BMD reductions, for the case of lateral impact. (A, B) Strain distribution for osteopenic model. Strains are high anteriorly at the subcapital site and superiorly at the border of the neck and trochanteric regions. (C, D) Strain distribution for two decades of BMD loss in the femoral neck, with trochanteric and intertrochanteric BMD held constant. Strains in the femoral neck are higher than the baseline case (osteopenic), and are lower near the trochanteric region. (E, F). Strain distribution for two decades of BMD loss in the trochanteric and intertrochanteric regions, with femoral neck BMD held constant. Strains in the femoral neck are lower than in the baseline case, and are higher near the trochanteric region.

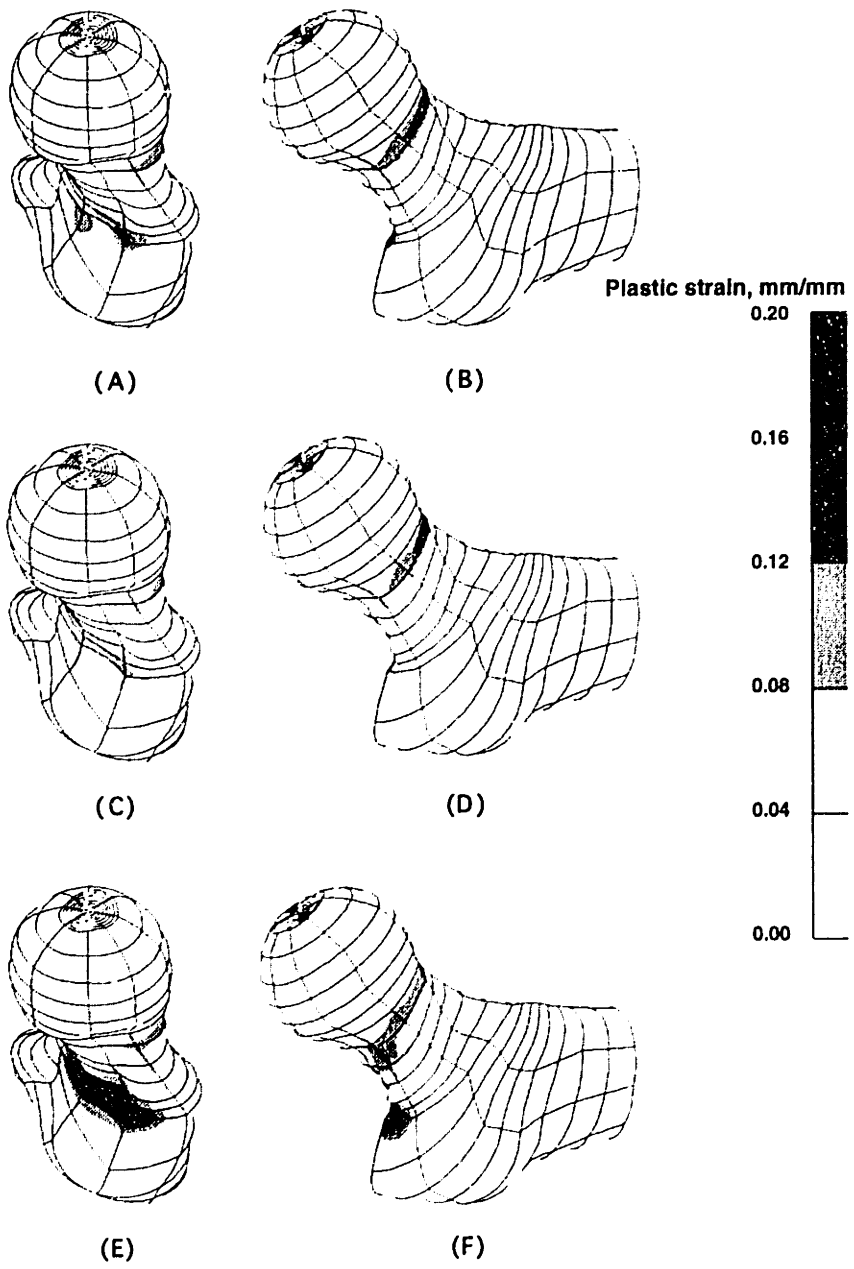

Figure 9: Plastic strain distributions at failure associated with non-uniform BMD reductions, for the case of posterolateral impact. (A, B) Osteopenic model. (C, D) Two decades of femoral neck BMD loss, with trochanteric and intertrochanteric BMD held constant. Strains are lower near the trochanteric region compared to the osteopenic case.(E, F) Two decades of trochanteric and intertrochanteric BMD loss, with femoral neck BMD held constant. Strains are lower in the femoral neck and higher near the trochanteric region relative to the osteopenic case.

model, indicating that fracture pattern may be sensitive to the relative BMD levels in the femoral neck, trochanteric, and intertrochanteric regions.

The results of this study provide the first data regarding the geometry-independent relationship between age-related bone loss and changes in the structural capacity of the femur. Prior to this study, knowledge of the relationship between BMD and femoral strength was limited to experimentally-determined correlations from populations with a broad range of femur geometries. Since geometric parameters (such as femoral neck cross-sectional area) can explain up to about 75% of the variance in femoral failure load present within a population (Courtney *et al.*, 1994; Pinilla *et al.*, 1996), these *ex vivo* data do not necessarily reflect the relationship between BMD and failure load for an individual, whose density changes occur independent or nearly independent of geometric changes. The results of this study are also unique in that they arise from models that incorporated the fully three-dimensional patterns of bone loss that are associated with reductions in BMD. In addition to considering the complexity of patterns of age-related bone loss, another strength of this study is that it incorporated a range of loading conditions appropriate for simulating falls with impact on the hip, including loads lying outside the frontal plane under which the femur is particularly weak.

Although the results of this study provide valuable theoretical information that would be nearly impossible to obtain experimentally, there are limitations of the investigation that deserve attention. Important among these limitations are those associated with the finite element model used. The magnitudes of the predicted failure loads may be sensitive to both the use of isotropic material properties for bone, and to the use of the von Mises yield condition to model bone material failure. Since apparent density explains approximately 80% of the variance in trabecular bone modulus (Rice *et al.*, 1988), and the addition of architectural parameters results in only slight improvements in predictive accuracy (Snyder and Hayes, 1990), the incorporation of material anisotropy would probably not alter the trends in femoral strength predicted as a function of age-related bone

loss. This is particularly true since the model did incorporate the full heterogeneity in density found within the femur, and also incorporated fully three-dimensional patterns of density loss. With regard to the choice of failure criterion, the model reported here using the von Mises yield condition has been used successfully to predict changes in structural capacity associated with differences in the direction of impact during a fall (see Chapter 5). This evidence, combined with the finite element results of previous investigators (Lotz *et al.*, 1991a; Lotz *et al.*, 1991b; Keyak *et al.*, 1996), lends support to the use of the von Mises yield condition for predicting relative strength values. However, further research into the multiaxial failure behavior of trabecular bone is needed before finite element models of the femur can be used to predict failure load magnitudes with great accuracy.

In addition to the limitations associated with the finite element model itself, our examination of the structural consequences of bone loss using only a single femoral geometry may limit the applicability of our results to femurs with different geometries. It is possible that femurs with different geometrical features (e.g. femoral neck length, width, angle, and cross-sectional area) have different structural responses to age-related density reductions. The techniques developed here for converting age-related density changes to changes in finite element model material properties could be adapted to any QCT-generated finite element model. An area for future research, then, is to examine the structural consequences of age-related bone loss in femurs with a wide range of geometries. Another potential limitation relates to the patterns of BMD loss examined in the parametric study of non-uniform bone loss. It is unlikely that many individuals experience bone loss in one region of the femur (for example, the femoral neck) completely independently from bone loss in other regions (such as the trochanteric region). However, investigators have demonstrated, using longitudinal data, that bone loss in the femoral neck is not correlated with bone loss in either the trochanteric or intertrochanteric regions (Greenspan *et al.*, 1994a). Therefore, the patterns of BMD reduction used in this study, although extreme, represent reasonable bounds on the types of bone loss that may occur in individuals.

The geometry-independent reductions in structural capacity predicted here are somewhat different from the reductions predicted by experimentally-determined relationships between BMD and femoral failure load. The predicted reduction in structural capacity of 21% (average of the results from the lateral and posterolateral impact directions of 20.6% and 21.8%, respectively) between the normal and osteopenic BMD levels agrees well with the reduction of 22% calculated from the relationship between total BMD and failure load reported by Pinilla *et al.* (1996), however it is somewhat lower than the reduction of 28% calculated from the relationship reported by Courtney *et al.* (1994) between femoral neck BMD and failure load. By contrast, between the osteopenic and osteoporotic BMD levels, the finite element model predicted a failure load reduction of 26%; the data of Pinilla *et al.* suggest a larger reduction of 34%, while the data of Courtney *et al.* suggest a reduction of 30%, somewhat closer to that predicted by the finite element model. The apparent inconsistencies in strength reduction calculated from the data of these *ex vivo* studies are probably caused at least in part by inter-study differences in geometric variables, resulting in somewhat different relationships between BMD and femoral strength. These inconsistencies between *ex vivo* studies, coupled with the differences between the results of the *ex vivo* studies and the geometry-independent results from the finite element model, underscore the idea that cross-sectional BMD-failure load relationships are confounded by geometry, and therefore do not necessarily reflect the (geometry-independent) BMD-failure load relationship for a given individual.

The results of this study indicate that a reduction in BMD later in life (i.e., between normal and osteopenic BMD levels) may cause a greater percent reduction in structural capacity than the same percentage BMD reduction earlier in life (i.e., between normal and osteopenic BMD levels). This dependence of failure load reduction on baseline BMD level was predicted despite the fact that true density differences were *less* between the osteopenic and osteoporotic levels than they were between the normal and osteopenic levels (based on the cross-sectional analysis of Chapter 6). When assessed longitudinally, the rate of

femoral bone loss in elderly women actually *increases* with age (Greenspan *et al.*, 1994a). Assuming that BMD losses in these women occur in the absence of large geometric changes, the relationship between bone loss and structural capacity for elderly women may be even *more* non-linear than the results of this study indicate.

In the parametric study of non-uniform BMD reductions, loss of bone in the trochanteric and intertrochanteric regions (with femoral neck BMD held constant) caused larger reductions in structural capacity than loss of bone in the femoral neck (with trochanteric and intertrochanteric BMD held constant). This result may help to explain some of the scatter present in experimentally-determined relationships between BMD and failure load. Pinilla *et al.* (1996) tested a group of cadaveric femurs to failure under fall loading conditions identical to the lateral impact direction used in this study, and reported a relationship between total BMD and failure load (Fig. 1). Analysis of these data revealed that all of the data points lying above the regression line (n = 4) had a ratio of femoral neck to trochanteric BMD *less* than one, while all points below the regression line (n = 6) had a ratio of femoral neck to trochanteric BMD *greater* than one. This is consistent with the results from the finite element model presented here, which predicted lower structural capacities when the trochanteric BMD was reduced relative to the femoral neck BMD. Therefore, the relative magnitudes of an individual's femoral neck and trochanteric BMD may aid in predicting whether his or her femoral strength is greater or less than that predicted from total BMD alone.

The dependence of plastic strain distribution (and therefore possibly fracture pattern) on the relative magnitudes of BMD in the femoral neck and trochanteric regions is consistent with previous clinical findings. In a population of elderly hip fracture patients, Greenspan *et al.* (1994b) found that both a high femoral neck BMD and a low trochanteric BMD were associated with the occurrence of trochanteric fractures. The finding of this study that reduction of trochanteric BMD relative to femoral neck BMD caused plastic strains to decrease in the femoral neck and increase near the trochanteric region is consistent

with this clinical finding. In addition to the difference in fracture pattern associated with relative regional BMD values, the results of this study indicate that a low trochanteric relative to femoral neck BMD may also be associated with a lower structural capacity of the femur. The combination of clinical and theoretical results indicates, then, that osteopenic individuals with low trochanteric relative to femoral neck BMD have two strikes against them: a greater risk of fracture due to lower structural capacity and, if they do fracture, a greater risk of sustaining trochanteric fractures (which have been associated with higher mortality [Crane and Kernek, 1983; Lawton *et al.*, 1983] than femoral neck fractures). Therefore, the *ratio* of trochanteric to femoral neck BMD, as well as total BMD, should be considered in the evaluation of hip fracture risk.

7.5 References

Bouxsein M., Courtney A., and Hayes W. (1995) Ultrasound and densitometry of the calcaneus correlate with the failure loads of cadaveric femurs. *Calcif Tissue Int* **56**, 99-103.

Carter D. R. and Hayes W. C. (1976) Bone compressive strength: the influence of density and strain rate. *Science* **194**, 1174-1176.

Courtney A. C., Wachtel E. F., Myers E. R., and Hayes W. C. (1994) Effects of loading rate on strength of the proximal femur. *Calcif Tissue Int* **55**, 53-58.

Courtney A. C., Wachtel E. F., Myers E. R., and Hayes W. C. (1995) Age-related reductions in the strength of the femur tested in a fall loading configuration. *J Bone Joint Surg [Am]* **77**, 387-395.

Crane J. and Kernek C. (1983) Mortality associated with hip fractures in a single geriatric hospital and residential health facility: a ten-year review. *J Am Geriatr Soc* **31**, 472-475.

Cummings S., Nevitt M., Browner W., Stone K., Fox K., Ensrud K., Cauley J., Black D., and Vogt T. (1995) Risk factors for hip fracture in white women. *N Engl J Med* **332**, 767-773.

Cummings S. R., Black D. M., and Nevitt M. C. (1990) Appendicular bone density and age predict hip fracture in women. *JAMA* **263**, 665-668.

Cummings S. R., Black D. M., Nevitt M. C., Browner W., Cauley J., Ensrud K., Genant H. K., Palermo L., Scott J., and Vogt T. M. (1993) Bone density at various sites for prediction of hip fractures. *Lancet* **341**, 72-75.

Greenspan S., Maitland L., Myers E., Krasnow M., and Kido T. (1994a) Femoral bone loss progresses with age: A longitudinal study in women over age 65. *J Bone Min Res* **9**, 1959-1965.

Greenspan S., Myers E., Maitland L., Kido T., Krasnow M., and Hayes W. (1994b) Trochanteric bone mineral density is associated with type of hip fracture in the elderly. *J Bone Min Res* **9**, 1889-1894.

Kanis J. A., Melton L. J., Christiansen C., Johnston C. C., and Khaltaev N. (1994) The diagnosis of osteoporosis. *J Bone Min Res* **9**, 1137-1141.

Keyak J., Jones K., Rossi S., and Skinner H. (1996) Prediction of femoral strength in two load configurations using CT scan-derived finite element models. *Trans 42nd ORS* **21**, 249.

Lawton J., Baker M., and Dickson R. (1983) Femoral neck fractures - two populations. *Lancet* **2**, 70-72.

Looker A., Johnston C., Wahner H., Dunn W., Calvo M., Harris T., Heyse S., and Lindsay R. (1995) Prevalence of low femoral bone density in older U.S. women from NHANES III. *J Bone Min Res* **10**, 796-802.

Lotz J. C., Cheal E. J., and Hayes W. C. (1991a) Fracture prediction for the proximal femur using finite element models: Part 1-Linear analysis. *J Biomech Eng* **113**, 353-360.

Lotz J. C., Cheal E. J., and Hayes W. C. (1991b) Fracture prediction for the proximal femur using finite element models: Part 2-Nonlinear analysis. *J Biomech Eng* **113**, 361-365.

Melton L., Atkinson E., O'Fallon W., Wahner H., and Riggs B. (1993) Long-term fracture prediction by bone mineral assessed at different skeletal sites. *J Bone Min Res* **8**, 1227-1233.

Nevitt M., Johnell O., Black D., Ensrud K., Genant H., and Cummings S. (1994) Bone mineral density predicts non-spine fractures in very elderly women. *Osteoporosis Int* **4**, 325-331.

Pinilla T., Boardman R., Bouxsein M., Myers E., and Hayes W. (1996) Impact direction from a fall influences the failure load of the femur as much as age-related bone loss. *Calcif Tissue Int* **58**, 231-235.

Reilly D. T. and Burstein A. H. (1975) The elastic and ultimate properties of compact bone tissue. *J Biomech* **8**, 393-405.

Rice J. C., Cowin S. C., and Bowman J. A. (1988) On the dependence of the elasticity and strength of cancellous bone on apparent density. *J Biomech* **21**, 155-168.

Robinovitch S. N., Hayes W. C., and McMahon T. A. (1991) Prediction of femoral impact forces in falls on the hip. *J Biomech Eng* **113**, 366-374.

Snyder B. D. and Hayes W. C. (1990) Multiaxial Structure-Property Relations in Trabecular Bone. In *Biomechanics of Diarthrodial Joints*, 31-59, Ed. Mow V. C., Ratcliffe A., and Woo S. L.-Y., Springer-Verlag, New York.

Snyder S. M. and Schneider E. (1991) Estimation of mechanical properties of cortical bone by computed tomography. *J Orthop Res* **9**, 422-431.

van den Kroonenberg A., Hayes W. C., and McMahon T. A. (1996) Hip impact velocities and body configurations for voluntary falls from standing height. *J Biomech* **29**, 807-811.

Weber T. G., Yang K. H., Woo R., and Fitzgerald R. H. (1992) Proximal femur strength: Correlation of the rate of loading and bone mineral density. *ASME Adv in Bioengineering* **22**, 111-114.